Atomic layer deposition for biosensing applications

Octavio Graniel Tamayo

To cite this version:

Octavio Graniel Tamayo. Atomic layer deposition for biosensing applications. Other. Université Montpellier, 2019. English. ⟨NNT : 2019MONTS071⟩. ⟨tel-02964682⟩

HAL Id: tel-02964682
https://theses.hal.science/tel-02964682v1
Submitted on 12 Oct 2020

THÈSE POUR OBTENIR LE GRADE DE DOCTEUR DE L'UNIVERSITÉ DE MONTPELLIER

En chimie séparative, matériaux et procédés

École doctorale Sciences Chimiques Balard (ED459)

Unité de recherche Institut Européen des Membranes (IEM-UMR 5365)

Atomic layer deposition for biosensing applications

Présentée par Octavio GRANIEL TAMAYO
Le 8 octobre 2019

Sous la direction de Philippe MIELE,
la co-direction de Sébastien BALME
et l'encadrement de Mikhael BECHELANY

Devant le jury composé de

David MUÑOZ-ROJAS, Chargé de Recherche CNRS, Université Grenoble Alpes	Rapporteur
Grégory BARBILLON, Professeur, École d'ingénieur-e-s (EPF)	Rapporteur
Frédéric FAVIER, Directeur de Recherche, Université de Montpellier	Président
Mathilde LEPOITEVIN, Maître de Conférences, École Normale Supérieure	Examinatrice
Philippe MIELE, Professeur, ENCSM et Institut Universitaire de France	Directeur de thèse
Sébastien BALME, Maître de Conférences, Université de Montpellier	Co-directeur de thèse
Mikhael BECHELANY, Chargé de Recherche CNRS, Université de Montpellier	Invité

UNIVERSITÉ
DE MONTPELLIER

Para mi Mamá Pili

Abstract

Atomic layer deposition (ALD) has emerged as an essential vapor deposition technique of thin films for countless applications. The rising demand for electronic components and nanostructured materials has established ALD as one of the key fabrication processes in the nanotechnology market.

In this work, novel nanostructured materials that can be used as transducers in biosensor devices are presented. These materials have been prepared by a combination of ALD with top-down and bottom-up techniques such as nanosphere lithography (NSL), physical vapor deposition (PVD), metal-assisted chemical etching (MACE), and electrodeposition.

As a first promising candidate, silicon nanowires (SiNWs) covered with ZnO by ALD were fabricated. These 3D structures are quite attractive for optical biosensing applications thanks to their intense photoluminescence (PL) activity at room temperature. These core/shell nanostructures were fully characterized and tested as possible sensors for the detection of hydrogen peroxide, which is a common reaction product of several oxidoreductases.

In addition, Au-covered hollow urchin-like ZnO nanostructures were prepared with controlled size by combining NSL, ALD, electrodeposition, and electron beam (E-beam) evaporation. The influence of the Au film thickness on the surface-enhanced Raman scattering (SERS) capabilities of the substrates was investigated. The optimized structures were used to detect thiophenol molecules with a limit of detection (LOD) of 10^{-8} M. Additionally, adenine can be detected with a concentration as low as 10^{-6} M. The excellent uniformity and batch-to-batch repeatability of the substrates makes them excellent candidates for reliable SERS sensing and biosensing.

Moreover, a miscellaneous group of novel materials with enticing features that can be readily applied in sensing, catalysis, and plasmonics is presented. Bimetallic Pd/Au nanoparticles supported on SiNWs with ALD and galvanic replacement were fabricated. Furthermore, hollow urchin-like ZnO structures with ZIF-8 via electrodeposition were fabricated for possible SERS applications.

Résumé

Le dépôt de couche atomique (ALD) est devenu une technique essentielle de dépôt en phase vapeur de couches minces pour de nombreuses applications. La demande croissante de composants électroniques et de matériaux nanostructurés a fait de ALD l'un des processus de fabrication clés du marché des nanotechnologies.

Dans ce travail, nous présentons de nouveaux matériaux nanostructurés pouvant être utilisés comme transducteurs dans des dispositifs à biocapteurs. Ces matériaux ont été préparés en combinant ALD avec des techniques "top-down" et "bottom-up" telles que la lithographie par nanosphère (NSL), le dépôt physique en phase vapeur (PVD), la gravure chimie assistée par des métaux (MACE) et électrodéposition.

En tant que premier candidat prometteur, des nanofils de silicium (SiNWs) recouverts de ZnO par ALD ont été fabriqués. Ces structures 3D sont très attractives pour les applications de biocapteurs optiques en raison de leur activité intense de photoluminescence (PL) à température ambiante. Dans une première approche, ces nanostructures cœur/coquille ont été entièrement caractérisées et testées en tant que capteurs possibles pour la détection du peroxyde d'hydrogène, qui est un produit de réaction courant de plusieurs oxydoréductases.

De plus, des nanostructures creuses en ZnO semblables à des oursins recouvertes de Au ont été préparées avec une taille contrôlée en combinant NSL, ALD, électrodéposition et évaporation par faisceau d'électrons (E-beam). L'influence de l'épaisseur du film Au sur les capacités de diffusion Raman (SERS) améliorées en surface des substrats a été étudiée. Les structures optimisées ont été utilisées pour détecter des molécules de thiophénol avec une limite de détection (LOD) de 10^{-8} M. De plus, l'adénine peut être détectée avec une concentration aussi basse que 10^{-6} M. L'excellente uniformité et la répétabilité lot par lot des substrats en font d'excellents candidats pour une détection et une biocapture SERS fiables.

En outre, un groupe diversifié de nouveaux matériaux présentant des caractéristiques attrayantes qui peuvent être facilement appliqués à la détection, à la catalyse et à la plasmonique est présenté. Des nanoparticules bimétalliques de Pd/Au supportées sur SiNWs avec ALD et un remplacement galvanique ont été fabriquées. De plus, des structures ZnO creuses de type urchin avec ZIF-8 par électrodéposition ont été fabriquées pour de possibles applications SERS.

Acknowledgements

First of all, I want to thank **Mikhael Bechelany** for answering that very first e-mail that put me on the road to pursuing a PhD. His mentoring and expertise in materials science, the countless constructive discussions, and the reassuring support throughout these last three years are some of the reasons why I can present this PhD work today. Thank you for giving me the chance to travel around Europe (and one country in Asia) to present our work and build a strong network of researchers with many different backgrounds.

I want to thank as well **Philippe Miele** and **Sébastien Balme** for giving me the chance of working at the Institut Européen des Membranes (IEM), the continuous guidance, and their sincere suggestions to carry out my experiments. I want to acknowledge the immense help of **Jean Marc Janot** with photoluminescence and the long discussions about stepping motors, lasers, computer programming, and optics. I want to thank **Sophie Tingry** and **Yaovi Holade** for answering all of the questions I had about electrochemistry and for letting me use their lab freely. I want to give a special mention to **Martin Dobrek** for his support on the annealing of most of my samples and for making sure that I followed the safety rules when handling dangerous materials (e.g., HF). I want to thank also **Vincent Rouessac** for sharing his vast knowledge on ellipsometry and for kindly showing me how to perform reactive ion etching. Regarding ALD, I want to mention the great help of **Bruno Navarra** when it came to fixing the ALD system.

The CanBioSe MSCA RISE Horizon 2020 project allowed me to meet some extraordinary people that contributed enormously to this work. I want to thank **Igor Iatsunskyi** and **Emerson Coy** for the TEM images and Raman measurements, **Roman Viter** for some photoluminescence studies, **Martin Järvekülg**, **Jaan Aarik**, and **Aarne Kasikov** for their help with Au sputtering.

For this dissertation, I want to thank my reading committee members **David Muñoz-Rojas** and **Grégory Barbillon** for their time, valuable comments, and interest to read this thesis. I want to thank as well my oral defense committee members **Frédéric Favier** and **Mathilde Lepoitevin** for their time and insightful remarks.

During these three years at the IEM, I had the honor of meeting some of the most incredible and kindest people. I want to give a special mention to all of the students that I met in the lab of Mika who helped me in some way or another: **Viktoriia Fedorenko** for the guiding with metal-assisted chemical etching (MACE), **Sakthivel Nagarajan** and **Socrates Radhakrishnan** for keeping me company late at night just before the lab closed, **Chantal Karam** for teaching me how to "float" polystyrene microspheres, **Amr Nada** and **Heba El-Maghrabi** for helping me with XRD and glass cutting. Also, I want to thank all the Lebanese girls that contributed enormously to my thesis and that always brought so many sweets: **Maryline Nasr** for telling me that there is a light at the end of the tunnel (PhD), **Sara Kawrani** for teaching me over and over how to properly use the oven and for being always happy in the lab, **Syreina Al Sayegh** for helping me with the ALD and XRD every time that I needed them and for all the laughs, **Marleine Tamer** for always preparing delicious food and singing Shakira songs with me and keeping an eye on the things we needed to order in the lab, **Maya Abdallah** for always smiling and laughing at Sakthi's jokes, and **Cynthia Farha** for making me listen to gorgeous Lebanese music. I want to thank **Matthieu Weber** for sharing with me his knowledge on ALD and ellipsometry and for reading and correcting my English and French documents. Also, I want to thank **Habib Belaid** for all the 3D printed things that I needed for my experiments, all the traveling together, and all the parties at his place. I thank **Ana Bortolassi** for all the fantastic time we spent together and some of the funniest parties I have been to. I want to thank as well **Mona Semsarilar** for all the fruitful discussions we had about pretty much everything and for all the pieces of advice for becoming a successful researcher.

I thank my friends at the IEM **Cyril Oberlin**, **Thomas Babut**, **Marianne Benoit**, **Marine Harguindeguy**, **Carmen Montoro**, and **Nazym Tuleushova** for all the support and the fantastic time we spent together in the lab and outside the lab. I thank as well all the people whom I shared my office with during almost three years **Lucie Ries**, **Marie-Jo Valero**, **Damien Alligier**, **Oleksandra Ganzenko**, and **Kevin Turani-I-Belloto** for all the nice discussions and the delicious cookies.

As Spanish is my mother tongue, I felt the need to find people whom I could talk to in Spanish. I did not know that I was about to meet some of the kindest and funniest people in my life. I want to thank **Dánae González** for helping me since the first day I started to work in the lab and for bringing me the most delicious fruits from Spain, **Enrique Folgado** for making me laugh every single day and for bringing something sweet to each of the birthday parties in the lab, **Carlos Castilla** for being an awesome roommate and for lending me his PS4 games, and **Sofía Dominguez** for all the RuPaul discussions and all the Citadelles nights you hosted at your apartment. I thank you all for all the trips we made together, all the new Spanish words I learned, birthday presents, laughs, and delicious food. All four of you made my time in Montpellier one of the best in my life. I am sure we will have more adventures together, and hopefully, we will go to México soon.

I want to thank as well all the people outside of the lab that kept me company throughout these three years in Montpellier by organizing dinners and hikes: **Anne-Sophie Bonnet-Lebrun**, **Alexis Lemaire**, **Rémi Patin**, **Laure Olazcuaga**, **Linda Slaim**, **Francisco Zuloaga**, **Rose Joubert**, **Jennifer Sok**, **Victor Cazalis**, **Thomas Aubier**, and **Francisco Rivero**.

My family has been there for me during the ups and downs of this thesis. I want to thank my mom for considering me for her trips around the world, and my dad for listening to all of the stories about my adventures in France. I want to thank my siblings for making me laugh every time I needed it and for keeping company to my parents.

México has never left me and, as proof, I can say that my relationship with two of my best friends has remained steady. I have to thank **Bárbara Ramírez** for the memorable trips to India and Malaysia and for all the unconditional support. I also thank **Alonso García** for his hospitality and his spiritual support. I want to thank **Bei Bei** for the many gifts that came unexpectedly and his support throughout my thesis.

Last but not least, I want to thank **Sylvain Lamure** for his unconditional love, enormous support, and for always comforting me during the most challenging times.

Octavio Graniel Tamayo
Montpellier, December 2019

Contents

List of acronyms

1D	One dimensional
3D	Three dimensional
AAO	Anodic aluminum oxide
AFM	Atomic force microscopy
AgFON	Silver film-over-nanospheres
ALD	Atomic layer deposition
ALE	Atomic layer epitaxy
APTES	3-aminopropyltriethoxy silane
BE	Binding energy
BEL	Band-edge laser
BSA	Bovine serum albumin
CaDPA	Calcium dipicolinate
CCD	Charge coupled device
CE	Chemical enhancement
ChO$_x$	Cholesterol oxidase
CNT	Carbon nanotube
CVD	Chemical vapor deposition
DC	Direct current
DEZ	Diethylzinc
DI	Deionized
DLE	Deep level deffect emission
DPV	Differential pulse voltammetry
E-beam	Electron beam
EDX	Energy-dispersive X-ray spectroscopy
EF	Enhancement factor
EIS	Electrochemical impedance spectroscopy
EM	Electromagnetic enhancement
FET	Field effect transistor
FFT	Fast Fourier transform
FIB	Focused ion beam
FON	Film-over-nanospheres
FWHM	Full width at half maximum
GMR	Giant magnetoresistance
GO$_x$	Glucose oxidase
GSH	Tripeptide reduced glutathione

GST	Glutathione S-transferase
GVA	*Grapevine virus A-type*
H441	Human adenocarcinoma epithelial
HAADF	High-angle annular dark-field
HmiM	2-Methylimidazole
HR	High-resolution
HRIL	High refractive index layer
ICDD	International Centre for Diffraction Data
ICP	Inductively coupled plasma
IgG	Immunoglobulin G
IL-10	Interleukin-10
ITO	Indium tin oxide
LB	Lysogeny broth
LED	Light-emitting diode
LOD	Limit of detection
LPG	Long-period grating
LPS	Lipopolysaccharide
LSPR	Localized surface plasmon resonance
MACE	Metal-assisted chemical etching
MBE	Molecular beam epitaxy
MEF	Metal-enhanced fluorescence
ML	Molecular layering
MOCVD	Metal organic chemical vapor deposition
MOF	Metal organic framework
MOS	metal-oxide-semiconductor
MOSFET	Metal oxide semiconductor field effect transistor
MQW	Multiple quantum well
NBE	Near band edge emission
NPG	Nanoporous gold
NSL	Nanosphere lithography
NW	Nanowire
PBS	Phosphate buffered saline
PC	Photonic crystal
PDMS	Polydimethylsiloxane
PET	Poly(ethylene terephtalate)
PL	Photoluminescence
PLD	Pulsed laser deposition
POC	Point-of-care
PSA	Prostate-specific antigen
PVD	Physical vapor deposition
RF	Radio frequency

RIE	Reactive ion etching
RSD	Relative standard deviation
SAM	Self-assembled monolayer
SAPE	Streptavidin, phycoerythrin conjugated
SAW	Surface acoustic wave
SDS	Sodium dodecyl sulfate
SEM	Scanning electron microscopy
SERS	Surface-enhanced Raman spectroscopy
SiNWs	Silicon nanowires
SPR	Surface plasmon resonance
SWV	Square wave voltammetry
TCID50	Tissue culture infective dose
TEM	Transmission electron microscopy
TESUD	11-(triethoxysilyl) undecanal
UV	Ultraviolet
UV-Vis-NIR	Ultraviolet-visible-near infrared
VLS	Vapor-liquid-solid
XPS	X-ray photoelectron spectroscopy
XRD	X-ray diffraction
ZIF	Zeolitic imidazole framework

Chapter 1

Introduction

"The coming nanometer age can, therefore, also be called the age of interdisciplinarity [1]." Heinrich Rohrer, considered one of the fathers of nanotechnology, encouraged scientists from different academic fields to combine their knowledge for developing new ways to interact with matter at the nanoscale. We have learned over the years that, long before we set out to manipulate single atoms or detect single molecules, nature had already perfected the art of biology at the nanoscale: DNA, one of the backbones of living organisms, has a diameter of roughly 2 nm. However, our ability to mimic nature has not been entirely successful. When comparing nature's elegant and effortless methods to our rather cumbersome fabrication techniques, we can unequivocally see that there is yet a wide gap waiting to be closed.

Nevertheless, a great deal of progress has been made, as we are finally approaching the limits of Moore's law, which states that the number of transistors in an integrated circuit doubles every two years, and 7 nm nodes are a reality and are available in the market [2]. Part of this progressive miniaturization comes from the combination of bottom-up and top-down approaches that combine lithographic techniques and a peculiar vapor deposition technique: atomic layer deposition (ALD).

It comes as no surprise then that almost every chip manufacturing company uses a form of this technique and that recognition to its inventor, Tuomo Suntola, has been paid by receiving numerous awards (including the 2018 Millenium Technology Award). However, the full potential of ALD has just started to be explored. A plethora of applications that touch almost every imaginable field has been demonstrated and keeps growing. As Tuomo Suntola puts it: "Let's first think what to do, and then do it [3]." We have thus set ourselves to the task of thinking what else can we do with ALD and how we can achieve it.

1.1 Atomic layer deposition

ALD is a vapor deposition technique enabling the preparation of thin film materials with high conformality and excellent control over the thickness [4–6]. Its origins can be traced back to two different places [7]. ALD was first developed by Aleskovskii during the 1960s in Russia and was referred to as molecular layering (ML) [8]. Later on, at the beginning of the 1970s in Finland, Suntola developed the atomic layer epitaxy (ALE) technique to deposit ZnS for electroluminescent displays [7, 9]. In the next decades and up to today, the route was then referred to as ALD.

ALD is based on self-limiting reactions between a gas precursor and a solid surface that allows the deposition of thin films in a layer-by-layer fashion. The ability to deposit conformal films on high aspect ratio structures, with high uniformity over large areas, at (relatively) low temperatures, has made ALD a technique of choice for the preparation of ultrathin films and a key enabling technology [4, 10, 11]. ALD allows the deposition of a wide range of materials such as oxides [4, 12], nitrides [13, 14], sulfides [15, 16], and pure elements [17–20]. These features have made ALD a relevant technique for many applications such as fuel cells [21], metal oxide semiconductor field effect transistors (MOSFETs) [22], water splitting [23] and purification [24], encapsulation [25], membranes [14], solar cells [26, 27], and batteries [28]. Also, the possibility of controlling the composition of the deposited layer by making nanolaminate or alloyed structures allows the tailoring of the chemical and physical properties of the ALD prepared materials [29, 30].

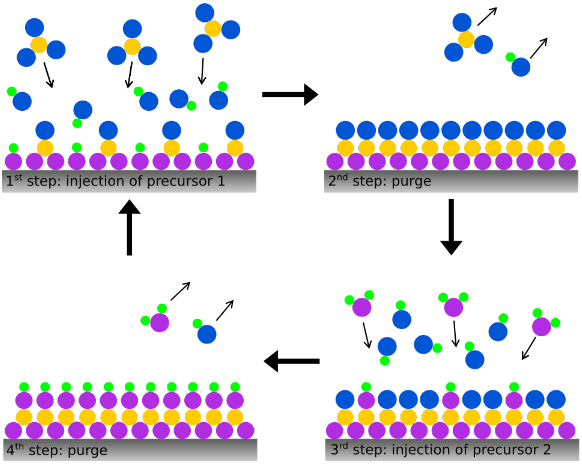

Figure 1.1: Schematic representation of the ALD process

ALD is a cycle based process involving four steps (depicted schematically in Fig. 1.1). In the first step, a precursor is introduced into the reactor chamber and is left enough time to react with the surface groups of the substrate. Next, the unreacted precursor molecules and the by-products are removed by purging/pumping the system with an inert gas (usually N_2 or Ar). The third step involves the introduction of a second precursor (the co-reactant) to react with the adsorbed molecules. The final step consists in purging/pumping again the system to remove unreacted precursor and by-products molecules. As a result, one (sub) monolayer of the desired material is deposited on the substrate surface. This cycle is then repeated until the desired thickness is obtained.

The use of ALD in the fabrication of nanomaterials for biological and medical applications has proliferated and is now widely spread [31–35]. The compatibility of ALD with the nanoscale of the components found in biomedical devices, the biocompatibility of the materials that can be deposited, and the tuning of the chemical reactivity are some of the reasons why there is a keen interest for using

ALD for biomedical applications. Among these applications, biosensing has recently benefited from ALD as a tool for the fabrication of biosensors.

1.2 Biosensors

Generally speaking, biosensors are devices that allow the selective detection of a target molecule [36], making them useful for many applications such as clinical diagnosis [37], food safety [38], environmental monitoring [39], security and bioterrorism [40, 41]. A typical biosensor configuration is presented in Fig. 1.2. Biosensors have two main components: a biorecognition layer and a physical transducer. When the analyte of interest (e.g., low molecular compound, [bio] macromolecules, protein, virus, cell) is captured by the biorecognition element, a biochemical signal is produced, and the transducer element transforms it into a signal that can be measured and correlated (in some cases) to the concentration of it.

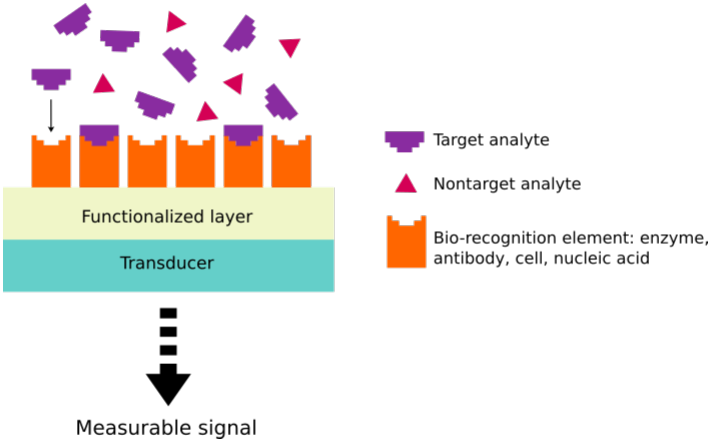

Figure 1.2: Typical biosensor configuration

Biosensors are selective thanks to the bioselective layer that interacts only with the analyte of interest. However, the robustness, sensitivity, and the detection limit of a biosensor are strongly influenced by the physical, chemical, optical, and mechanical properties of the transducer material, which can be fine-tuned by choosing a suitable material with unique architectures. Nanomaterials have become more attractive than conventional materials in the micro/macro-scale due to their high surface area and their ability to produce a stronger signal upon interaction with analytes due to their enhanced physical properties. Furthermore, the reduced size of nanomaterials can be exploited to create portable devices, reduce the volume of the sample, improve the speed of detection, and reduce the overall cost of production [42]. At the same time, as the activity of the biorecognition element depends on its structure upon attachment to the transducer layer, several immobilization strategies have been developed. For instance, enzymes can be immobilized through covalent bonding, entrapment, and cross-linking [43, 44]. Each one of these approaches presents advantages and drawbacks that are determined by the type of biorecognition element, the transducer, and the final biosensing application.

In general, biosensors can be classified either by the type of biorecognition element (e.g., enzyme, antibodies, cell, nucleic acids) or by the nature of transducer signal (i.e., electrochemical, optical, electrical, mass-sensitive, magnetic). As one of the most reported types of biosensors, optical biosensors offer numerous advantages such as direct, real-time, and label-free detection of both biological and chemical analytes. The detection in this type of biosensors is based on the interaction between the optical field and the biorecognition element [45]. Optical biosensors can be divided into label-free and label-based. In label-free mode, the signal comes directly from changes in the properties of the transducer material (e.g., photoluminescence [PL], surface plasmon resonance [SPR], ellipsometry, and surface-enhanced Raman spectroscopy [SERS]). On the other hand, in label-based biosensors, the measured optical signal comes from the attached tag (e,g., fluorescence, colorimetric, and luminescence) [46].

1.3 Motivation and outline

The primary intention of this thesis is to apply ALD in the fabrication of nanostructured transducer materials for biosensors. To this end, the combination of ALD with other nanofabrication techniques is of utmost importance and represents the core of this thesis. As briefly described in the introduction, transducer materials need imperatively to be biocompatible and, preferably, nanostructured. For this reason, ALD is one of the few techniques that allow depositing biocompatible materials with a precise thickness control, and that can be applied in different stages of the fabrication process of biosensors. Besides, ALD is a high-throughput technique that can be easily scaled up for the industrial production of biosensors, which represents a solution to one of the most significant drawbacks in the biosensing technology: the mass production of affordable and robust devices.

As one of the most mature ALD processes, the deposition of ZnO is suggested as a candidate for the fabrication of transducers. The attractive physicochemical and optical properties of ZnO, its biocompatibility with biorecognition elements, and the recent advances in its crystal growth technology are fully exploited. Also, the flexibility of ALD to either coat a pre-fabricated nanostructure to produce core-shell hybrids or to deposit a "seed" layer for the growth of defined nanostructures is explored. To illustrate this, a combination of colloidal lithography and ALD is proposed for the fabrication of core/shell structures. Likewise, a different method that combines colloidal lithography, ALD, and electrodeposition is offered for the growth of ZnO nanostructures.

Taking into consideration that the primary goal of biosensing is to obtain a precise and rapid detection of an analyte, it is safe to say that optical biosensors offer a possibility to tackle these needs. Thus, a variety of detection techniques have been developed, and their proof of concept has been demonstrated. On one hand, conventional optical methods such as absorption, reflection, or scattering provide information from changes in the incident beam of light after its interaction with a sample. On the other hand, there is another type of optical sensing that is based on the emission of light at a different wavelength than the incident one. In particular, this work focuses on photoluminescence and surface-enhanced Raman spectroscopies, which are two of the most promising optical sensing approaches. For instance, PL can be employed for sensing by exciting a sample and looking at changes in the PL spectrum upon interaction with an analyte. However, in the case of SERS, the optical signal comes directly from the inelastically scattered photons that interact with the analyte.

The motivation of this thesis is thus to provide a general overview of the flexibility and versatility of ALD for the fabrication of biosensors. Several fabrication techniques are used in combination with ALD to produce nanostructured transducers. Even though the transducer materials showed in this thesis are not fully introduced in a real biosensor device, this work envisions their application and availability to a broad range of scientific fields.

The rest of the thesis is organized as follows:

Chapter 2 presents a short survey of the various ways ALD has been used for biosensing technology. These involve nanofabrication steps, protection of the biosensor, and enhancement of the optical, chemical, and catalytical properties of the transducer material.

Chapter 3 follows the literature review by describing the fabrication and characterization techniques used for the production of nanostructured transducers. Furthermore, the experimental details for the fabrication of the two nanostructures used in this work are addressed.

Chapter 4 displays the results obtained from the fabrication of hybrid ZnO/Si core/shell structures and their possible application for PL biosensing.

Chapter 5 emphasizes on another type of high-aspect-ratio hybrid nanostructures based on ZnO and Au and their application as SERS substrates.

Chapter 6 features a set of hybrid materials that were produced by combining galvanic replacement and electrodeposition and the nanostructures from Chapter 4 and Chapter 5. Although no biosensing application is achieved, these materials have potential feasibility to do so.

References

[1] Rohrer, H. "The nanometer age: Challenge and chance." *Microelectronic Engineering* vol. 27, no. 1-4 (1995), pp. 3–15.

[2] Taiwan Semiconductor Manufacturing Company (TSMC). *7 nm Technology.* https://www.tsmc.com/english/dedicatedFoundry/technology/7nm.htm, Last accessed on 2019-06-23. 2017.

[3] People Behind the Science Podcast (PBtS). *Dr. Tuomo Suntola: Atomic Layer Deposition Developer, Fundamental Physicist, and Scientific Philosopher.* http://www.peoplebehindthescience.com/dr-tuomo-suntola, Last accessed on 2019-06-23. 2018.

[4] George, S. M. "Atomic layer deposition: An overview." *Chemical Reviews* vol. 110, no. 1 (2010), pp. 111–131.

[5] Leskelä, M. and Ritala, M. "Atomic layer deposition (ALD): From precursors to thin film structures." *Thin Solid Films* vol. 409, no. 1 (2002), pp. 138–146.

[6] Chalker, P. "Photochemical atomic layer deposition and etching." *Surface and Coatings Technology* vol. 291 (2016), pp. 258–263.

[7] Puurunen, R. L. "A short history of atomic layer deposition: Tuomo Suntola's atomic layer epitaxy." *Chemical Vapor Deposition* vol. 20, no. 10-12 (2014), pp. 332–344.

[8] Malygin, A. A. et al. "From V. B. Aleskovskii's "Framework" Hypothesis to the Method of Molecular Layering/Atomic Layer Deposition." *Chemical Vapor Deposition* vol. 21, no. 10-11-12 (2015), pp. 216–240.

[9] Suntola, T. and Antson, J. *Method for producing compound thin films.* 1977.

[10] Leskelä, M. and Ritala, M. "Atomic Layer Deposition Chemistry: Recent Developments and Future Challenges." *Angewandte Chemie International Edition* vol. 42, no. 45 (2003), pp. 5548–5554.

[11] Ritala, M. and Leskelä, M. "Atomic layer deposition." *Handbook of Thin Films.* Elsevier, 2002, pp. 103–159.

[12] Hämäläinen, J., Ritala, M., and Leskelä, M. "Atomic Layer Deposition of Noble Metals and Their Oxides." *Chemistry of Materials* vol. 26, no. 1 (2014), pp. 786–801.

[13] Kim, H. "Atomic layer deposition of metal and nitride thin films: Current research efforts and applications for semiconductor device processing." *Journal of Vacuum Science & Technology B: Microelectronics and Nanometer Structures* vol. 21, no. 6 (2003), p. 2231.

[14] Weber, M. et al. "Boron nitride nanoporous membranes with high surface charge by atomic layer deposition." *ACS Applied Materials & Interfaces* vol. 9, no. 19 (2017), pp. 16669–16678.

[15] Meng, X. et al. “Atomic Layer Deposition of Aluminum Sulfide: Growth Mechanism and Electrochemical Evaluation in Lithium-Ion Batteries.” *Chemistry of Materials* vol. 29, no. 21 (2017), pp. 9043–9052.

[16] Peters, A. W. et al. “Atomically Precise Growth of Catalytically Active Cobalt Sulfide on Flat Surfaces and within a Metal–Organic Framework via Atomic Layer Deposition.” *ACS Nano* vol. 9, no. 8 (2015), pp. 8484–8490.

[17] Aaltonen, T. et al. “Atomic layer deposition of noble metals: Exploration of the low limit of the deposition temperature.” *Journal of Materials Research* vol. 19, no. 11 (2004), pp. 3353–3358.

[18] Johnson, R. W., Hultqvist, A., and Bent, S. F. “A brief review of atomic layer deposition: From fundamentals to applications.” *Materials Today* vol. 17, no. 5 (2014), pp. 236–246.

[19] Lim, B. S., Rahtu, A., and Gordon, R. G. “Atomic layer deposition of transition metals.” *Nature Materials* vol. 2, no. 11 (2003), pp. 749–754.

[20] Weber, M. J. et al. “Atomic layer deposition of high-purity palladium films from Pd(hfac)$_2$ and H_2 and O_2 Plasmas.” *The Journal of Physical Chemistry C* vol. 118, no. 16 (2014), pp. 8702–8711.

[21] Gong, Y. et al. “Stabilizing Nanostructured Solid Oxide Fuel Cell Cathode with Atomic Layer Deposition.” *Nano Letters* vol. 13, no. 9 (2013), pp. 4340–4345.

[22] Hong, Y. et al. “Highly selective ZnO gas sensor based on MOSFET having a horizontal floating-gate.” *Sensors and Actuators B: Chemical* vol. 232 (2016), pp. 653–659.

[23] Ho, T. A. et al. “Metallic Ni 3 S 2 Films Grown by Atomic Layer Deposition as an Efficient and Stable Electrocatalyst for Overall Water Splitting.” *ACS Applied Materials & Interfaces* vol. 10, no. 15 (2018), pp. 12807–12815.

[24] Weber, M. et al. “Novel and Facile Route for the Synthesis of Tunable Boron Nitride Nanotubes Combining Atomic Layer Deposition and Annealing Processes for Water Purification.” *Advanced Materials Interfaces* vol. 5, no. 16 (2018), p. 1800056.

[25] Black, A. et al. “Encapsulating Chemically Doped Graphene via Atomic Layer Deposition.” *ACS Applied Materials & Interfaces* vol. 10, no. 9 (2018), pp. 8190–8196.

[26] Elias, J. et al. “Urchin-inspired zinc oxide as building blocks for nanostructured solar cells.” *Nano Energy* vol. 1, no. 5 (2012), pp. 696–705.

[27] Van Delft, J. A., Garcia-Alonso, D., and Kessels, W. M. “Atomic layer deposition for photovoltaics: Applications and prospects for solar cell manufacturing.” *Semiconductor Science and Technology* vol. 27, no. 7 (2012).

[28] Liu, J. et al. “Rational Design of Atomic-Layer-Deposited LiFePO4 as a High-Performance Cathode for Lithium-Ion Batteries.” *Advanced Materials* vol. 26, no. 37 (2014), pp. 6472–6477.

[29] Chaaya, A. A. et al. "Tuning optical properties of Al_2O_3/ZnO nanolaminates synthesized by atomic layer deposition." *The Journal of Physical Chemistry C* vol. 118, no. 7 (2014), pp. 3811–3819.

[30] Gu, Y.-Z. et al. "Optical and microstructural properties of ZnO/TiO_2 nanolaminates prepared by atomic layer deposition." *Nanoscale research letters* vol. 8, no. 1 (2013), p. 107.

[31] Guo, D. J. et al. "GaN nanowire functionalized with atomic layer deposition techniques for enhanced immobilization of biomolecules." *Langmuir* vol. 26, no. 23 (2010), pp. 18382–18391.

[32] Marichy, C., Bechelany, M., and Pinna, N. "Atomic layer deposition of nanostructured materials for energy and environmental applications." *Advanced Materials* vol. 24, no. 8 (2012), pp. 1017–1032.

[33] Pessoa, R. et al. "TiO_2 coatings via atomic layer deposition on polyurethane and polydimethylsiloxane substrates: Properties and effects on *C. albicans* growth and inactivation process." *Applied Surface Science* vol. 422 (2017), pp. 73–84.

[34] Vähä-Nissi, M. et al. "Antibacterial and barrier properties of oriented polymer films with ZnO thin films applied with atomic layer deposition at low temperatures." *Thin Solid Films* vol. 562 (2014), pp. 331–337.

[35] Zhang, K. et al. "Sr/ZnO doped titania nanotube array: An effective surface system with excellent osteoinductivity and self-antibacterial activity." *Materials and Design* vol. 130 (2017), pp. 403–412.

[36] Turner, A. P. F. "Biosensors: sense and sensibility." *Chemical Society Reviews* vol. 42, no. 8 (2013), p. 3184.

[37] Fu, X. et al. "A SERS-based lateral flow assay biosensor for highly sensitive detection of HIV-1 DNA." *Biosensors and Bioelectronics* vol. 78 (2016), pp. 530–537.

[38] Luo, J. et al. "Disposable bioluminescence-based biosensor for detection of bacterial count in food." *Analytical Biochemistry* vol. 394, no. 1 (2009), pp. 1–6.

[39] Mishra, A., Kumar, J., and Melo, J. S. "An optical microplate biosensor for the detection of methyl parathion pesticide using a biohybrid of Sphingomonas sp. cells-silica nanoparticles." *Biosensors and Bioelectronics* vol. 87 (2017), pp. 332–338.

[40] Liu, S. et al. "Detection of Abrin by Electrochemiluminescence Biosensor Based on Screen Printed Electrode." *Sensors* vol. 18, no. 2 (2018), p. 357.

[41] Muhammad-Tahir, Z. and Alocilja, E. C. "A conductometric biosensor for biosecurity." *Biosensors and Bioelectronics* vol. 18, no. 5-6 (2003), pp. 813–819.

[42] Li, J. and Wu, N. *Biosensors Based on Nanomaterials and Nanodevices.* CRC Press, 2014, p. 517.

[43] Putzbach, W. and Ronkainen, N. “Immobilization Techniques in the Fabrication of Nanomaterial-Based Electrochemical Biosensors: A Review.” *Sensors* vol. 13, no. 4 (2013), pp. 4811–4840.

[44] Nguyen, H. H. et al. “Immobilized Enzymes in Biosensor Applications.” *Materials* vol. 12, no. 1 (2019), p. 121.

[45] Damborsky, P., Vitel, J., and Katrlik, J. “Optical biosensors.” *Essays In Biochemistry* vol. 60, no. 1 (2016), pp. 91–100.

[46] Tereshchenko, A. et al. “Optical biosensors based on ZnO nanostructures: Advantages and perspectives. A review.” *Sensors and Actuators B: Chemical* vol. 229, no. February (2016), pp. 664–677.

Chapter 2

ALD for biosensing applications*

ALD has proven to be a versatile technique to fabricate nanostructures [1–4]. The precise thickness control and excellent conformality allowed by the technique enables to fabricate complex nanostructures with a high surface area that can be used for the design of biosensors. Some of the films deposited by ALD can function as sacrificial layers that can be removed later by chemical or physical etching to produce the desired nanostructure. Other films can be used to fabricate the transducer element of a biosensor, which requires biocompatible materials that can interact with the bio-recognition elements. Additionally, they can be used to protect biosensors and improve their stability towards harsh environments. In this chapter, ALD films deposited by ALD used in combination with other techniques for nanofabrication will be discussed.

2.1 ALD to produce nanostructured biosensors

Recently, the interest in fabricating biosensors with nano-sized features has grown because their dimensions are in the same range as the biological components of the bio-recognition layer. A selection of nanostructured biosensors fabricated using ALD is presented in Table 2.1. Jang *et al.* deposited a film of Al_2O_3 by ALD to be used as a sacrificial layer for the fabrication of a vertical nanogap in a label-free electrical biosensor for the detection of streptavidin [5]. Al_2O_3 films of 5 nm, 10 nm and 15 nm were deposited to explore the effect on sensitivity from different gap sizes. Fig. 2.1 shows the vertical nanogap fabricated with 5 nm of Al_2O_3 and 2 nm of Ti. By comparing the ratio of the current before and after binding of streptavidin to biotin, they found out that the 7 nm gap is too small for the binding to take place (no change in current). However, they observed significant current increases for the 12 nm and 17 nm gaps. Similarly, Im *et al.* combined nanosphere lithography (NSL) and ALD for the fabrication of a periodic array of ring-shaped nanocavities with 10 nm gap size to be used as a SERS substrate [6]. Fig. 2.2 presents a schematic representation of the fabrication process. The number of ALD cycles controls the thickness of the Al_2O_3 layer and this, in turn, controls the resulting gap size. Adenine was used as an analyte to test the film-over-nanospheres (FON) substrate "FON-gap." SERS measurements revealed a strong $731\,\mathrm{cm}^{-1}$ purine stretch coming from adenine that was used to test the detection limits of the SERS substrate. A 76 nM detection limit was obtained, which makes the FON-gap an excellent bioanalytical platform for SERS biosensing.

---

[*] This chapter has been published as: O. Graniel, M. Weber, S. Balme, P. Miele, M. Bechelany, Atomic layer deposition for biosensing applications, *Biosensors and Bioelectronics*, 122 (2018) 147–159. doi:10.1016/j.bios.2018.09.038.

Table 2.1: Examples of films deposited by ALD for the fabrication of nanostructured biosensors

Material	Application	Substrate	Analyte	Detection Method	Detection range	Ref.
Al_2O_3	Sacrificial layer for nanogap fabrication	Gold nanogap/Biotin	Streptavidin	Electrochemical (current)	Detection down to 1.5 nM	[5]
Al_2O_3	Layer for nanoring fabrication	Plasmonic nanoring cavities	Adenine	Optical (SERS)	Limit of detection 76 nM	[6]
Al_2O_3	Layer for coax fabrication	Nanoscale coaxial electrodes/anti-cholera toxin antibody	Cholera toxin	Electrochemical (differential pulse voltammetry [DPV] or square wave voltammetry [SWV])	Linear dynamic range of detection of 0.01 µg/ml to 1 µg/ml Limit of detection 2 ng/ml	[7]
Al_2O_3	Nano-spacer for metal-enhanced fluorescence (MEF)	Microarray platform on Ag film/split DNA aptamer	17-β-estradiol	Optical (fluorescence)	Detection limit of 1 pg/ml	[8]
Al_2O_3/ ZnO	Nanopore size modification, enhancement of sensing capabilities	poly(ethylene terephthalate) (PET) nanochannel/Al_2O_3/ ZnO/biotin	Avidin, streptavidin, bovine serum albumin (BSA), IgG, anti-BSA	Electrochemical (current)	Avidin and streptavidin discrimination/ BSA, IgG and anti-BSA detection	[9]
ZnO	Decoration of silicon nanowires (SiNWs) with ZnO nanoparticles	SiNWs FETs (field effect transistor)/chemical receptors	Explosive chemical species	Electrochemical (FET)	Detection down to the parts-per-quadrillion range	[10]

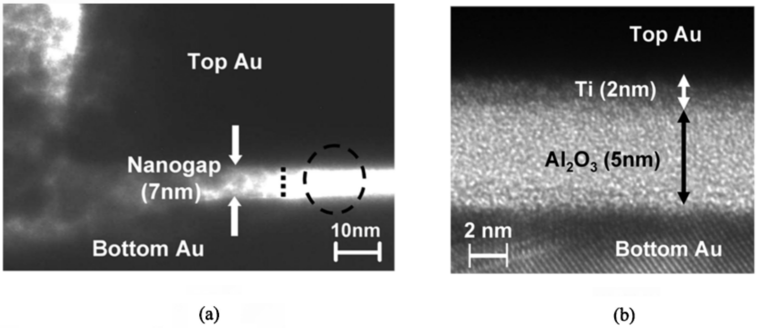

Figure 2.1: (a) Cross-sectional transmission electron microscopy (TEM) images of a 7 nm vertical gold nanogap. Vertical line is an interfacial boundary of Al_2O_3 and air, which is filled with Pt for TEM analysis and (b) close-up view of circle in (a). Reprinted with permission from [5]. Copyright 2007 American Vacuum Society.

In order to fabricate materials with low dimensions, ALD has been used to fill high aspect ratio nanoholes of porous materials [11] such as anodic aluminum oxide (AAO) [12, 13]. Thanks to its controllable pore diameter, periodicity, and density distribution [14], AAO has been incorporated successfully as a template for biosensors fabrication. As an example, Tarish *et al.* obtained highly ordered ZnO/ZnS core/shell nanotube arrays by using ALD of ZnO and rapid thermal deposition with AAO as a template [15]. ALD has also been used as a tool for tuning single solid-state nanopore sensors. Such sensors, inspired by the pioneering work of Kasianowicz *et al.* on α-hemolysin [16], are nanometer-sized apertures fabricated in thin films that allow label-free detection of single molecules [17–19]. Thanks to its conformal deposition, ALD has been used to coat nanopores with high aspect ratio [20]. For example, Cabello-Aguilar *et al.* deposited Al_2O_3/ZnO nanolaminates to reduce the size of a hydrophobic nanopore [21]. The diameter of the nanopore was fine-tuned for α–hemolysin insertions. Al_2O_3/ZnO nanolaminates were chosen due to their low surface roughness, which prevents the collonar growth of layers that can clog the nanopore [22]. The ability of ALD to homogeneously coat the internal surface of a nanopore allows an excellent surface functionalization [23]. This capability limits the non-controlled adsorption of proteins outside the track-etched nanopore and is useful for biosensing [9]. ALD has also been used to reduce electrical noise in SiN [24] and PET [25] nanopores by coating them with a thin layer of Al_2O_3.

These examples show the relevance of ALD for the fabrication of nanostructured biosensors and its versatility to be used in combination with other fabrication techniques. The advantages of using ALD to deposit thin films can be seen in the nanometer scale features achieved in the different types of biosensors and the various morphologies that can be coated.

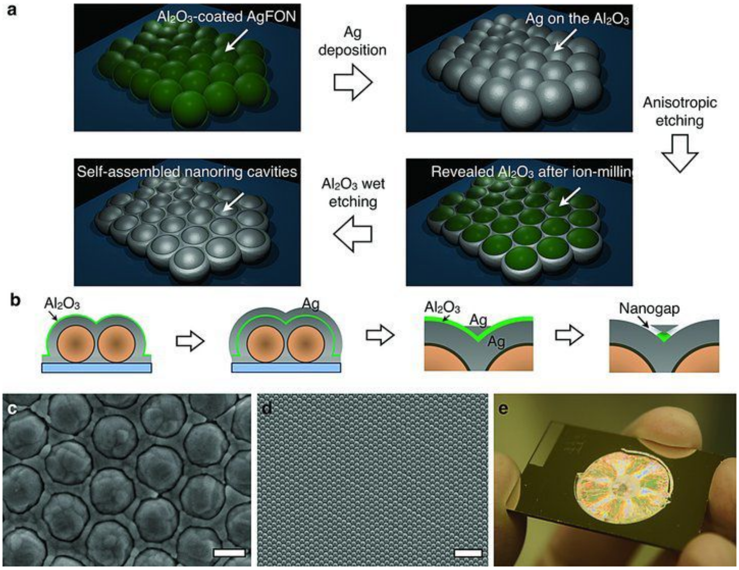

Figure 2.2: (a) A schematic representation of the fabrication process for plasmonic nanoring cavities based biosensors, using NSL and ALD. (b) Cross-sectional schematics of the fabrication process. (c) Scanning electron micrograph (SEM) of the nanoring cavities on the FON substrates. Scale bar: 200 nm. (d) SEM image of the nanoring cavity array formed over a 16 µm × 10 µm area. (e) Photograph of the nanoring cavity (FON-gap) sample. On the standard glass slide, the FON-gap structures are made in a 2 cm-wide circular area. Reprinted with permission from [6]. Copyright 2013 John Wiley and Sons.

2.2 ALD for the fabrication of transducers

In order to produce a signal that can be measured and correlated to the presence and concentration (in some cases) of a specific analyte, the transducer element of a biosensor requires well-defined morphologies with optimal optical, electrical, chemical, mechanical, and structural properties [26–28]. It is crucial that the interaction between the analyte and the biorecognition element on the transducer material produces a change in one or more of its physicochemical properties (e.g., mass change, photoluminescence change, pH change, photocurrent change). Also, the biocompatibility of the transducer element is necessary to facilitate the immobilization of the biorecognition elements [29–31]. The capabilities offered by ALD can effectively meet these challenges and examples of oxide transducers fabricated with ALD are presented in Table 2.2.

Recently, Tereshchenko *et al.* used a ZnO film deposited by ALD as an optical biosensor platform to detect *Grapevine virus A-type* (GVA) proteins (GVA-antigens) for the first time [34]. ZnO was chosen due to its high isoelectric point (∼9.5), biocompatibility for the immobilization of GVA-antibodies, and ability to change its photoluminescence (PL) emission when interacting with

Table 2.2: Examples of films deposited by ALD for the fabrication of nanostructured biosensors

Material	**Application**	**Substrate**	**Analyte**	**Detection Method**	**Detection range**	**Ref.**
TiO_x	Transducer layer	LPG/ TiO_x/ Biotin	Avidin	Optical (refractive index)	Detection of avidin-biotin complex	[32]
ZnO	Transducer layer	ZnO nanorods/ GO_x	Glucose	Electrochemical (current)	Sensitivity of 69.8 nm μM^{-1} cm^{-2}	[33]
ZnO	Transducer layer	ZnO film/GVA antibody	GVA antigen	Optical (photoluminescence)	Sensitivity in the range from 0.001 nm/ml to 10 nm/ml	[34]

biomolecules. In their work, they deposited a 110 nm thick ZnO layer on a Si substrate at a low deposition temperature of 100 °C. By looking at the PL signal of the biosensor while adding different concentrations of GVA-antigen, they detected the protein with sensitivity in the range from 0.001 nm/ml to 10 nm/ml. Kim *et al.* grew ZnO nanorods using a hydrothermal method and a seed layer deposited by ALD [33]. A 20 nm ZnO was deposited and used to promote the growth of high aspect ratio ZnO nanorods in a layer-by-layer fashion. Glucose oxidase (GO_x) was immobilized on the ZnO nanorods to detect glucose over a range of different concentrations by cyclic voltammetry. The biosensor showed a sensitivity of 69.8 nm/($\mu M\,cm^2$) for the ZnO nanorods with the highest surface area.

Transducer materials can also be functionalized chemically to immobilize the biorecognition element [35, 36]. The chemical grafting of biomolecules shows an increase of the surface coverage when compared to physical adsorption and improves the general stability and performance of the biosensor [37]. TiO_x was deposited on a long-period grating (LPG) induced in an optical fiber as a transducer for the recognition of biotin-avidin interactions [32]. The transducer layer was functionalized with amine groups to form a peptide bond with the carboxyl group of biotin. X-ray photoelectron spectroscopy (XPS) was used to confirm the successful functionalization with 3-aminopropyltriethoxy silane (APTES) as well as biotin on the TiO_x layer. A 13.2 nm shift in the resonance wavelength was obtained when binding of avidin to biotin took place, proving the biosensor's ability to detect this event.

The possibility of fabricating the transducer element in biosensors with ALD has been demonstrated in the examples mentioned above. With the growing need to fabricate biosensors with smaller dimensions, faster response rates, and higher sensitivities, the use of transducers prepared by ALD will become more common and will play a key role in the development of these devices.

2.3 ALD layers to protect biosensors from their environment

ALD deposited films have been used as protective coatings, for example, to limit corrosion processes [38–40]. The ability to coat large areas with substantial uniformity and excellent conformality are some of the advantages of ALD over other thin film deposition techniques. Also, ALD provides dense, pinhole-free films with outstanding adhesion properties [41]. These benefits have made ALD an excellent choice to protect the surface of biosensors from aqueous environments and render them stable and, in some cases, reusable. To illustrate this, a list of biosensors with protective coatings deposited by ALD is presented in Table 2.3.

Table 2.3: Examples of films deposited by ALD for biosensor protection purposes

Material	**Application**	**Substrate**	**Analyte**	**Detection Method**	**Detection range**	**Ref.**
Al_2O_3	Protection against oxidation of Ag	Silver film-over-nanosphere (AgFON)	Anthrax biomarker calcium dipicolinate (CaDPA)	Optical (SERS)	Limit of detection 1.4×10^3 spores	[42]
Al_2O_3	Protection of ZnO	ZnO passivated with Al_2O_3	Biofilm	Mass-sensitive (SAW)	Limit of detection 5.3 pg	[43]
SiO_2	Protection of nanolaser structure	InGaAsP multiple quantum well (MQW)/ biotin	SAPE	Optical (air-bridge-type Γ-BEL lasing wavelength shift)	Detection of streptavidin-biotin reaction	[44]

Cha *et al.* used ALD of SiO_2 to protect the surface of a photonic crystal (PC) band-edge laser (BEL) structure [44]. These In-P based structures are subject to chemical attack, and their surface is full of defects that can cause rapid carrier annihilation. By depositing a 5 nm SiO_2 film, they successfully protected the nanolaser device from harsh chemicals and used it as a layer for biotin functionalization. Fig. 2.3 shows the overall functionalization process schematically. Regions with PC pattern show a stronger fluorescence thanks to their higher surface to volume ratio when compared to planar regions. Also, they detected streptavidin with a figure of merit of ∼800, which showed the high sensibility of the BEL biosensor.

The sensitivity of a biosensor can be lowered when a protective layer is applied. The properties of the material to be deposited, as well as its thickness, must be optimized to reduce the possible detrimental effects on the performance of the biosensor. Kim *et al.* used an ALD Al_2O_3 film as a passivation layer to protect the ZnO piezoelectric layer from bacterial growth media or animal serum of a

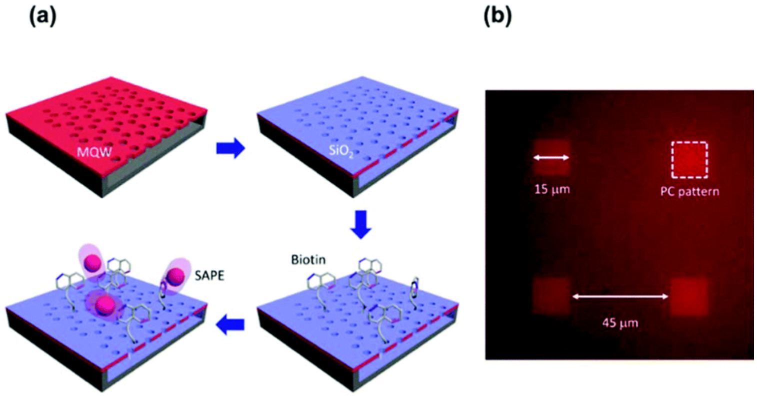

Figure 2.3: (a) Schematic representation of the surface functionalization steps for biosensing test. From top-left: 2D PC BEL fabrication; conformal deposition of ALD-SiO_2 layer; biotinylation of silica-terminated surface; and chemical interaction between biotin and streptavidin molecules tagged with streptavidin-phycoerythrin conjugate (SAPE). (b) Fluorescence microscopy image taken after the dye-conjugated streptavidin was bound onto the biotin-functionalized PC surface. Reprinted with permission from [44]. Copyright 2015 Royal Society of Chemistry.

surface acoustic wave (SAW) biofilm sensor [43]. They calculated the normalized theoretical sensitivity of the SAW sensor after applying a protective layer of different materials (Al_2O_3, Si_3N_4, SiO_2, and Teflon) and observed that Al_2O_3 was the one that provided the lowest degradation in sensitivity. A 45 nm Al_2O_3 film was deposited by E-beam evaporation, radio frequency (RF) sputtering and ALD to assess the performance of each of the deposition techniques. After two days in Lysogeny broth (LB) media bacterial suspension, the films prepared by E-beam evaporation and RF sputtering led to some damage and did not protect the ZnO layer successfully as compared to the ALD film (Fig. 2.4). *E. coli* was cultured to test the SAW sensor for biofilm growth monitoring, and a detection limit of 5.3 pm was achieved.

Zhang *et al.* deposited an ultrathin Al_2O_3 layer on a AgFON substrate for SERS detection [42]. The Al_2O_3 layer was used to protect Ag against oxidation and allows preserving an excellent sensitivity. Also, the adsorption affinity of the anthrax biomarker detected in this study for the Al_2O_3 is five times stronger than that for the AgFON alone. The SERS substrate was later used for bacillus spores detection, and a limit of detection (LOD) of $\sim 1.4 \times 10^3$ spores was attained. The SERS substrate remained functional over a period of 9 months and opens up the possibility to be used for biomedical, homeland security, and environmental applications. These examples illustrate the feasibility of ALD to deposit highly dense and conformal films for the protection of biosensors. The improved long-term stability of ALD coated devices allows them to be reused without having a detrimental impact on their sensing performance and opens up

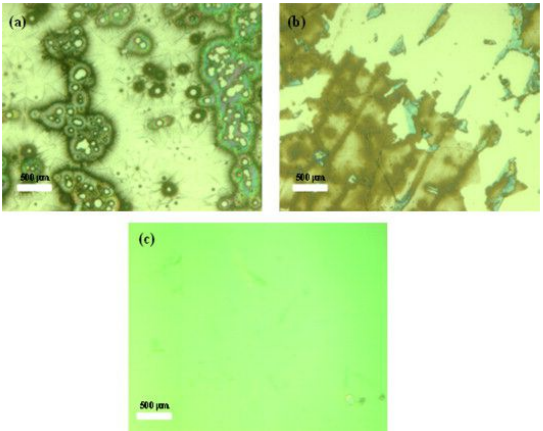

Figure 2.4: Optical images showing the surface of the SAW sensor passivated with a 45 nm Al2O3 film using (a) E-beam evaporation, (b) RF sputtering (dark area is ZnO) and (c) ALD (no ZnO damage) in LB media with the bacterial solution after two days. Reprinted with permission from [43]. Copyright 2012 Elsevier.

the possibility for biosensors to be used for *in vivo* monitoring.

2.4 Materials deposited by ALD

The properties of materials at the nanoscale strongly depend on their size, shape, chemical composition, and surface area [45, 46]. Thus, ALD has been extensively used to modify and enhance different electrical, optical, catalytical, and structural properties of biosensor materials [24, 47–49]. In order to be used in biosensing applications, the materials need to be biocompatible with the biological components of the biosensor and should not compromise the sensitivity and overall performance of these devices. Due to the popularity of FET type biosensors [50–52], most of the applications of ALD in biosensing have been focused so far on depositing high dielectric materials. Nonetheless, materials with high refractive index and high catalytic activity have also been reported. In this section, the materials deposited by ALD to fabricate biosensors have been classified by their relevant property and are showcased with a few examples.

2.4.1 Materials with high dielectric constant

ALD has been used to deposit thin films of materials with high dielectric constant to reduce leakage current, passivate surfaces and, in some cases, serve as gate dielectrics [53, 54]). Examples of high dielectric constant oxides films deposited by ALD for the fabrication of biosensors are presented in Table 2.4.

Table 2.4: Examples of materials with high dielectric constant deposited by ALD for the fabrication of biosensors

Material	Application	Substrate	Analyte	Detection Method	Detection range	Ref.
Al_2O_3	Current leakage prevention	Silicon wire FET/urease	Urea	Electrochemical (FET)	0.1 mM to 0.68 mM	[55]
Al_2O_3	Current leakage prevention	Magnetic nanoparticles/ Influenza A capture antibody	Influenza A viruses	Magnetoelectric (GMR)	Detection range of 1.5×10^2 50 % tissue culture infective dose (TCID50)/ml up to 1×10^5 TCID50/ml	[56]
Al_2O_3	Insulating layer, gate dielectric, adhesion improvement	MoS_2/anti-PSA antibody	PSA	Electrochemical (FET)	Down to 1 pg/ml	[57]
HfO_2	Gate dielectric material	Bio-FET	Biotin	Electrochemical (FET)	Biotin functionalization	[58]
HfO_2	Gate dielectric layer, protection of electrodes from liquid environment	MoS_2 nanosheet FET/monoclonal PSA	Cancer marker protein PSA	Electrochemical (FET)	Detection down to 375 fM	[59]
ZrO_2	Gate insulator	Potassium-doped polypyrrole/carbon nanotube/cholesterol oxidase (ChO_x)	Cholesterol	Electrochemical (FET)	Linear range of 0.5 mM to 20 mM Sensitivity of 400 µA/(mM mm^2)	[60]
ZrO_2	Insulating layer	Polydimethylsiloxane (PDMS) microwells/gold electrodes	Normal human dermal fibroblast and human lung adenocarcinoma epithelial (H441)	Electrochemical (impedance)	Successful cell analysis for nanotoxicological studies	[61]

One of the most used high k oxides is Al_2O_3 [62, 63]. Due to its high breakdown field and high thermal stability, Al_2O_3 deposited by ALD can successfully reduce surface leakage current [64]. Another positive aspect of this material for biosensing is the fact that Al_2O_3 films by ALD present good biocompatibility [65]. Chen *et al.* deposited a 10 nm film of Al_2O_3 to prevent current leakage between silicon nanowires and analyte solution in a FET biosensor for urea detection [55]. The Al_2O_3 film was later treated with oxygen plasma (to clean it and render its surface hydrophilic) before functionalization with APTES and urease enzyme. Krishna *et al.* developed a giant magnetoresistance (GMR) biosensor based on magnetic nanoparticles for detection of influenza A virus [56]. In their work, they deposited an 18 nm thick Al_2O_3 film onto a GMR chip to prevent current leakage.

Vello *et al.* deposited a 3.3 nm Al_2O_3 insulating film on nickel interdigitated electrodes to prevent leakage current and enable them to operate in an aqueous buffered medium [66]. To obtain this, they immersed the interdigitated electrodes coated with Al_2O_3 in a phosphate buffered saline (PBS) solution while applying 1 V to the pads of the device. The Al_2O_3 coated electrodes were functionalized with tripeptide reduced glutathione (GSH) to detect the target enzyme glutathione S-transferase (GST) by evaluating variations on the overall capacitance values. The biosensor could detect GST at concentrations as low as 200 pmol/L (the lowest value reported according to references) and could be easily regenerated to be used several times. Yoo *et al.* deposited an Al_2O_3 layer on an SU-8 organic layer to fabricate a hybrid gate dielectric in a MoS_2 FET biosensor [57]. The 30 nm Al_2O_3 layer provided high insulating properties and improved the adhesion between the organic SU-8 layer and the MoS_2/source-drain electrodes multilayer. Fig. 2.5 shows the different layers of the epidermal skin-type MoS_2 biosensor.

The flexible biochip was used for real-time detection of prostate-specific antigen (PSA) with concentrations as low as 1 pg/ml, which is much lower than the value needed for clinical trials (∼4 ng/ml). In addition, they introduced a commercial light-emitting diode (LED) to provide a direct diagnostic result, which opens up the possibility to use this type of biosensors in point-of-care (POC) and forensic applications.

Another high-κ material that has been deposited by ALD for biosensing applications is HfO_2. HfO_2 is known for its thermodynamic stability when deposited on Si, which effectively reduces leakage current and makes it suitable as a gate material for metal-oxide-semiconductor (MOS) devices [67–69]. Also, HfO_2 has an isoelectric point around pH 7 that makes it uncharged in many biological solutions and can be functionalized with biomolecules [58].

Lee *et al.* developed a biosensor based on HfO_2 for human interleukin-10 (IL-10) detection by electrochemical impedance spectroscopy (EIS) [70]. They deposited a 10.7 nm film of HfO_2 on a silicon wafer which was later functionalized with self-assembled monolayers (SAMs) of an aldehyde-silane (11-(triethoxysilyl) undecanal (TESUD)) and anti-human IL-10 mAb. By following the EIS of the modified HfO_2 with increasing human-IL-10 concentrations, they demonstrated that the biosensor had a working linear range of 0.1 pg/ml to 20 pg/ml and a

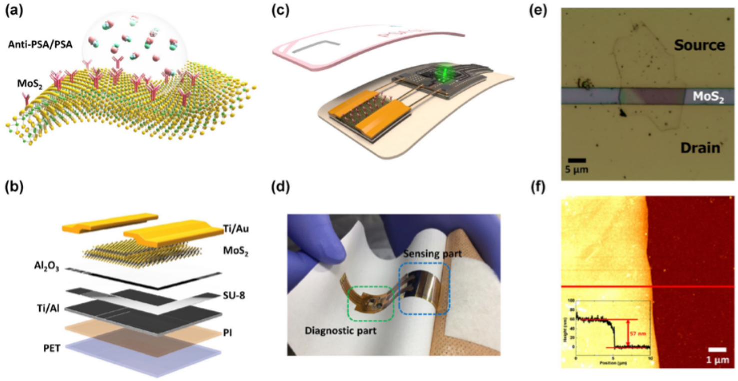

Figure 2.5: Illustration of the platform of an epidermal skin-type MoS_2. (a) Schematic of the PSA binding with the PSA antibody functionalized on the MoS_2 surface. (b) and (c) schematic layout of the 2D multilayer MoS_2 FETs. Photograph (d) of an epidermal skin-type MoS_2 biosensor system consisting of the biosensor, read-out circuits, and an LED as an indicator. (e) Optical image and (f) atomic force microscopy (AFM) image of a flexible MoS_2 device. Reprinted with permission from [57]. Copyright 2017 Springer Nature.

sensitivity of 49 ng/ml. Wang *et al.* reported a label-free MoS_2 nanosheet-based FET biosensor covered with a 7 nm to 8 nm layer of HfO_2 [59]. Fig. 2.6 shows the home-built microfluidic channel system where sample solutions were flowed to be detected by the active area. Figure 6c shows the different layers that make up the FET biosensor. They used HfO_2 to serve as the gate dielectric layer, to protect the metal electrodes from a fluidic environment, and to serve as a starting layer for functionalization with silanes. The FET biosensor showed good sensitivity (down to the femtomolar level) to cancer marker protein PSA and high selectivity by not responding to BSA protein.

Besides Al_2O_3 and HfO_2, ALD of ZrO_2 has also been reported for biosensors fabrication. Thanks to its large energy bandgap and thermodynamic stability, ZrO_2 has been considered as an alternative gate dielectric material [71–73]. Barik *et al.* deposited ZrO_2 by ALD as gate insulator on an enzyme FET biosensor [60]. They deposited ZrO_2 on the channel region of the biosensor to increase its capacitance and thus gain sensitivity. Sticker *et al.* deposited a 15 nm thick ZrO_2 insulation layer on interdigitated microelectrodes for nanotoxicological cell analysis [61]. By running computational simulations, they showed that insulated interdigitated electrode structures had an improved electrical current distribution when compared to bare electrodes. They successfully evaluated the toxicity of silica nanoparticles (with and without protein coatings) on H441 cells by monitoring the impedance signal over time. The numerous examples of biosensors that employ high-κ oxides films prepared by ALD highlight the importance of this technique for the fabrication of these devices. Moreover, the conformal and pinhole free thin films of metal oxides successfully passivate the

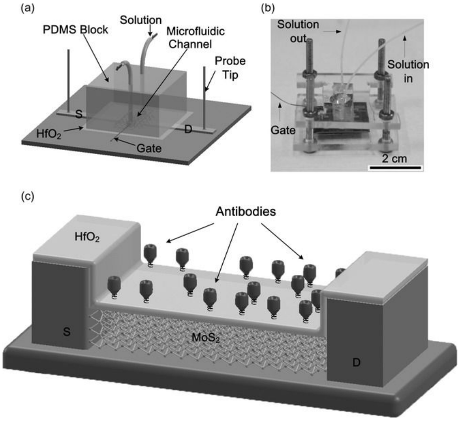

Figure 2.6: Schematic (a) and photo (b) of the biosensor configuration. (c) Schematic of the biofunctionalization layers on the device surface (S [source]; D [drain]). Reprinted with permission from [59]. Copyright 2014 John Wiley and Sons.

surface of the biosensors without loss of sensitivity and make them promising for miniaturized POC diagnostics.

2.4.2 Materials with high refractive index

Materials deposited by ALD with high refractive index have been used in optical applications [74, 75] and microelectromechanical systems [76]. Owing to the smoothness of the films and the ability to coat complex-shaped substrates with a precise thickness control, ALD has been preferred over other thin film deposition techniques like dip coating and self-assembly [77, 78]. Examples of high refractive index films deposited by ALD for the fabrication of biosensors are presented in Table 2.5.

Recently, Oubaha *et al.* deposited a Ta_2O_5 layer by ALD to increase the sensing properties of a multianalyte biosensor [79]. Ta_2O_5 was chosen due to its high refractive index, which increases the intensity of the evanescent field by 440 times when compared to the system without the high refractive index layer (HRIL). The thickness of the HRIL chosen for this work was 32 nm because it provides the maximum evanescent wave enhancement. Cy-5-labeled mouse immunoglobulin G (IgG) antibody was detected through fluorescence detection, and a limit of detection of 0.25 µg/ml0.25 µg/ml was achieved. Smietana *et al.* deposited an ALD layer of TiO_2 on LPGs for a label-free optical biosensor [80]. TiO_2 was used for improving the refractive index sensitivity of the biosensor and as a biocompatible material for endotoxin binding protein (adhesin) functionalization. The deposition of a 70 nm thick TiO_2 layer on the LPG increased the refractive index sensitivity 2.8 times when compared to the bare LPG. Binding of *E. coli* B lipopolysaccharide (LPS) to bacteria adhesion was confirmed thanks to an increase in the spectral separation of resonances.

Table 2.5: Examples of materials with high refractive index deposited by ALD for the fabrication of biosensors

Material	Application	Substrate	Analyte	Detection method	Detection range	Ref.
Ta_2O_5	Evanescent field enhancement	Waveguide-based photonic platform/ Cy5-labelled anti-mouse IgG antibody	Mouse IgG antigen	Optical (fluorescence)	Limit of detection of 0.25 µg/ml	[79]
TiO_2	Improvement of refractive index sensitivity	LPG/ TiO_2/*E. coli* B bacteriophage g37 adhesin	*E. coli* B LPS	Optical (refractive index)	Positive test for adhesin-LPS binding	[80]

2.4.3 Materials with catalytic activity

ALD has been used to improve the catalytic activity of materials thanks to its ability to precisely control the catalyst particles properties and uniform dispersion on the surface of the support [81–83]. Examples of materials with catalytic activity deposited by ALD for the fabrication of biosensors are presented in Table 2.6.

Recently, Choi *et al.* reported the decoration of carbon nanotubes (CNTs) with Ni nanoparticles by ALD for non-enzymatic glucose sensing [85]. The presence of Ni nanoparticles on CNTs was confirmed by TEM, high-angle annular dark-field (HAADF), and energy-dispersive X-ray spectroscopy (EDX). The ∼8 nm Ni nanoparticles were uniformly distributed on the walls of the CNTs. The selectivity of the sensor was confirmed by showing minimum changes in the oxidation current when adding ascorbic acid or uric acid, whereas, in the case of glucose, the value of the oxidation current was far more important. The sensor presented a detection limit of 2 µM and a linear range of 0.005 mM to 2 mM. Furthermore, it showed a rapid response and repeatability for non-enzymatic detection of glucose.

At the nanoscale, both mass transport and electron transport play a crucial role in obtaining excellent electrocatalytic properties. Nanoporous metals decorated with transition-metal oxides have been proposed as structures that can serve as electrochemical biosensors. Zhang *et al.* deposited a CoO layer on nanoporous gold (NPG) for the detection of glucose and H_2O_2 [84]. The Au nanopores with a size ranging between 40 nm to 100 nm were covered with 100 to 800 cycles of CoO. When less than 200 cycles were used, the amorphous CoO formed a discontinuous layer. On the other hand, a continuous layer was

Table 2.6: Examples of materials with catalytic activity deposited by ALD for the fabrication of biosensors

Material	Application	Substrate	Analyte	Detection Method	Detection range	Ref.
CoO	Electrode body, catalytic activity	NPG/CoO	H_2O_2	Electrochemical (current)	Linear range of detection 0.1 mM to 92.9 mM	[84]
Ni	Electrocatalyst for glucose oxidation	CNT-Ni nanocomposites	Glucose	Electrochemical (current)	Linear range of detection of 0.005 mM to 2 mM Detection limit of 2 µM	[85]
NiO	Electrocatalyst for glucose oxidation	NiO/SiC nanocomposite	Glucose	Electrochemical (current)	Linear range of detection of 0.004 mM to 7.5 mM Detection limit of 0.32 µM	[86]

observed at higher cycles. The NPG/CoO heterostructure showed an excellent electrocatalytic activity of glucose oxidation owing to the interconnected Au skeletons and the synergistic effect between Au and CoO. Furthermore, the electrochemical biosensor could detect concentrations of hydrogen peroxide (H_2O_2) as low as 0.1 mM and its sensitivity was comparable to other types of composite electrodes based on graphene sheets, noble metals, and metal oxide nanoparticles.

2.5 Conclusions and future perspectives

ALD has rapidly become a valuable technique for the fabrication of biosensors thanks to its ability to deposit a wide range of materials with precise thickness control and excellent conformality. In this minireview, the crucial role of ALD for the fabrication of different types of nanostructured biosensors and its capability to improve their sensing properties has been shown. Immobilization of biorecognition elements has also been demonstrated on layers deposited by ALD thanks to their biocompatibility and controlled chemical composition. The continuous miniaturization trend of biosensor devices and the complexity of the structures to coat demand high conformality, uniformity, and film quality that conventional thin film deposition techniques such as chemical vapor deposition (CVD) and physical vapor deposition (PVD) cannot achieve [87]. However, there are still some challenges to overcome. Conventional ALD remains a slow technique and requires mosf ot the time vacuum conditions that make the processes somewhat expensive and difficult to scale up [88]. For this reason, different approaches such as spatial atmospheric ALD [89–91], roll-to-roll systems [92, 93], and rotating reactors [94, 95] are being developed to make the process (even) more scalable and compatible with industrial requirements. Additionally, the design and synthesis of new and affordable precursors are needed to further increase the availability of materials that can be deposited. This is a difficult task given the constraints that the ALD reaction imposes on the precursors. The chemicals must be volatile at room temperature (or by being slightly heated) and thermally stable. Also, they must react quickly with the substrate to allow surface saturation and provide a fast growth [96–98].

Furthermore, while some biosensors have passed the testing phase and have become available in healthcare applications as handheld devices or portable units [99], their design must still be improved so they can diversify their applications in fields such as environmental monitoring, security and bioterrorism, and food safety. Finally, it is safe to say that ALD (in combination with other fabrication techniques) will push biosensors past the limitations they currently face by providing robust, sensible, and selective platforms that will become part of our everyday lives.

References

[1] Hong, K. J. and Kim, S. O. "Atomic layer deposition assisted sacrificial template synthesis of mesoporous TiO_2 electrode for high performance lithium ion battery anodes." *Energy Storage Materials* vol. 2 (2016), pp. 27–34.

[2] Li, X. et al. "A pressure tuned stop-flow atomic layer deposition process for MoS_2 on high porous nanostructure and fabrication of TiO_2/MoS_2 core/shell inverse opal structure." *Applied Surface Science* vol. 422 (2017), pp. 536–543.

[3] Viter, R. et al. "Tuning of ZnO 1D nanostructures by atomic layer deposition and electrospinning for optical gas sensor applications." *Nanotechnology* vol. 26, no. 10 (2015), p. 105501.

[4] Xiong, S. et al. "Atomic-layer-deposition-enabled nonwoven membranes with hierarchical ZnO nanostructures for switchable water/oil separations." *Journal of Membrane Science* vol. 493 (2015), pp. 478–485.

[5] Jang, D.-Y. et al. "Sublithographic vertical gold nanogap for label-free electrical detection of protein-ligand binding." *Journal of Vacuum Science & Technology B: Microelectronics and Nanometer Structures* vol. 25, no. 2 (2007), p. 443.

[6] Im, H. et al. "Self-assembled plasmonic nanoring cavity arrays for SERS and LSPR biosensing." *Advanced Materials* vol. 25, no. 19 (2013), pp. 2678–2685.

[7] Archibald, M. M. et al. "A nanocoaxial-based electrochemical sensor for the detection of cholera toxin." *Biosensors and Bioelectronics* vol. 74 (2015), pp. 406–410.

[8] Lee, W.-I. et al. "A smartphone imaging-based label-free and dual-wavelength fluorescent biosensor with high sensitivity and accuracy." *Biosensors and Bioelectronics* vol. 94 (2017), pp. 643–650.

[9] Lepoitevin, M. et al. "Non-Fluorescence label protein sensing with track-etched nanopore decorated by avidin/biotin system." *Electrochimica Acta* vol. 211 (2016), pp. 611–618.

[10] Lichtenstein, A. et al. "Supersensitive fingerprinting of explosives by chemically modified nanosensors arrays." *Nature Communications* vol. 5 (2014), p. 4195.

[11] Elam, J. W. et al. "Atomic layer deposition for the conformal coating of nanoporous materials." *Journal of Nanomaterials* vol. 2006 (2006), pp. 1–5.

[12] Banerjee, P. et al. "Nanotubular metal-insulator-metal capacitor arrays for energy storage." *Nature Nanotechnology* vol. 4, no. 5 (2009), pp. 292–296.

[13] Yao, Z. et al. "AAO-assisted synthesis of highly ordered, large-scale TiO_2 nanowire arrays via sputtering and atomic layer deposition." *Nanoscale Research Letters* vol. 10, no. 1 (2015), p. 166.

[14] Poinern, G. E. J., Ali, N., and Fawcett, D. "Progress in Nano-Engineered Anodic Aluminum Oxide Membrane Development." *Materials* vol. 4, no. 3 (2011), pp. 487–526.

[15] Tarish, S. et al. "Highly efficient biosensors by using well-ordered ZnO/ZnS core/shell nanotube arrays." *Nanotechnology* vol. 28, no. 40 (2017), p. 40550.

[16] Kasianowicz, J. J. et al. "Characterization of individual polynucleotide molecules using a membrane channel." *Proceedings of the National Academy of Sciences* vol. 93, no. 24 (1996), pp. 13770–13773.

[17] Dekker, C. "Solid-state nanopores." *Nature Nanotechnology* vol. 2, no. 4 (2007), pp. 209–215.

[18] Lepoitevin, M. et al. "Functionalization of single solid state nanopores to mimic biological ion channels: A review." *Advances in Colloid and Interface Science* vol. 250 (2017), pp. 195–213.

[19] Miles, B. N. et al. *Single molecule sensing with solid-state nanopores: Novel materials, methods, and applications.* 2013.

[20] Spende, A. et al. "TiO_2 , SiO_2 , and Al_2O_3 coated nanopores and nanotubes produced by ALD in etched ion-track membranes for transport measurements." *Nanotechnology* vol. 26, no. 33 (2015), p. 335301.

[21] Cabello-Aguilar, S. et al. "Slow translocation of polynucleotides and their discrimination by α-hemolysin inside a single track-etched nanopore designed by atomic layer deposition." *Nanoscale* vol. 5, no. 20 (2013), pp. 9582–9586.

[22] Balme, S. et al. "Ionic transport through sub-10nm diameter hydrophobic high-aspect ratio nanopores: Experiment, theory and simulation." *Scientific Reports* vol. 5, no. 1 (2015), p. 10135.

[23] Lepoitevin, M. et al. “Combining a sensor and a pH-gated nanopore based on an avidin-biotin system.” *Chemical Communications* vol. 51, no. 27 (2015), pp. 5994–5997.

[24] Chen, P. et al. “Atomic layer deposition to fine-tune the surface properties and diameters of fabricated nanopores.” *Nano Letters* vol. 4, no. 7 (2004), pp. 1333–1337.

[25] Thangaraj, V. et al. “Detection of short ssDNA and dsDNA by current-voltage measurements using conical nanopores coated with Al_2O_3 by atomic layer deposition.” *Microchimica Acta* vol. 183, no. 3 (2016), pp. 1011–1017.

[26] Tereshchenko, A. et al. “Optical biosensors based on ZnO nanostructures: Advantages and perspectives. A review.” *Sensors and Actuators B: Chemical* vol. 229, no. February (2016), pp. 664–677.

[27] Velasco-Garcia, M. N. and Mottram, T. “Biosensor Technology addressing Agricultural Problems.” *Biosystems Engineering* vol. 84, no. 1 (2003), pp. 1–12.

[28] Zhang, S., Wright, G., and Yang, Y. “Materials and techniques for electrochemical biosensor design and construction.” *Biosensors and Bioelectronics* vol. 15, no. 5-6 (2000), pp. 273–282.

[29] Guo, D. J. et al. “GaN nanowire functionalized with atomic layer deposition techniques for enhanced immobilization of biomolecules.” *Langmuir* vol. 26, no. 23 (2010), pp. 18382–18391.

[30] Im, H. et al. *Atomic layer deposition: A versatile technique for plasmonics and nanobiotechnology.* 2012.

[31] Schindler, M. et al. “Novel post-process for the passivation of a CMOS biosensor.” *physica status solidi (RRL) – Rapid Research Letters* vol. 2, no. 1 (2008), pp. 4–6.

[32] Dominik, M. et al. “Titanium oxide thin films obtained with physical and chemical vapour deposition methods for optical biosensing purposes.” *Biosensors and Bioelectronics* vol. 93 (2017), pp. 102–109.

[33] Kim, J. Y. et al. “Tailoring the surface area of ZnO nanorods for improved performance in glucose sensors.” *Sensors and Actuators B: Chemical* vol. 192 (2014), pp. 216–220.

[34] Tereshchenko, A. et al. “ZnO films formed by atomic layer deposition as an optical biosensor platform for the detection of Grapevine virus A-type proteins.” *Biosensors and Bioelectronics* vol. 92 (2017), pp. 763–769.

[35] Arya, S. K. et al. “Recent advances in ZnO nanostructures and thin films for biosensor applications: Review.” *Analytica Chimica Acta* vol. 737 (2012), pp. 1–21.

[36] Brétangol, F. et al. “Surface functionalization and patterning techniques to design interfaces for biomedical and biosensor applications.” *Plasma Processes and Polymers* vol. 3, no. 6-7 (2006), pp. 443–455.

[37] Gervais, L. et al. “Immobilization of biotinylated bacteriophages on biosensor surfaces.” *Sensors and Actuators B: Chemical* vol. 125, no. 2 (2007), pp. 615–621.

[38] Díaz, B. et al. “Tantalum oxide nanocoatings prepared by atomic layer and filtered cathodic arc deposition for corrosion protection of steel: Comparative surface and electrochemical analysis.” *Electrochimica Acta* vol. 90 (2013), pp. 232–245.

[39] Shang, Y. et al. “Synthesis of gold nanoparticles by reduction of $HAuCl_4$ under UV irradiation.” *Solid State Sciences* vol. 15 (2013), pp. 17–23.

[40] Standridge, S. D., Schatz, G. C., and Hupp, J. T. “Toward plasmonic solar cells: Protection of silver nanoparticles via atomic layer deposition of TiO_2.” *Langmuir* vol. 25, no. 5 (2009), pp. 2596–2600.

[41] Matero, R. et al. “Atomic layer deposited thin films for corrosion protection.” *Journal de Physique IV* vol. 09, no. PR8 (1999), Pr8–499.

[42] Zhang, X. et al. “Ultrastable Substrates for Surface-Enhanced Raman Spectroscopy: Al_2O_3 Overlayers Fabricated by Atomic Layer Deposition Yield Improved Anthrax Biomarker Detection.” *Journal of the American Chemical Society* vol. 128, no. 31 (2006), pp. 10304–10309.

[43] Kim, Y. W. et al. “An ALD aluminum oxide passivated Surface Acoustic Wave sensor for early biofilm detection.” *Sensors and Actuators B: Chemical* vol. 163, no. 1 (2012), pp. 136–145.

[44] Cha, H. et al. “Surface passivation of a photonic crystal band-edge laser by atomic layer deposition of SiO_2 and its application for biosensing.” *Nanoscale* vol. 7, no. 8 (2015), pp. 3565–3571.

[45] Bechelany, M., Balme, S., and Miele, P. “Atomic layer deposition of biobased nanostructured interfaces for energy, environmental and health applications.” *Pure and Applied Chemistry* vol. 87, no. 8 (2015), pp. 751–758.

[46] Zhang, S. et al. “Synthesis, assembly, and applications of hybrid nanostructures for biosensing.” *Chemical Reviews* vol. 117, no. 20 (2017), pp. 12942–13038.

[47] Cheun, H. et al. “Electrical and optical properties of ZnO processed by atomic layer deposition in inverted polymer solar cells.” *Journal of Physical Chemistry C* vol. 114, no. 48 (2010), pp. 20713–20718.

[48] O’Neill, B. J. et al. “Catalyst Design with Atomic Layer Deposition.” *ACS Catalysis* vol. 5, no. 3 (2015), pp. 1804–1825.

[49] Wang, G. et al. “Microwave absorption properties of carbon nanocoils coated with highly controlled magnetic materials by atomic layer deposition.” *ACS Nano* vol. 6, no. 12 (2012), pp. 11009–11017.

[50] Li, Q. et al. “Advances in Nanowire Transistor-Based Biosensors.” *Small Methods* vol. 2, no. 4 (2018), p. 1700263.

[51] Sarkar, D. et al. “MoS_2 Field-Effect Transistor for Next-Generation Label-Free Biosensors.” *ACS Nano* vol. 8, no. 4 (2014), pp. 3992–4003.

[52] Zafar, S. et al. “Silicon Nanowire Field Effect Transistor Sensors with Minimal Sensor-to-Sensor Variations and Enhanced Sensing Characteristics.” *ACS Nano* vol. 12, no. 7 (2018), pp. 6577–6587.

[53] Kim, H., Lee, H. B. R., and Maeng, W. J. “Applications of atomic layer deposition to nanofabrication and emerging nanodevices.” *Thin Solid Films* vol. 517, no. 8 (2009), pp. 2563–2580.

[54] Ponraj, J. S., Attolini, G., and Bosi, M. “Review on Atomic Layer Deposition and Applications of Oxide Thin Films.” *Critical Reviews in Solid State and Materials Sciences* vol. 38, no. 3 (2013), pp. 203–233.

[55] Chen, Y. et al. “Surface-modified silicon nano-channel for urea sensing.” *Sensors and Actuators B: Chemical* vol. 133, no. 2 (2008), pp. 593–598.

[56] Krishna, V. D. et al. “Giant Magnetoresistance-based Biosensor for Detection of Influenza A Virus.” *Frontiers in Microbiology* vol. 7 (2016), p. 400.

[57] Yoo, G. et al. “Real-time electrical detection of epidermal skin MoS_2 biosensor for point-of-care diagnostics.” *Nano Research* vol. 10, no. 3 (2017), pp. 767–775.

[58] Chen, Y. W. et al. “Atomic layer deposited hafnium oxide gate dielectrics for charge-based biosensors.” *Electrochemical and Solid-State Letters* vol. 13, no. 3 (2010), G29–G32.

[59] Wang, L. et al. “Functionalized MoS_2 Nanosheet-Based Field-Effect Biosensor for Label-Free Sensitive Detection of Cancer Marker Proteins in Solution.” *Small* vol. 10, no. 6 (2014), pp. 1101–1105.

[60] Barik, M. A. et al. “Highly Sensitive Potassium-Doped Polypyrrole/Carbon Nanotube-Based Enzyme Field Effect Transistor (ENFET) for Cholesterol Detection.” *Applied Biochemistry and Biotechnology* vol. 174, no. 3 (2014), pp. 1104–1114.

[61] Sticker, D. et al. “Zirconium dioxide nanolayer passivated impedimetric sensors for cell-based assays.” *Sensors and Actuators B: Chemical* vol. 213 (2015), pp. 35–44.

[62] Knez, M., Nielsch, K., and Niinistö, L. “Synthesis and surface engineering of complex nanostructures by atomic layer deposition.” *Advanced Materials* vol. 19, no. 21 (2007), pp. 3425–3438.

[63] Zhao, Y. et al. “Passivation mechanism of thermal atomic layer-deposited Al_2O_3 films on silicon at different annealing temperatures.” *Nanoscale Research Letters* vol. 8, no. 1 (2013), p. 114.

[64] Ye, J. et al. “Raman and photoluminescence of ZnO films deposited on Si (111) using low-pressure metalorganic chemical vapor deposition.” *Journal of Vacuum Science & Technology A: Vacuum, Surfaces, and Films* vol. 21, no. 4 (2003), pp. 979–982.

[65] Finch, D. S. et al. “Biocompatibility of atomic layer-deposited alumina thin films.” *Journal of Biomedical Materials Research - Part A* vol. 87, no. 1 (2008), pp. 100–106.

[66] Vello, T. P. et al. “Hybrid organic/inorganic interfaces as reversible label-free platform for direct monitoring of biochemical interactions.” *Biosensors and Bioelectronics* vol. 87 (2017), pp. 209–215.

[67] Aarik, J. et al. “Optical characterization of HfO_2 thin films grown by atomic layer deposition.” *Thin Solid Films* vol. 466, no. 1-2 (2004), pp. 41–47.

[68] Green, M. L. et al. “Nucleation and growth of atomic layer deposited HfO_2 gate dielectric layers on chemical oxide (Si–O–H) and thermal oxide (SiO_2 or Si–O–N) underlayers.” *Journal of Applied Physics* vol. 92, no. 12 (2002), pp. 7168–7174.

[69] Gusev, E. P., Copel, M., and Gribelyuk, M. “Ultrathin HfO_2 films grown on silicon by atomic layer deposition for advanced gate dielectrics applications.” *Microelectronic Engineering* vol. 69, no. 2-4 (2003), pp. 145–151.

[70] Lee, M. et al. “A novel biosensor based on hafnium oxide: Application for early stage detection of human interleukin-10.” *Sensors and Actuators B: Chemical* vol. 175 (2012), pp. 201–207.

[71] Kukli, K. et al. “Influence of growth temperature on properties of zirconium dioxide films grown by atomic layer deposition.” *Journal of Applied Physics* vol. 92, no. 4 (2002), pp. 1833–1840.

[72] Nam, W. H. and Rhee, S. W. “Atomic layer deposition of ZrO_2 thin films using dichlorobis[bis-(trimethylsilyl)amido]zirconium and water.” *Chemical Vapor Deposition* vol. 10, no. 4 (2004), pp. 201–205.

[73] Niinistö, L. et al. “Advanced electronic and optoelectronic materials by atomic layer deposition: An overview with special emphasis on recent progress in processing of high-k dielectrics and other oxide materials.” *Physica Status Solidi (A) Applied Research* vol. 201, no. 7 (2004), pp. 1443–1452.

[74] Alasaarela, T. et al. “Atomic layer deposited titanium dioxide and its application in resonant waveguide grating.” *Applied optics* vol. 49, no. 22 (2010), pp. 4321–5.

[75] Zhu, S. et al. “High sensitivity refractometer based on TiO_2-Coated adiabatic tapered optical fiber via ALD technology.” *Sensors* vol. 16, no. 8 (2016), p. 1295.

[76] Rissanen, A. et al. “Monolithically integrated microspectrometer-on-chip based on tunable visible light MEMS FPI.” *Sensors and Actuators A: Physical* vol. 182 (2012), pp. 130–135.

[77] Sobel, N. and Hess, C. “Nanoscale Structuring of Surfaces by Using Atomic Layer Deposition.” *Angewandte Chemie International Edition* vol. 54, no. 50 (2015), pp. 15014–15021.

[78] Zhao, Y. et al. “Refractive index sensitivity enhancement of optical fiber cladding mode by depositing nanofilm via ALD technology.” *Optics Express* vol. 21, no. 22 (2013), p. 26136.

[79] Oubaha, M. et al. “Development of a multianalyte optical sol–gel biosensor for medical diagnostic.” *Sensors and Actuators B: Chemical* vol. 221 (2015), pp. 96–103.

[80] Smietana, M. et al. “Label-free sensitivity of long-period gratings enhanced by atomic layer deposited TiO_2 nano-overlays.” *Optics Express* vol. 23, no. 7 (2015), p. 8441.

[81] Sun, S. et al. “Single-atom catalysis using Pt/graphene achieved through atomic layer deposition.” *Scientific Reports* vol. 3, no. 1 (2013), p. 1775.

[82] Weber, M. J. et al. “Sub-nanometer dimensions control of core/shell nanoparticles prepared by atomic layer deposition.” *Nanotechnology* vol. 26, no. 9 (2015), p. 094002.

[83] Weber, M. J. et al. “Supported Core/Shell Bimetallic Nanoparticles Synthesis by Atomic Layer Deposition.” *Chemistry of Materials* vol. 24, no. 15 (2012), pp. 2973–2977.

[84] Zhang, C. et al. “Electrochemical Biosensor Based on Nanoporous Au/CoO Core-Shell Material with Synergistic Catalysis.” *ChemPhysChem* vol. 17, no. 1 (2016), pp. 98–104.

[85] Choi, T. et al. “Synthesis of carbon nanotube-nickel nanocomposites using atomic layer deposition for high-performance non-enzymatic glucose sensing.” *Biosensors and Bioelectronics* vol. 63 (2015), pp. 325–330.

[86] Yang, P. et al. “NiO/SiC nanocomposite prepared by atomic layer deposition used as a novel electrocatalyst for nonenzymatic glucose sensing.” *ACS Applied Materials & Interfaces* vol. 7, no. 8 (2015), pp. 4772–4777.

[87] Crowell, J. E. “Chemical methods of thin film deposition: Chemical vapor deposition, atomic layer deposition, and related technologies.” *Journal of Vacuum Science & Technology A: Vacuum, Surfaces, and Films* vol. 21, no. 5 (2003), S88–S95.

[88] Muñoz-Rojas, D. and MacManus-Driscoll, J. “Spatial atmospheric atomic layer deposition: a new laboratory and industrial tool for low-cost photovoltaics.” *Materials Horizons* vol. 1, no. 3 (2014), pp. 314–320.

[89] Hoffmann, L. et al. “Spatial Atmospheric Pressure Atomic Layer Deposition of Tin Oxide as an Impermeable Electron Extraction Layer for Perovskite Solar Cells with Enhanced Thermal Stability.” *ACS Applied Materials & Interfaces* vol. 10, no. 6 (2018), pp. 6006–6013.

[90] Hoye, R. L. Z. et al. “Research Update: Atmospheric pressure spatial atomic layer deposition of ZnO thin films: Reactors, doping, and devices.” *APL Materials* vol. 3, no. 4 (2015), p. 040701.

[91] Poodt, P. et al. “Spatial atomic layer deposition: A route towards further industrialization of atomic layer deposition.” *Journal of Vacuum Science & Technology A: Vacuum, Surfaces, and Films* vol. 30, no. 1 (2012), p. 010802.

[92] Ali, K. et al. “High rate roll-to-roll atmospheric atomic layer deposition of Al_2O_3 thin films towards gas diffusion barriers on polymers.” *Materials Letters* vol. 136 (2014), pp. 90–94.

[93] Maydannik, P. S. et al. “Roll-to-roll atomic layer deposition process for flexible electronics encapsulation applications.” *Journal of Vacuum Science & Technology A: Vacuum, Surfaces, and Films* vol. 32, no. 5 (2014), p. 051603.

[94] Longrie, D. et al. “Thermal and Plasma-Enhanced Atomic Layer Deposition of TiN Using TDMAT and NH3 on Particles Agitated in a Rotary Reactor.” *ACS Applied Materials & Interfaces* vol. 6, no. 10 (2014), pp. 7316–7324.

[95] Sharma, K., Hall, R. A., and George, S. M. “Spatial atomic layer deposition on flexible substrates using a modular rotating cylinder reactor.” *Journal of Vacuum Science & Technology A: Vacuum, Surfaces, and Films* vol. 33, no. 1 (2015), 01A132.

[96] Johnson, R. W., Hultqvist, A., and Bent, S. F. “A brief review of atomic layer deposition: From fundamentals to applications.” *Materials Today* vol. 17, no. 5 (2014), pp. 236–246.

[97] Leskelä, M. and Ritala, M. “Atomic layer deposition (ALD): From precursors to thin film structures.” *Thin Solid Films* vol. 409, no. 1 (2002), pp. 138–146.

[98] Marichy, C., Bechelany, M., and Pinna, N. “Atomic layer deposition of nanostructured materials for energy and environmental applications.” *Advanced Materials* vol. 24, no. 8 (2012), pp. 1017–1032.

[99] Ronkainen, N. J., Halsall, H. B., and Heineman, W. R. “Electrochemical biosensors.” *Chemical Society Reviews* vol. 39, no. 5 (2010), pp. 1747–1763.

Chapter 3

Materials and methods

Following the ideas reflected in Chapter 2, this chapter is dedicated to introducing some of the underlying principles of the techniques used for the fabrication and characterization of nanostructures. By combining high-throughput methods such as colloidal lithography, physical vapor deposition (PVD), and electrodeposition, with ALD, we attain nanometer-sized structures with different compositions. Thus, the fabrication of silicon nanowires (SiNWs) and urchin-like structures are investigated and optimized to function as reliable biosensors.

3.1 Fabrication techniques

3.1.1 Atomic layer deposition

The deposition of ZnO and Pd were carried out in a home-built ALD system depicted in Fig. 3.1. The ALD reactor chamber has a circular (diameter of 83 mm) sample stage that can fit samples with a maximum height of 10 mm. This chamber is connected to an Ar line, precursor vessels, and a rotary pump that can achieve a base pressure of $\sim 10^{-2}$ mbar

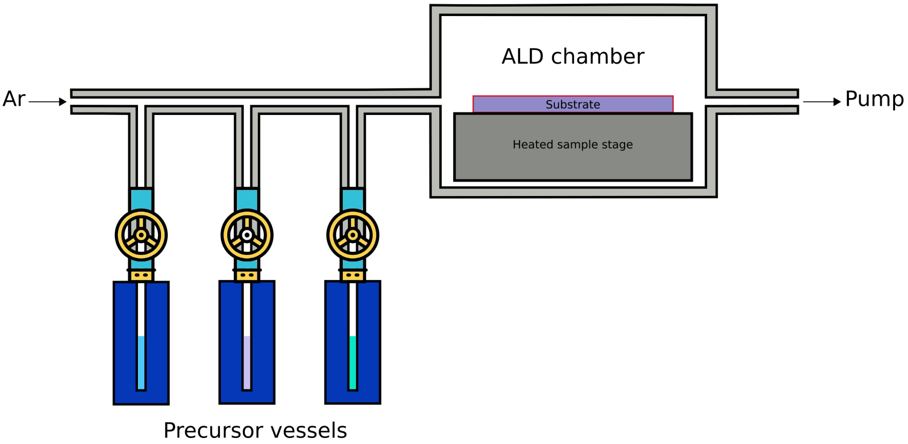

Figure 3.1: Schematic diagram of the home-built ALD system used to deposit ZnO and Pd in this work.

3.1.1.1 ZnO

Zinc oxide (ZnO) is a direct wide band gap (E_g ~3.3 eV) semiconductor with an intense near-band-edge excitonic emission at room temperature and high isoelectric point. ZnO has been grown by pulsed laser deposition (PLD) [1], molecular beam epitaxy (MBE) [2], metal organic chemical vapor deposition (MOCVD) [3], and sputtering [4]. The rising interest for using ZnO in microelectronic applications that require a though control over the growth of the film and high conformality, has paved the way for ALD to be one of the preferred techniques to deposit it. As one of the first materials to be deposited by ALD, ZnO has been prepared with different precursors, but by far the most common is diethylzinc (DEZ). DEZ reacts with water following the reaction (where * denotes surface species):

$$\mathrm{Zn(C_2H_5)_2^* + H_2O \longrightarrow ZnO^* + 2\,C_2H_6} \qquad \{1\}$$

This reaction is highly exothermic and can be used to deposit ZnO from ambient temperature up to 600 °C [5]. The reactant and co-reactant tubes connected to the ALD chamber were heated at 100 °C to avoid condensation of the precursors. The deposition was carried out at either 80 °C or 100 °C depending on the substrate to cover. Table 3.1 contains the process parameters used in this work.

Table 3.1: ALD process parameters for the deposition of ZnO.

	Pulse (s)	Exposure (s)	Ar purge (s)
DEZ	0.3	30	40
H_2O	2	30	40

3.1.1.2 Pd

The long-standing attractiveness of palladium (Pd) for catalytic applications [6] and its hydrogen storage capability [7] have been spotted by the ALD community and different approaches have been developed for its deposition [8, 9]. To date, the most used precursor for the deposition of Pd is Pd(II) hexafluoroacetylacetonate $\mathrm{Pd(hfac)_2}$. In order to use this precursor, different co-reactants such as H_2 [10] and formalin (CH_2O) [11] have been used to reduce Pd^{2+} to Pd^0. Furthermore, the use of H_2 and O_2 plasmas to provide additional surface reactivity and lower working temperatures than purely thermal processes has also been explored [12]. For this work, Pd was deposited from $\mathrm{Pd(hfac)_2}$ as reactant and formalin as co-reactant following the reaction pathway proposed by Elam *et al.* [11]:

$$\mathrm{Pd{-}H_x^* + Pd(hfac)_2 \longrightarrow Pd{-}Pd(hfac)_{2-x}^*} + x\,\mathrm{Hhfac} \qquad \{2\}$$

$$\mathrm{Pd{-}Pd(hfac)_{2-x}^* + HCOH \longrightarrow Pd{-}Pd{-}H_x^*} + 2 - x\,\mathrm{Hhfac + CO} \qquad \{3\}$$

In reaction {2}, x Hfac molecules are liberated as a result of the Pd−H reaction with one $\mathrm{Pd(hfac)_2}$. Next, the Pd(hfac) surface reacts with HCOH as displayed on reaction {3}, where the HCOH is decomposed into 2H and CO. Finally, the surface is regenerated by the reaction of H with Pd−hfac.

The $Pd(hfac)_2$ was kept in a stainless steel bubbler heated at 70 °C. The deposition of Pd was carried out at 220 °C and the tubes connecting the precursor and co-reactant were heated at 110 °C to avoid condensation. The parameters used for the deposition of Pd are displayed in Table 3.2.

Table 3.2: ALD process parameters for the deposition of Pd.

	Pulse (s)	Exposure (s)	Ar purge (s)
$Pd(hfac)_2$	5	15	10
CH_2O	1	15	60

3.1.2 Colloidal lithography

Since the first description of two-dimensional colloid crystallization by Pieranski [13], the first reported lithographic mask by Fischer [14], and the first fabrication of metallic nanostructures by R.P. van Duyne [15], the use of colloidal crystals for the fabrication of nanostructures remains a powerful and dynamic tool. A plethora of complex shapes such as nanotriangles [16], nanorings [17], nanobowls [18], nanoneedles [19], and nanowires [20] has become possible by using colloidal masks and the applications continue to grow.

Colloidal lithography, more commonly known as nanosphere lithography (NSL), is based on the deposition of spheres (polystyrene, SiO_2, PDMS, etc.) via direct assembly on a solid substrate or by liquid interface-mediated processes and their subsequent use as a lithographic mask. Each one of the two approaches to deposit the spheres presents its advantages and limitations. For instance, direct assembly on a solid substrate methods (e.g., drop casting, convective assembly, spin coating, and electrophoretic deposition) are experimentally uncomplicated and do not require fancy setups. Moreover, they can be used to prepare different colloid arrangements with substrates that are already structured. On the contrary, when liquid interface-mediated processes are used, the monolayer is not able to adapt to nanostructured substrates due to its inherent low-energy state, which prevents it from disassembling into different arrangements.

Overall, interface-mediated techniques do not suffer from the formation of undesired multilayers as the colloidal particles are formed in a liquid interface where they can assemble with the lowest free energy possible. Moreover, the composition of the subphase can be tuned to (i.e., changing the pH or adding electrolytes) promote the formation of macroscopic single crystal domains. Additionally, different types of substrates can be used as the monolayer is formed at the interface and only needs to be transferred to the surface of the substrate. However, the majority of direct assembly methods are constrained by the choice of substrate as they usually require a particular surface charge or hydrophilicity.

Indeed, the Langmuir-Blodgett technique is the most well-known interface-mediated process for colloidal crystallization [21]. This method was first conceived for the assembly of molecular monolayers and involved the controlled compression of molecular monolayers formed by spreading amphiphilic compounds at the air-water interface. Once assembled, the monolayers adhere to a hydrophilic substrate that is drawn in an upward fashion, and the process can be repeated several times to produce multiple layers. Nevertheless, this technique requires an extremely clean environment, and it is time-consuming.

To avoid the drawbacks of the Langmuir-Blodgett technique, Vogel *et al.* developed a method that involves the direct assembly of colloidal crystals at the air-water interface (Fig. 3.2). In this method, an ethanolic solution of polystyrene spheres is deposited on the surface of a glass slide that is immersed in a crystallization dish filled with water. As soon as the polystyrene spheres touch the water, they assemble into a monolayer that can be later transferred to a substrate immersed in the subphase.

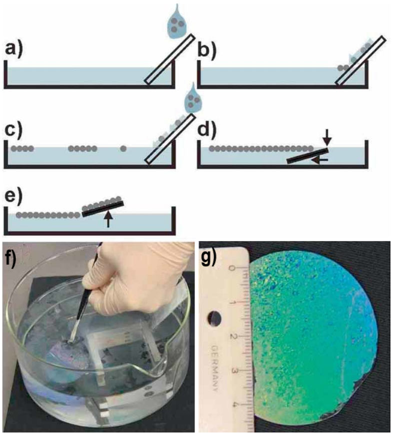

Figure 3.2: Schematic illustration and photographs of the monolayer fabrication process. a,b) Addition of colloids to the interface via a tilted glass slide, c) formation of a close-packed monolayer, d,e) monolayer transfer by immersion of the transfer substrate and subsequent elevation under a shallow angle, f) photograph of the deposition of 1 µm colloids onto the air/water interface; Individual, crystalline monolayer patches floating at the interface can be seen, g) monolayer after drying on a Si wafer. Reprinted with permission from [22]. Copyright 2011 John Wiley and Sons.

3.1.2.1 Non-close packed monolayers

The interspacing of colloidal crystals can be modified to obtain sophisticated lithographic masks that can be used in etching steps or angular evaporation to fabricate different structures from those obtained with the classical NSL method. There are two main approaches to obtain non-close packed monolayers. The first one involves the modification of a close-packed monolayer by using an etching technique or by separating the spheres with a mechanical stretching (using an elastomeric substrate). The second one uses the spin coating technique to deposit solutions of nanospheres and monomers that can be later polymerized.

By far, the size reduction of close-packed 2D colloidal crystals by etching methods such as isotropic plasma etching, anisotropic reactive ion etching (RIE), and electron beam irradiation, is the most used approach in the literature owing to its simplicity and precision [23]. Since its first introduction by Haginoya *et al.* [24], the thinning of polystyrene spheres by RIE remains a powerful tool for the fabrication of non-close packed lithographic masks [25]. Fig. 3.3 shows a schematic diagram of the RIE chamber for the etching of polystyrene spheres. By carefully choosing the size of the polystyrene spheres and the etching parameters, the final size of the polystyrene spheres and their spacing can be modified for the desired application. In general, the plasma etching process is performed at low pressures (below 10 mbar) and the plasma can be started by either by a RF source or as an inductively coupled plasma (ICP) through a coil [26]. The RIE process has four main steps: 1) generation of chemically reactive species as a result of the interaction of the generated plasma and the gas of interest; 2) chemisorption of the reactive species on the surface of the polystyrene spheres; 3) formation of the volatile reaction product; and 4) desorption of the reaction product and removal from the reaction chamber [27].

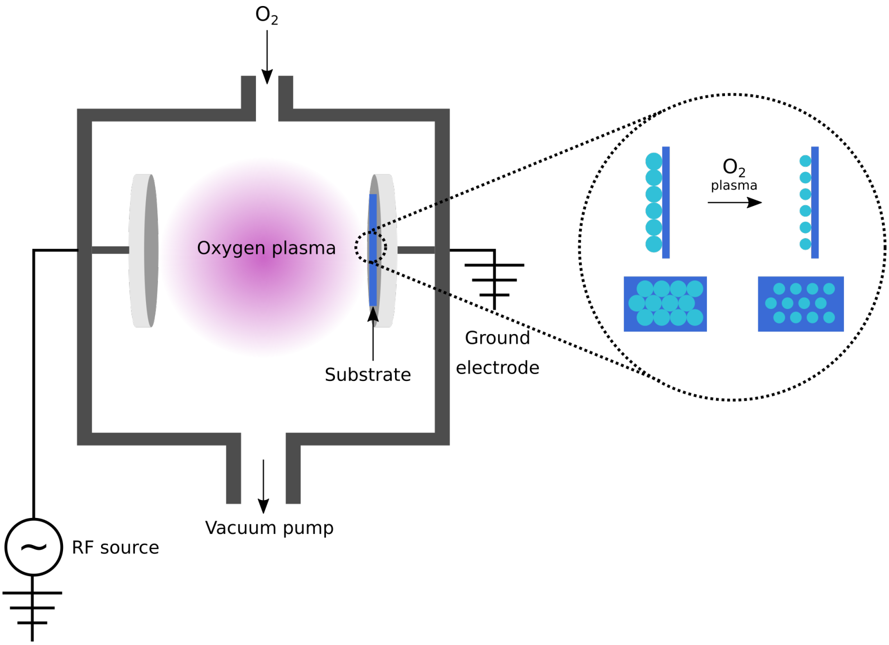

Figure 3.3: Schematic illustration of the RIE process to create a non-close packed monolayer.

3.1.3 Metal-assisted chemical etching

The fabrication of silicon (Si) nanostructures by using top-down and bottom-up approaches remains one of the most active areas in the semiconductor industry [28]. Si nanostructures have been fabricated by different methods such as RIE, vapor-liquid-solid (VLS) growth, electrochemical etching, laser ablation, molecular beam epitaxy, and metal-assisted chemical etching (MACE). First introduced by Li and Bohn [29], the MACE technique allows the fabrication of Si nanostructures with precise control on the size, length, crystallographic orientation, doping type, and doping concentration [30]. In contrast, the fabrication of large arrays of vertically-aligned Si nanostructures by using the VLS method poses a challenge due to catalyst contamination and difficult orientation control. Furthermore, the VLS method and the RIE etching introduce many crystallographic defects that affect the overall quality of the Si nanostructures.

In a traditional MACE process, a Si substrate covered by a noble metal thin film is immersed in an etching solution of hydrogen fluoride (HF) and H_2O_2). Consequently, the Si underneath the noble metal is etched faster than the one not covered by the noble metal and, depending on the initial morphology of the noble metal, Si nanopores or SiNWs are created. For example, Huang *et al.* developed a method to fabricate SiNWs by using a patterned Ag mask with defined size-pores created with NSL [31]. This NSL-based method allows controlling the final diameter of the SiNWs (by changing the parent sphere size) as well as their length (by adjusting the etching time).

Different reported models describe the chemical and electrochemical reactions that occur during the MACE process [32]. It is widely accepted that the reactions occur preferentially at the metal/etching solution interface. For simplicity, we will consider the model proposed by Huang *et al.* [28] involving a Si substrate covered by a Au mask fabricated with NSL. Fig. 3.4 displays the different process taking place during MACE. First, the reduction of the H_2O_2 occurs at the metal (cathode reaction):

$$\mathrm{H_2O_2 + 2\,H^+ + 2\,e^- \longrightarrow 2\,H_2O} \tag*{\{4\}}$$

The e^- in reaction {4} are taken from Au being dissolved:

$$\mathrm{Au^0 \longrightarrow Au^{3+} + 3\,e^-} \tag*{\{5\}}$$

Second, owing to the more electronegative character of Au when compared to Si, the Au ions are reduced back to Au^0 by taking e^- from the Si substrate. The generated holes are locally injected underneath the Au layer and they oxidize Si into SiO_2. Third, HF dissolves SiO_2:

$$\mathrm{SiO_2 + 6\,HF \longrightarrow H_2SiF_6 + 2\,H_2O} \tag*{\{6\}}$$

Fourth, the Si in contact with Au is etched at a faster rate than the bare Si substrate. Finally, the holes generated underneath the Si in contact with the noble metal are diffused to the walls of the pore.

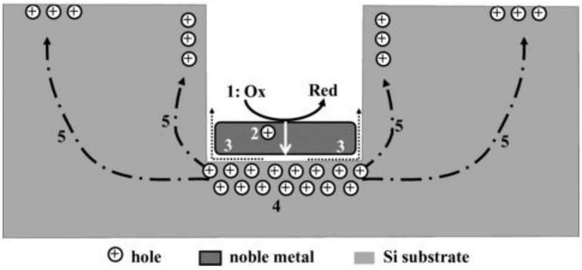

Figure 3.4: Schematic illustration of the different processes involved in MACE. The numbers indicate the steps introduced in this subsection. Reprinted with permission from [28]. Copyright 2011 John Wiley and Sons.

3.1.4 Electrodeposition

The electrodeposition technique to deposit metals (and alloys) from a solution containing ionic species has been widely used at the industrial scale for several decades and is well documented in the literature [33, 34]. In particular, this fabrication technique has been used to increase the corrosion resistance of materials, increase the conductivity in electronic components, and even for decorative purposes to imbue materials with an attractive appearance [35]. Simultaneously, the electrodeposition of semiconductors as thin films and nanostructures has found many practical applications in the field of photovoltaic solar panels and large-area display devices [36, 37].

3.1.5 ZnO

As an important semiconducting oxide material, ZnO has been electrodeposited from aqueous and non-aqueous media to form thin films, nanorods [38], flat disklike-deposits [39], and more recently, urchin-like structures [40]. To this day, the two main routes to electrodeposit ZnO are via an oxygen saturated solution [41] or a nitrate solution [42]. In general, the electrodeposition of ZnO described by Peulon and Lincot requires an oxygen-saturated solution containing the adequate concentration of $ZnCl_2$ and three electrodes, as shown in Fig. 3.5.

A cathodic potential is applied and hydroxide ions are generated at the surface of the working electrode:

$$O_2 + 2\,H_2O + 4\,e^- \longrightarrow 4\,OH^- \qquad \{7\}$$

The generated hydroxide ions react with Zn ions and ZnO is precipitated:

$$Zn^{2+} + 2\,OH^- \longrightarrow ZnO + H_2O \qquad \{8\}$$

By changing the electrochemical conditions, ZnO can be deposited with different morphologies depending on the desired application. Likewise, Elias *et al.* [43] developed a method to fabricate urchin-like nanostructures by combining NSL, ALD, and electrodeposition. In this technique, the length and diameter

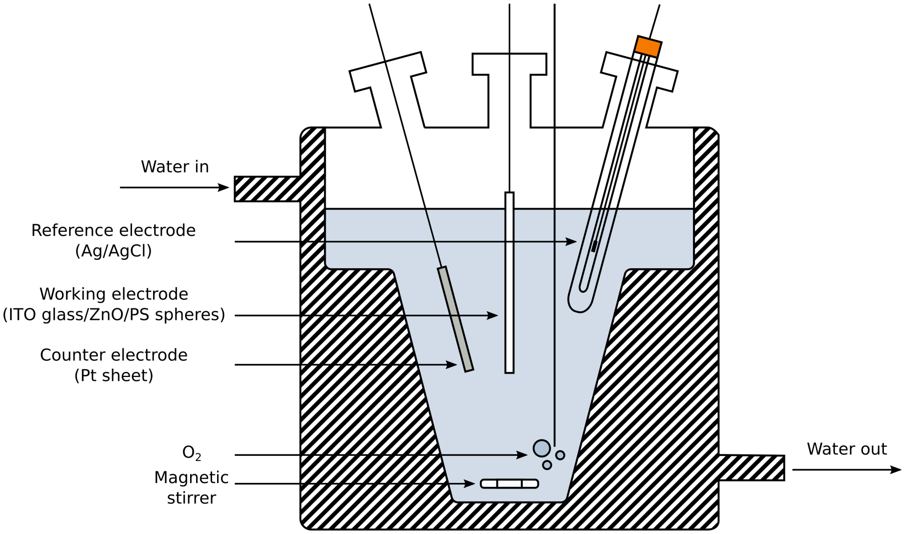

Figure 3.5: Schematic illustration of the electrochemical cell used in this work for the electrodeposition of ZnO.

of the ZnO nanowires can be tuned by changing the electrodeposition charge density and the concentration of $ZnCl_2$, respectively.

3.1.6 ZIF-8

The research interest in the electrochemical synthesis of metal organic frameworks (MOFs) has risen tremendously in the past few years. These nanoporous materials whose framework is based on metallic nodes held together by bridging organic linkers have found potential applications in gas separation [44], energy storage [45], sensing [46], and microelectronics [47]. While this might seem exciting, the majority of these applications are based on MOFs in bulk form, which hinders their use in membranes, sensors, and integration with microelectronics that require MOF crystals as thin films or coatings [48]. Recently, MOF films have been produced by means of electrochemical synthesis methods, which opens up the possibility for their large-scale production in industrial processes. The electrochemical deposition of MOFs can proceed anodically or cathodically. In the anodic approach, metal ions are introduced to a solution containing an organic ligand by electrochemically oxidizing a metal support, which produces a thin MOF film on the anodic surface [49]. In cathodic deposition, the reduction of ions (e.g., nitrates) at the cathode induces the deprotonation of organic linkers that can react with metal ions, which triggers the formation of MOFs [50]. Although attractive enough, the cathodic approach is usually accompanied by co-deposition of the corresponding metal, which is unwanted in many cases. Recently, the first cathodic deposition of a zeolitic imidazolate framework material (ZIF) was achieved by Zhang *et al.* [51]. In their method, they perform a ZIF-8 synthesis by saturating with oxygen the precursors solution of $ZnCl_2$ and imidazole organic ligands in methanol (Fig. 3.6).

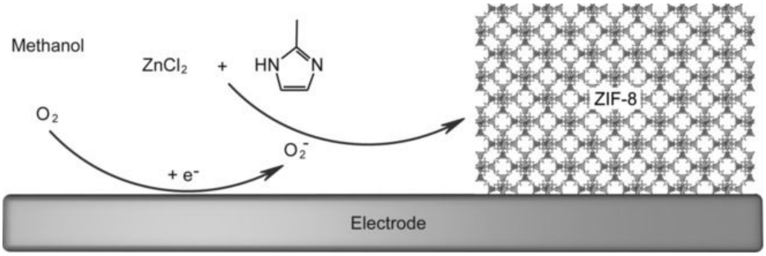

Figure 3.6: Schematic illustration of the oxygen mediated cathodic deposition of ZIF-8. Reprinted with permission from [51]. Copyright 2019 John Wiley and Sons.

This oxygen-triggered approach allows depositing large-area uniform ZIF-8 films while avoiding the plating of Zn metal. The proposed reaction mechanism involves the reduction of O_2 to ${O_2}^-$ on the electrode surface (reaction {9}), the subsequent formation of a superoxo-Zn^{II} complex (reaction {10}), and the reaction between Zn^{II}-imidazole complexes and superoxo-Zn^{II} intermediates (reaction {11}), which finally evolve to ZIF-8 via ligand-exchange, nucleation, and crystal growth [52].

$$O_2 + e^- \longrightarrow {O_2}^- \tag{9}$$

$$Zn^{2+} + O^{2-} \longrightarrow (Zn^{2+})({O_2}^-) \tag{10}$$

$$\begin{gathered} 2\,(Zn^{2+})({O_2}^-) + 2\,[Zn(HmiM)_m L_n] \longrightarrow \\ 2\,[Zn(miM)(HmiM)_{m-1} L_n] + 2\,Zn^{2+} + H_2O_2 + O_2 \end{gathered} \tag{11}$$

3.1.7 Galvanic replacement

Bimetallic nanostructures exhibit unique catalytic, electronic, optical, and magnetic properties that set them apart from their monometallic analogs [53]. Several methods such as precipitation [54], sol-gel [55], hydrothermal [56], galvanic replacement [57], and ALD [58] have been developed to precisely control their shape, size, and composition. Among these, the galvanic replacement approach represents one of the most versatile and simple methods that enable the synthesis of bimetallic and hollow materials with a high degree of control in their composition, surface morphology, and size [59]. The galvanic replacement reaction is a spontaneous redox reaction that occurs between a metal and ions of another metal in solution. The reaction is driven by the difference in standard electrode potentials of the metals, which results in dissolution (oxidation) of one of the metals and the plating of the second metal (reduction). Recently, the galvanic replacement reaction has been exploited to produce bimetallic nanostructures based on Au and Pd for applications in catalysis [60], sensing [61], and plasmonics [62]. Given the difference in reduction potential between Au^{3+}/Au (1.4 eV) and Pd^{2+}/Pd (0.195 eV) pairs, the replacement reaction can proceed as follows:

$$3\,Pd^0 + 2\,Au^{3+} \longrightarrow 3\,Pd^{2+} + 2\,Au \qquad \{12\}$$

When a Pd nanoparticle is in contact with a Au^{3+} ion, the Pd atoms from the surface are quickly oxidized and dissolved to produce Pd^{2+} ions into the suspension reaction. At the same time, Au^{3+} are reduced and deposited on the surface of the nanoparticle. The composition of the resulting alloy can be changed by adjusting the amount of Au^{3+} ions relative to the amount of Pd metal [63].

3.1.8 Physical vapor deposition

Physical vapor deposition processes are based on the production of a condensable vapor from a material (in liquid or solid form) and its subsequent condensation in a substrate to form a thin film [64]. In general, PVD processes are used to deposit films of elements and alloys with thicknesses that go from just a few nanometers to several microns [65]. Also, the technique presents exceptional flexibility in terms of the size (which can go as large as 10 ft × 12 ft) and the geometrical complexity of substrates. Depending on the way the vapor is produced, PVD processes can be classified into vacuum deposition (evaporation), sputter deposition, arc vapor deposition, and ion plating.

3.1.8.1 Electron beam evaporation

Vacuum evaporation by electron beam (E-beam) is a PVD process where intense beams of high-energy electrons are used to vaporize materials [66]. Fig. 3.7 presents a schematic representation of an E-beam evaporation system. E-beam evaporation allows the deposition of most pure metals (even those with high melting points) and is especially suitable for refractory materials such as most ceramics (oxides and nitrides), glasses, carbon, and refractory metals [67]. Typically, the electron beams used in this technique are accelerated to high voltages (10 kV to 15 kV) and are focused by electric or magnetic fields to bombard a material contained in a crucible. To avoid the interaction between the vaporized material and the gas molecules contaminating the system, the deposition usually takes place in the range of 10^{-5} – 10^{-9} mbar. Additionally, deposition rates as high as $50\,\mu m\,s^{-1}$ can be achieved.

3.1.8.2 Sputter deposition

The sputtering phenomenon is based on the bombardment of a solid surface by high-energy ions and the resulting physical (not thermal) vaporization of atoms from the surface by the momentum transfer [68]. The sputter deposition

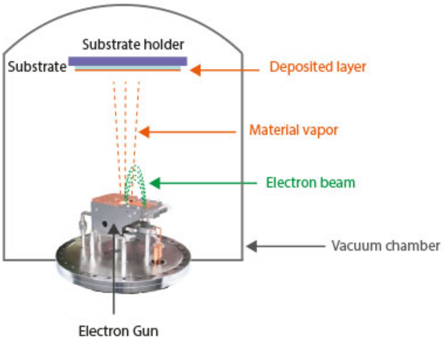

Figure 3.7: Schematic illustration of an E-beam evaporation system. Reprinted from Evaporation materials, Neyco. Retrieved June 06 2019 from https://www.neyco.fr/en/page/evaporation-materials. Copyright 2019 Neyco.

technique can be used to deposit films either by sputtering from an elemental (or an alloy) target or by sputtering from a compound target (where, in most cases, there is a loss of the more volatile material). Depending on the condition under which the sputtering is done, the process can be classified into direct current (DC), RF, magnetron, and ion beam sputtering [69]. Among these, DC sputtering presents the simplest configuration [70]. Fig. 3.8 shows a typical configuration of a DC sputtering system schematically. Generally, the DC configuration comprises a cathode (target), an anode (where the substrate to cover is placed), and a DC power source (supplying a potential between 0.5 keV to 5 keV) that are placed in a vacuum chamber at either low pressure ($<5 \times 10^{-3}$ mbar) or high pressure (5×10^{-3} mbar to 3×10^{-2} mbar). The sputtering chamber is filled with Ar, and a plasma is created (and sustained) by applying a DC voltage between the electrodes. The Ar ions generated by the glow discharge are accelerated to the negatively biased target, and sputtering of the surface of the target occurs. The sputtered species proceed in the direction of the substrate, and a thin film is formed.

3.1.9 Conclusions

In the first half of this chapter, we described nano and micro fabrication processes that combine both top-down and bottom-up approaches. These techniques, which are currently used in many well-established and emerging applications in the industry, will continue to be key players in the ongoing industrial revolution. In the next section, the underlying principle of the characterization techniques used to study the physicochemical properties of the SiNWs and urchin-like structures will be discussed.

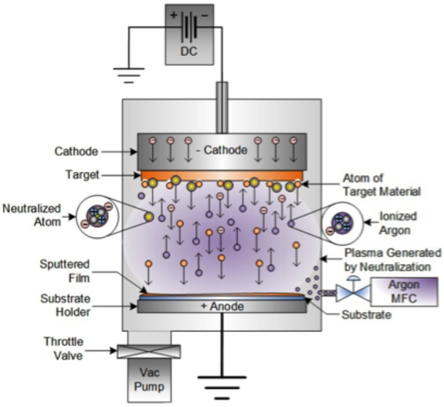

Figure 3.8: Schematic illustration of a DC sputtering evaporation system. Reprinted from What is DC sputtering?, Semicore. Retrieved June 06 2019 from http://www.semicore.com/news/94-what-is-dc-sputtering. Copyright 2019 Neyco.

3.2 Characterization methods

It is well known that, once you obtain a new material, the first thing to do is to study its physical, chemical, optical, and mechanical properties. In particular, when a novel nanomaterial is produced, the characterization and measurement of its physicochemical properties represents an interesting challenge. Similarly, when the fabrication process of a material involves several steps, careful attention must be paid between each of the stages to make sure that no problems have occurred. In the second half of this chapter, the elemental aspects of the characterization techniques that were used to study the materials fabricated in this work are introduced.

3.2.1 Scanning electron microscopy

Scanning electron microscopy (SEM) is an electron probe characterization method that uses a high-energy electron beam for imaging and chemical analysis of a material. Fig. 3.9 shows the principal components of an SEM instrument. The electron gun at the top of the column produces a beam that is focused through a series of magnetic lenses and is rastered in a squared area of the surface of a sample. The variety of signals produced by the interaction of the electrons with the sample (e.g., secondary electrons, backscattered electrons, x-rays) are detected to provide information about the topography and composition of the sample (with the aid of a solid state x-ray detector for EDX). In general, there are no complicated steps to prepare samples, and the only requirement is for the samples to be sufficiently conductive (non-conductive samples are usually coated with a thin film of Pt).

The morphology of all the samples was characterized by a Hitachi S4800 SEM.

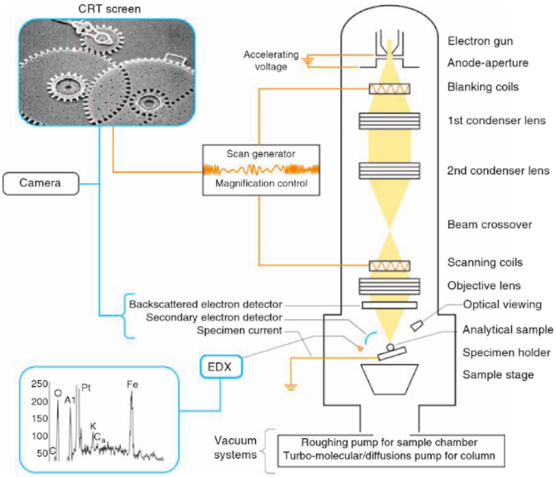

Figure 3.9: Schematic illustration of the main components of a scanning electron microscope. Reprinted with permission from [71]. Copyright 2008 Taylor & Francis.

3.2.2 Transmission electron microscopy

Transmission electron microscopy (TEM) is based on the same principles as SEM except for the detector (direct imaging on a fluorescent screen or PC screen with a charge coupled device or CCD) that is capable of capturing images generated by transmitted electrons. Fig. 3.10 shows the principal components of a TEM apparatus. Moreover, TEM uses even higher voltages than SEM (60 keV to 300 keV compared to 1 keV to 50 keV) and can achieve a spatial resolution of up to ∼50 pm (∼0.5 nm for SEM). Due to the requirement of transmitted electrons, the samples must be very thin (<150 nm for regular TEM and <30 nm for high-resolution TEM). This thinning usually involves tedious and complex preparation techniques that require a trained and experienced user. TEM experiments were performed in an HR-TEM JEOL ARM-200F, working at 200 kV, equipped with an EDX detector.

3.2.3 Atomic force microscopy

Atomic force microscopy (AFM) is another powerful imaging technique that, by scanning in a grid-like fashion an atomically sharp probe tip over a surface, can produce topographical images and also, with some modifications of the tip, allows to measure the forces of adhesion between the surface of the sample

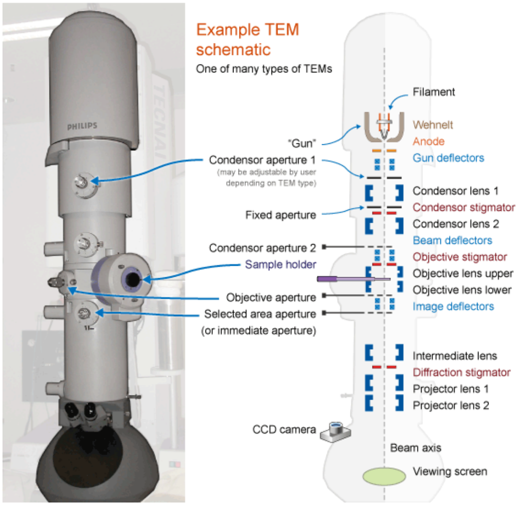

Figure 3.10: Schematic diagram of the internal structure of a transmission electron microscope. Reprinted from Basic principles of TEM operation, Microscopy Australia. Retrieved June 06 2019 from https://myscope.training/legacy/tem/introduction/. Copyright 2019 Microscopy Australia.

and the tip [72]. A generic AFM system is shown in Fig. 3.11. The sample is positioned on a piezoelectric stage that can move in the x, y, and z direction. The cantilever tip is positioned close to the surface of the sample. The stage is moved laterally to scan the desired area of the sample. As the cantilever moves over the sample, it becomes deflected due to the topography of the surface. The degree of deflection is measured by following changes in the reflected laser beam that moves on the photodetector. The distance between the cantilever and the sample is held constant by an electronic feedback control that adjusts the z-position of the sample. There are two main configurations for an AFM system. In contact mode, the tip of the cantilever remains in intimate contact with the sample while the stage is moving. This mode is appropriate for hard materials as it does not damage their surface. For weakly-bound specimens or softer materials, the tapping mode is used. In this mode, the tip of the cantilever has intermittent contact with the sample. This mode prevents damage to the sample and allows to image the amplitude and phase difference of the resonance vibration. The affinity of the tip for the surface of the sample can be used to create a chemical map based on the differences between the materials [73]. AFM was performed with a NANOMAN 5 device from Veeco, and it was controlled with the Nanoscope V software in tapping mode.

3.2.4 X-ray diffraction

X-ray diffraction (XRD) is one of the most noteworthy analytical methods to analyze the crystalline structure of materials. X-rays get diffracted because the

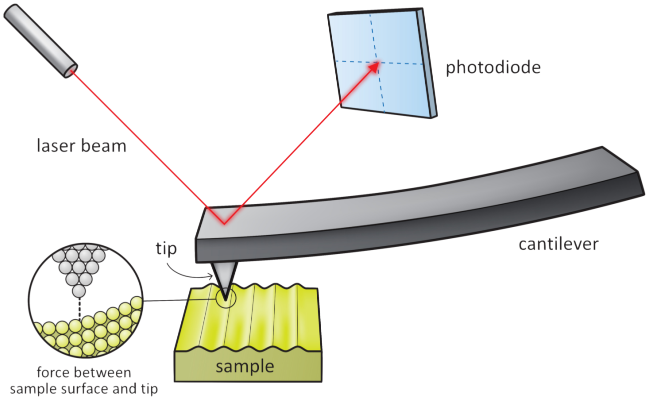

Figure 3.11: Schematic illustration of an atomic force microscope. Reprinted from Nanoscale Informal Science Education Network. Retrieved June 06 2019 from https://myscope.training/legacy/tem/introduction/. Copyright 2019 NISE network.

wavelength of x-rays is in the same order of magnitude of the spacing between atoms and planes of atoms of a crystalline compound. The diffracted x-rays provide a pattern that can be used to determine the structural orientation of the atoms in a given compound. One of the keystones of XRD is the Bragg equation:

$$n\lambda = 2d\sin\theta \tag{3.1}$$

In this equation, n is an integer (1,2,3,...n), λ is the wavelength, d is the interplanar distance between atomic planes, and θ is the angle of incidence of the x-ray beam with respect to these planes. Crystalline materials show long-range periodic structures that are displayed as Bragg diffraction peaks. In the simplest case, an XRD measurement consists of a group of intensities and the angles at which they are observed [74]. The resulting pattern represents the fingerprint of the material and can be later used for chemical identification by comparing it to diffraction patterns found in databases such as the International Centre for Diffraction Data (ICDD). For this work, XRD was performed with a PANalytical X'pert-PRO diffractometer equipped with an X'celerator detector using Ni-filtered Cu Kα radiation).

3.2.5 X-ray photoelectron spectroscopy

X-ray photoelectron spectroscopy (XPS) is technique that allows to study the surface chemistry of a material [75]. The technique involves irradiating a material in a high vacuum ($\sim 1 \times 10^{-8}$ mbar) with monochromatic or polychromatic soft x-rays and analyzing the kinetic energy of the detected electrons coming from the top 1-10 nm of the material being analyzed. The emitted electrons have measured kinetic energies given by:

$$KE = h\nu - BE - \phi_s \tag{3.2}$$

were $h\nu$ is the energy of the photon, BE is the binding energy of the atomic orbital from which the electron originates, and ϕ_s is the spectrometer work function. By counting these emitted electrons over a range of kinetic energies, a photoelectron spectrum is obtained. The position and intensity of the peaks in this spectrum enable the proper identification and quantification of the elements in the material. Changes in the chemical state of an element can be determined by shifts in the BE due to changes in the measured KE. For instance, the BE of the core electrons will increase if the valence electrons are slightly more distant to the core due to the formation of bonds with other elements [76]. XPS measurements were performed with a VG ESCALAB 250 spectrometer (ThermoFisher Scientific, Waltham, MA, USA).

3.2.6 Photoluminescence spectroscopy

Photoluminescence (PL) spectroscopy is a nondestructive characterization technique used to study the electronic structure of materials, especially for semiconductors. In some ways, the emission of photons from semiconductors is the reverse of the absorption of photons. However, emission only occurs in a narrow band of empty states that produces a spectrum much thinner than that of the absorption (which can involve all states in a semiconductor) [77]. Fig. 3.12 shows a schematic representation of the PL process.

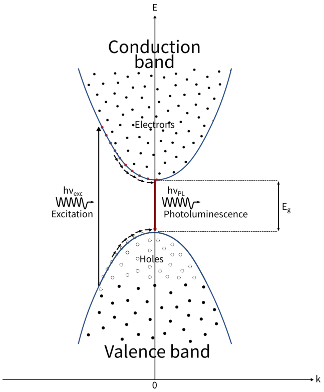

Figure 3.12: Schematic illustration of the PL process in a direct bandgap semiconductor.

In a PL spectroscopy setup, a laser beam (with energy much larger than the bandgap of the semiconductor) is directed toward a sample to generate free electrons and holes in the conduction and valence bands, respectively. These excited carriers can later relax and recombine by emitting light with the energy of the bandgap [78]. The emitted photons are dispersed with a monochromator and detected with a CCD or a photomultiplier tube. Fig. 3.13 shows a schematic representation of the experimental setup for PL spectroscopy. While it is possible to study almost all semiconductor materials with PL, only a weak signal can be measured from indirect bandgap semiconductors. Thus, for the case of direct bandgap semiconductors (e.g., ZnO) an abundant amount of information regarding their localized defects and impurities (and their concentration), optical emission efficiencies, and composition of the material (i.e., alloy composition) can be extracted by analyzing the PL spectrum.

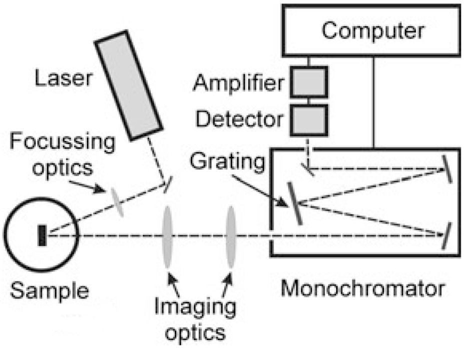

Figure 3.13: Schematic diagram of a standard PL spectroscopy setup. Reprinted with permission from [79]. Copyright 2008 Springer Nature.

3.2.7 Raman spectroscopy

3.2.7.1 Raman effect

The interaction of light with matter can result in either absorption, scattering, or no-interaction with the material (photons pass through it). The inelastic scattering of light was first described theoretically by Smekal in 1923 [80] and observed experimentally for the first time in 1928 by Raman and Krishnan [81]. In Raman spectroscopy, two types of scattering are involved. The first one is called Rayleigh scattering, and it occurs when the emitted photon has the same energy as the incident photon (elastic scattering). In the second case, the incident photon can transfer energy to the material (or vice versa), and it will be scattered with different energy (inelastic scattering). Light scattered with less energy than the incident light is called Stokes, while the one with higher energy is called anti-Stokes. Fig. 3.14 displays the elastic and inelastic light scattering processes. In the Stokes process, the material goes from a base level E_0 to virtual state with higher energy. However, in the anti-Stokes process, if the material is in an excited state E_{vib}, the scattered photon will have higher energy and the material will return to the base level E_0. At room temperature, the number of molecules in an excited state is minimal and, for this reason, the anti-Stokes process is less intense. In general, Raman spectroscopy involves only the detection of the Stokes signal [82].

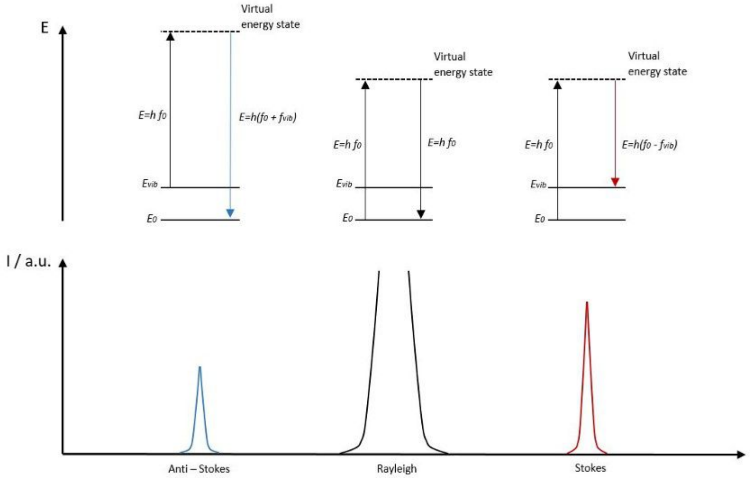

Figure 3.14: Schematic diagram of a Raman spectrum showing vibrational Raman effects. The Stokes process produces scattered light with lower energy than the incident light, while anti-Stokes produces scattered light with a higher energy than the incident light. Retrieved June 06 2019 from http://www.ltb-berlin.de/en/technologies/raman/. Copyright 2019 NISE network.

3.2.7.2 Surface-enhanced Raman spectroscopy

Surface-enhanced Raman spectroscopy (SERS) is a technique that is used to amplify by several orders of magnitude (reaching 8-9 orders of magnitude per single molecule) the Raman signals coming from a material [83]. The resulting peaks in a Raman spectrum correspond to vibrational modes of the analyte.

The effect was first observed by Fleischman *et al.* [84] and further explained firstly by Jeanmaire and Van Duyne [85] and secondly by Albrecht and Creighton [86]. The amplification effect of the Raman signal comes from two main mechanisms: electromagnetic (EM) and chemical (CE). The first involves the electromagnetic interaction of light with metals through excitations known as plasmon resonances. The second mechanism is related to changes in the polarizability of the probe due to its adsorption on the metal surface. Although both mechanisms are multiplicative, it is widely accepted that the main contribution to the enhancement comes from the EM mechanism [87]. To perform a SERS experiment, care must be taken while choosing the metallic substrate (usually Ag or Au), the characteristics of the laser excitation (e.g., wavelength), and the adsorption properties of the analyte. In general, Au and Ag are the two most used metals for the fabrication of SERS substrates [88] due to their optical properties (their plasmon resonances are in the visible/infrared) and their ease of manipulation for preparing nanostructures.

In this work, Raman measurements were performed with an InVia Raman spectrometer equipped with three different lasers (532 nm, 633 nm, and 785 nm) and an optical microscope with various objectives (50 × – 0.50 NA and 100 × – 0.9 NA) in backscattering geometry. Fig. 3.15 shows a schematic representation of the Raman spectrometer used in this work.

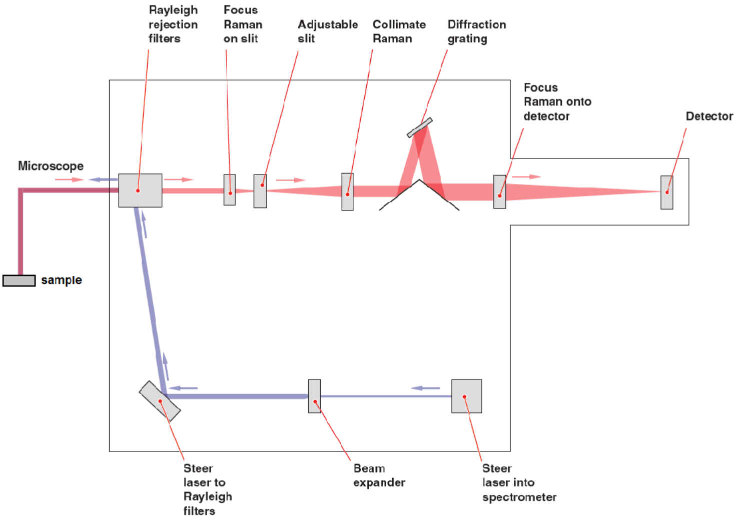

Figure 3.15: Schematic illustration of a Renishaw InVia InVia Raman spectrometer. Reprinted with permission from [89]. Copyright 2011 John Wiley and Sons.

3.2.8 Conclusions

The structural, morphological, chemical, and optical properties of nanomaterials and nanostructures can be achieved by using a combination of techniques such as SEM, TEM, AFM, XRD, XPS, PL, and Raman spectroscopy. The necessary information to successfully fabricate and test a nanostructure/nanomaterial can be extracted by using the aforementioned techniques.

3.3 Materials

Polystyrene spheres (aqueous dispersion, 10 % w/w, size 1 and 0.5 µm), sodium dodecyl sulfate (SDS, CAS: 151-21-3, purity $>$ 99 %), hydrofluoric acid (HF, CAS: 47590, 48 % w/w), hydrogen peroxide (H_2O_2, CAS: 31642, 30 % w/w in H_2O), nitric acid (HNO_3, CAS: 30709, $\geq$65 % w/w), and hydrochloric acid

(HCL, CAS: 258148, 37 % w/w), and 2-Methylimidazole (HmiM, CAS: 693-98-1, > 99 %) were purchased from Sigma-Aldrich. Carboxylate-modified polystyrene spheres (aqueous dispersion, 4 % w/w, size 5 µm) were purchased from Thermo Scientific. $ZnCl_2$ (CAS: 7646-85-7, purity > 98 %) and potassium chloride (KCL, CAS: 7447-40-7, purity > 99 %) were purchased from Fluka. Thiophenol (C_6H_5SH, CAS: 108-98-5, purity > 99 %) and hydrogen tetrachloroaurate (III) trihydrate ($HAuCl_4 \cdot 3\,H_2O$, CAS: 16961-25-4, purity > 99 %) were purchased from Alfa Aesar. Diethylzinc ($(C_2H_5)_2Zn$, DEZ, CAS: 557-20-0, purity > 95 %) was purchased from Strem Chemicals. Boron-doped (8–25 Ω cm) p-type (100) crystal orientation Si wafers were purchased from LG Siltron Inc. Korea. Indium tin oxide (ITO) deposited on quartz was purchased from Präzisions Glas & Optik.

3.4 Experimental details for silicon nanowires covered with ZnO by ALD

3.4.1 Fabrication of silicon nanowires covered by ALD

Fig. 3.16 presents a schematic view of the overall process for the synthesis of SiNWs. A Si wafer was cut into 1 cm × 1 cm pieces and were cleaned sequentially with deionized (DI) water(18.2 MΩ cm), ethanol and acetone by ultrasonication for 15 min in each solvent. Then the substrates were treated by oxygen plasma to have a hydrophilic surface. The floating-transferring technique was used to deposit polystyrene spheres on the Si substrates.

Briefly, 40 µL of polystyrene spheres diluted by an equal amount of ethanol, was applied onto the modified substrates. After holding the substrate stationary for a while to disperse the solution, the wafer was then slowly immersed into the glass vessel filled with DI water, and polystyrene spheres started to form a monolayer on the water surface. After, 5 µL of an SDS solution (10 % w/w) were added to the water interface to change the surface tension and consolidate the particles. As a result, a large monolayer with highly ordered areas was obtained. Then, this monolayer of polystyrene spheres was transferred to the target substrate. The quality of the polystyrene spheres monolayer mask can be assessed right away by looking at the uniformity of the color throughout the whole area.

The reflected color of the pattern varies with the size of the spheres and the quality of the arrangement. After drying the sample in air at room temperature, the spheres were self-assembled into a close-packed, two-dimensional ordered lattice via attractive capillary forces.

After the consolidation of the polystyrene spheres monolayer, the diameter of the polystyrene spheres was decreased by oxygen plasma etching for 5 min to expose a part of the surface of the wafer for metal deposition. In order to stick the polystyrene spheres to the Si surface, a heat treatment at 100 °C for 30 min was performed. Next, a 30 nm Au film was deposited by sputter deposition. The sputtering was carried out at a discharge of 25 mA in a vacuum with a pressure

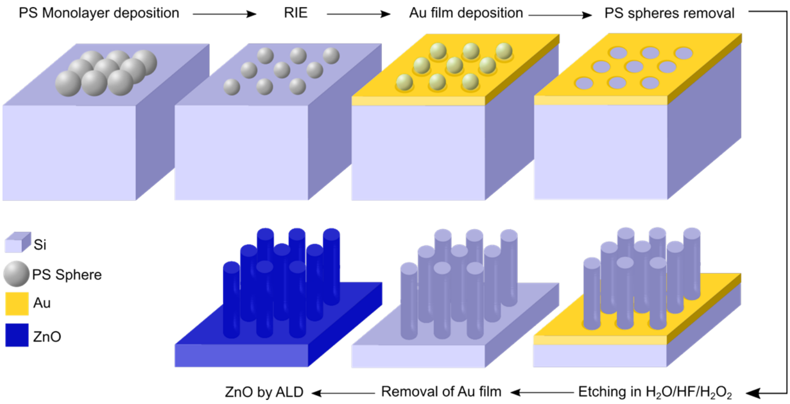

Figure 3.16: Schematic illustration of the different processes involved in MACE. The numbers indicate the steps introduced in this subsection.

below 0.1 mbar. After, the polystyrene spheres were removed by sonicating the samples during 5 s in ethanol. The samples covered by Au were etched with a solution of $H_2O/H_2O_2/HF$ with a volume ratio of 1:0.15:0.3 at room temperature for 1, 2, 5, and 7 min. To remove the residual Au, the samples were dipped in an aqua regia solution (a mixture of HNO_3 and HCl). Finally, 20 nm of ZnO were deposited by ALD at 100 °C with the parameters showed on Table 3.1. Similarly, 100 cycles of Pd were deposited at 220 °C on bare SiNWs with the parameters showed on Table 3.2.

3.4.2 Characterization of ZnO deposited by ALD on silicon nanowires

The XRD patterns were measured in the 2θ angular region between 10° and 60° with a scan speed of $2\,°\,\mathrm{min}^{-1}$ and a step rate of roughly $0.02\,°\,\mathrm{s}^{-1}$. From the XRD patterns, the grain size was calculated using the Debye-Scherer equation. SiNWs covered by ALD of ZnO were also investigated by TEM. The cross-sections and lamellas for TEM investigations were prepared by Focused Ion Beam (FIB). The FIB milling was carried out with a JEOL, JIB-4000.

Raman scattering was measured in backscattering geometry with a spectral resolution of $1\,\mathrm{cm}^{-1}$. The incident light was not polarized, and also the light detector contained no polarization filters. Raman spectroscopy was performed with a 488 nm laser. The beam was focused on the samples with a 50 × microscope objective with a NA = 0.4. The incident optical power was changed by using neutral density filters in the beam path. PL spectroscopy was studied in the spectral range of 350 nm to 800 nm with an excitation wavelength of 280 nm.

To test the capability of ZnO for detecting H_2O_2, a home-made PL setup was used. The PL was studied in the spectra range of 360 nm to 600 nm with an excitation wavelength of 330 nm. The samples were introduced into a black anodized aluminum chamber filled with a solution of 0.01 M phosphate buffered saline (PBS) and varying concentrations of H_2O_2.

3.5 Experimental details for Au-covered hollow urchin-like ZnO structures

3.5.1 Fabrication of Au-covered hollow urchin-like ZnO structures

Fig. 3.17 presents a schematic view of the overall process for the synthesis of Au-covered ZnO urchin-like structures. First, ITO substrates 1 cm × 2 cm were cleaned by sonication for 15 min in acetone, ethanol, and isopropanol sequentially and finally dried under air. After, the PS spheres were deposited on the ITO substrates using a previously reported method with slight modifications [22].

Briefly, a 1:2 solution of polystyrene (PS) spheres and anhydrous ethanol was added dropwise with a micropipette onto the surface of a tilted glass slide (previously treated with oxygen plasma) that was resting on the wall of a Petri dish filled with DI water. Afterward, 5 µL of an SDS solution (10 % w/w) were added to the water surface to change the surface tension and pack together the polystyrene spheres. The self-assembled PS spheres were then transferred to the ITO substrate (previously exposed to a 4 W, 254 nm UV lamp for 15 min to render it hydrophilic) by carefully introducing the substrate into the Petri dish and removing it from the solution at an angle of 45°. Once dry, the substrates were heated in an oven at 100 °C for 30 min to promote the adhesion of the PS spheres to the substrate. Next, the size of the spheres was reduced to produce a non–close-packed arrangement by reactive ion etching in O_2 plasma (0.6 mbar, 50W). The size of the polystyrene spheres was controlled by adjusting the o_2 plasma exposure time. As an example, after being etched for 5 min, the diameter of the PS spheres was reduced to 460 nm, leaving an interparticle distance of 60 nm (Fig. B.1).

Afterward, a 20 nm-thick ZnO layer was deposited on the PS spheres-covered substrates by ALD. The ZnO films were grown at 80 °C with the parameters showed on Table 3.1. Subsequently, electrodeposition of ZnO was performed using a previously reported procedure [40]. A three electrode configuration was used with the ITO/polystyrene spheres/ZnO ensemble as a working electrode, a Pt plate as the counter electrode, and Ag/AgCl as the reference electrode. An aqueous solution of 0.05 mM $ZnCl_2$ (zinc precursor) and 0.1 M KCl (supporting electrolyte) was used as the electrolyte and was continuously bubbled with O_2 during the whole electrodeposition process. The electrodeposition was carried out at 80 °C with a constant electric potential of -1 V during 15 min in a VersaSTAT 3 potentiostat. Once the electrodeposition was completed, the PS spheres were burned off in air at 600 °C for 2 h. Finally, a Au layer (10, 30 and 50 nm) was deposited by E-beam evaporation on top of the substrates.

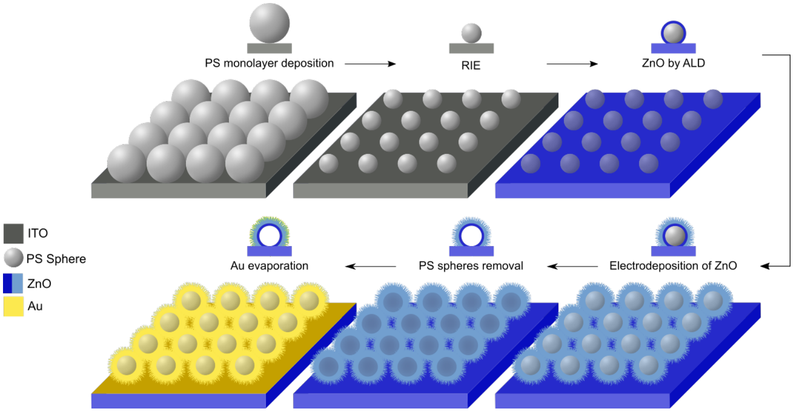

Figure 3.17: Schematic illustration of the different processes involved in the fabrication of Au-covered hollow urchin-like structures.

3.5.2 Characterization of Au-covered hollow urchin-like structures

The morphology of the as-prepared Au-covered urchin-like ZnO samples was characterized by SEM (Fig. 3.18).

In addition, samples were prepared for TEM experiments by performing angular cuts using FIB using a gallium source working at 10 kV, with 60°, 40° and 30° incident angle geometries over a large area (50 µm). In this way, several particles were cut at different axis and geometry. TEM experiments were performed at 200 kV. Samples were sonicated in ethanol after ion milling and drop cast on commercially available Cu grids and vacuum dried overnight in a desiccator. Fig. 3.18 displays TEM and EDX measurements for the Au-covered ZnO urchin-like structures.

The XRD patterns were measured in the 2θ angular region between 20° and 70° with a scan speed of $2\,°\,\mathrm{min}^{-1}$ and a step rate of roughly $0.02\,°\,\mathrm{s}^{-1}$. Fig. 3.18 shows the XRD patterns of ITO, urchin-like ZnO, and Au-covered urchin-like ZnO structures for comparison.

SERS measurements were performed with a Raman microscope with a 785 nm laser and a 100 × objective lens with a NA = 0.9 in a backscattering geometry. The samples were irradiated with laser powers of 0.48 mW (633 nm) and 0.55 mW (785 nm) with acquisition times between 1 s and 10 s. For comparison, all the collected spectra were normalized by laser power and acquisition time. The average SERS intensities reported and relative standard deviations (RSD) were calculated with 25 SERS spectra.

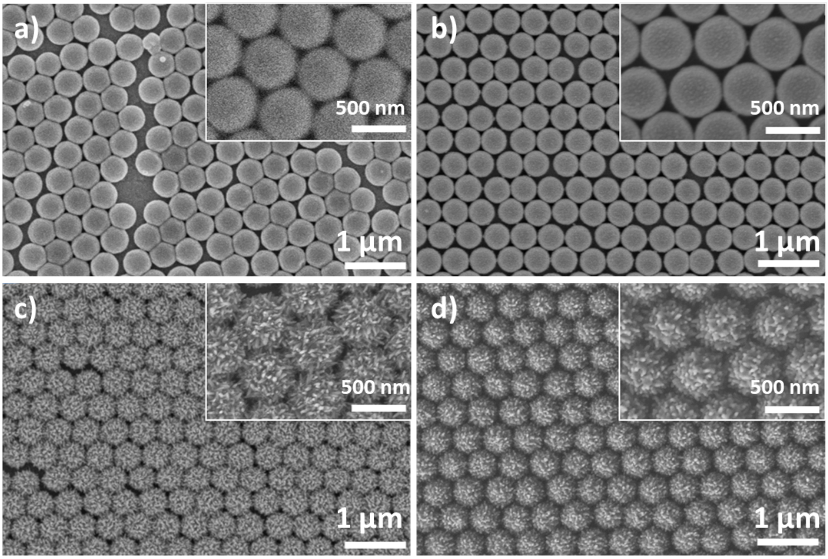

Figure 3.18: SEM micrographs of (a) an array of well-organized PS spheres, (b) PS spheres after been subjected to an oxygen plasma treatment, (c) ordered hollow urchin-like ZnO structures, and (d) urchin-like ZnO structures covered by a 30 nm-thick Au layer deposited by e-gun evaporation. The insets show higher magnifications of the corresponding SEM images.

3.6 Experimental details for hybrid Pd/Au and ZnO/Au/ZIF-8 materials

3.6.1 Fabrication and characterization of silicon nanowires decorated with Pd/Au nanoparticles

Silicon nanowires were prepared following the same procedure shown in Section 3.4.1. For the galvanic replacement reaction, a 15.66 mM solution of $HAuCl_4$ in DI water with a final volume of 2 ml was prepared. The $HAuCl_4$ concentration was chosen according to the Pd loading in our sample. The $HAuCl_4$ solution was poured into a small vial and was heated in a silicon oil bath at 70 °C. The SiNWs/Pd sample was introduced into the previously heated solution and was left to react for 16 h. Finally, the SiNWs/Pd/Au sample was thoroughly washed with DI water and left to dry at ambient temperature.

The morphology and composition of the SiNWs/Pd/Au samples was investigated with SEM and EDX. The composition was also studied by XPS with an excitation source of Al Kα (1486.6 eV). The analyzed surface had a diameter of 500 µm. The BEs of the obtained peaks were calibrated with the C1s peak for −c-c− bonds at 284.8 eV.

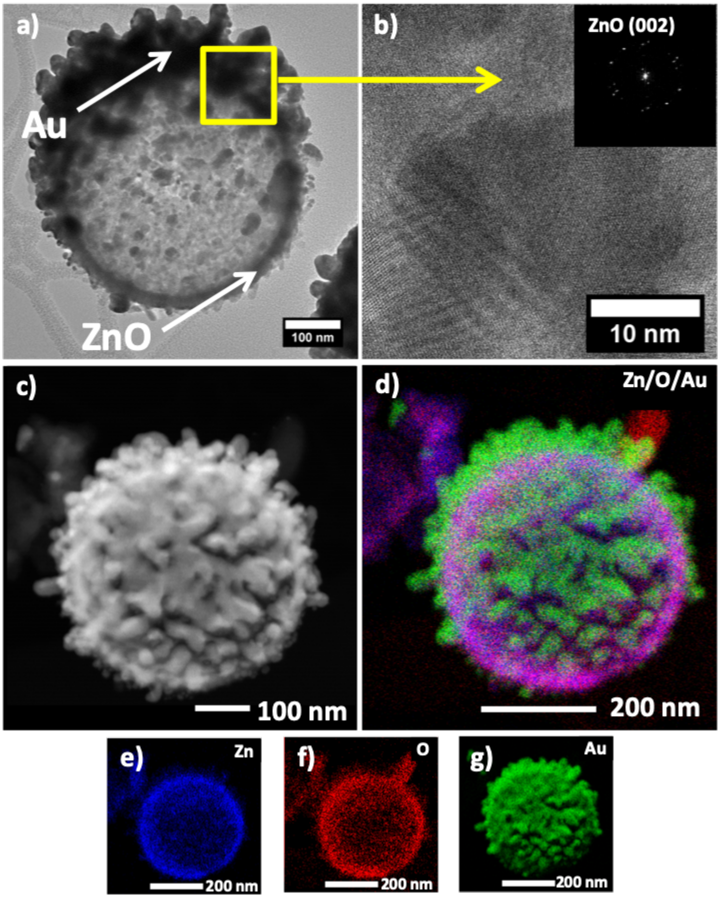

Figure 3.19: a) TEM image of a Au-covered ZnO urchin-like structure and b) high-resolution image of the selected area in image a). The inset in b) shows the FFT operation of the image. c) TEM and (d-g) EDX elemental mapping images of a Au-covered hollow ZnO urchin-like structure. Blue, red, and green illustrate Zn, O, and Au, respectively.

3.6.2 Fabrication and characterization of ZnO/Au/ZIF-8 hollow urchin-like structures

Au decorated hollow ZnO urchin-like structures were prepared following the procedure displayed in Section 3.5.1 with slight modifications. Briefly, 5 µL of an SDS solution (10 % w/w) were added to the surface of a Petri dish filled with DI water. After, a 1:2 solution of 5 µm carboxylate-modified polystyrene spheres and ethanol was added dropwise to the water surface of the Petri dish. After the polystyrene spheres had formed a monolayer, the O_2 plasma treated ITO substrate was carefully introduced into the Petri dish and removed from the

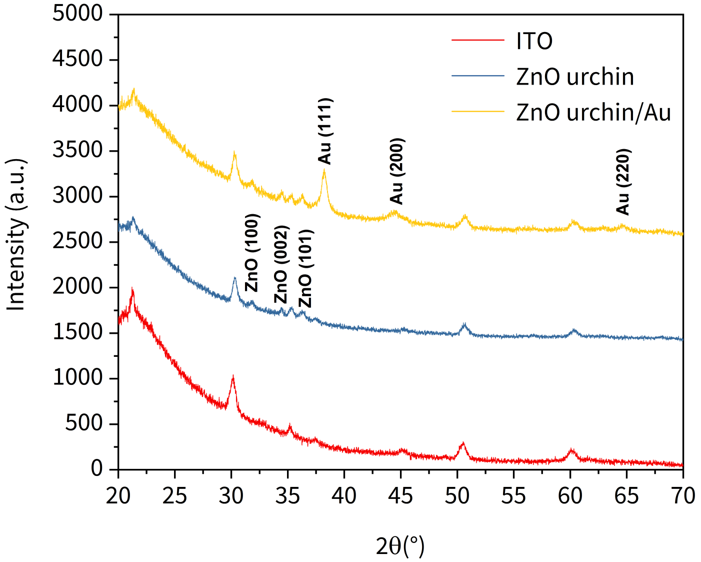

Figure 3.20: XRD patterns of ITO, urchin-like ZnO, and Au-covered urchin-like ZnO structures in the 20° to 70° 2θ

solution at an angle of 45°. For the electrodeposition of ZIF-8, a methanolic solution of $ZnCl_2$ (10 mM) and 2-methylimidazole (HmiM, 30 mM) was saturated with O_2 for 30 min before starting the process. CV deposition ($100\,\mathrm{mV\,s^{-1}}$) with a potential range of -1 V to 0 V was performed during 4 h. After deposition, the samples were washed with copious amounts of methanol and dried at ambient temperature. The sample morphology was characterized with SEM, while the chemical composition was studied with XRD.

3.7 Conclusions

Judging from the various techniques used in combination with ALD, we can say with confidence that it is possible to fabricate nanostructures with precise control of the size, morphology, and composition. For instance, SEM, TEM, and AFM were used to confirm the high aspect ratio of the SiNWs and urchin-like structures. Specifically, by performing SEM after each of the fabrication steps, the quality of the resulting nanostructures could be assessed. In the case of TEM, the crystalline quality of ZnO in both structures could be studied, and a better understanding of the individual features and details could be achieved. Equally important, techniques like XRD, XPS, and Raman are crucial for the correct identification of each of the chemical elements found on the produced nanostructures. As an illustration, XRD was used to evaluate the crystallinity of the ZnO covering the SiNWs. In a similar way, XPS was used to determine the oxidation state of Pd and Au from the Pd/Au decorated SiNWs structures. Equally important, the photoluminescence and Raman spectroscopies were used to test the feasibility of the as-prepared samples to be used as transducers for sensing.

In the next three chapters, the morphological, chemical, and optical characteristics of the prepared nanostructures will be discussed in detail. In the case of SiNWs/ZnO structures, a preliminary application for H_2O_2 sensing will be shown. Similarly, the application of the ZnO/Au urchin-like structures as potential SERS substrates will be demonstrated by detecting two different analytes. Finally, the potential applications of SiNWs decorated with Pd/Au nanoparticles and urchin like ZnO/Au/ZIF-8 structures will be discussed.

References

[1] Sakano, T. et al. "Surface enhanced Raman scattering properties using Au-coated ZnO nanorods grown by two-step, off-axis pulsed laser deposition." *Journal of Physics D: Applied Physics* vol. 41, no. 23 (2008), p. 235304.

[2] Look, D. C. "Recent advances in ZnO materials and devices." *Materials Science and Engineering: B* vol. 80, no. 1-3 (2001), pp. 383–387.

[3] Zhang, X. T. et al. "Temperature dependence of excitonic luminescence from nanocrystalline ZnO films." *Journal of Luminescence* vol. 99, no. 2 (2002), pp. 149–154.

[4] Wang, Q. P. et al. "Photoluminescence of ZnO films prepared by r.f. sputtering on different substrates." *Applied Surface Science* vol. 220, no. 1-4 (2003), pp. 12–18.

[5] Tynell, T. and Karppinen, M. "Atomic layer deposition of ZnO: a review." *Semiconductor Science and Technology* vol. 29, no. 4 (2014), p. 043001.

[6] "Palladium-catalyzed cross-coupling: A historical contextual perspective to the 2010 Nobel prize." *Angewandte Chemie International Edition* vol. 51, no. 21 (2012), pp. 5062–5085.

[7] Adams, B. D. and Chen, A. "The role of palladium in a hydrogen economy." *Materials Today* vol. 14, no. 6 (2011), pp. 282–289.

[8] Weber, M. et al. "High-performance nanowire hydrogen sensors by exploiting the synergistic effect of Pd nanoparticles and metal-organic framework membranes." *ACS Applied Materials & Interfaces* vol. 10, no. 40 (2018), pp. 34765–34773.

[9] "Fabrication of Pd-TiO_2 nanotube photoactive junctions via Atomic Layer Deposition for persistent pesticide pollutants degradation." *Applied Surface Science* vol. 483 (2019), pp. 219–230.

[10] "Substrate-independent palladium atomic layer deposition." *Chemical Vapor Deposition* vol. 9, no. 5 (2003), pp. 258–264.

[11] “Atomic layer deposition of palladium films on Al_2O_3 surfaces.” *Thin Solid Films* vol. 515, no. 4 (2006), pp. 1664–1673.

[12] Weber, M. J. et al. “Atomic layer deposition of high-purity palladium films from Pd(hfac)$_2$ and H_2 and O_2 Plasmas.” *The Journal of Physical Chemistry C* vol. 118, no. 16 (2014), pp. 8702–8711.

[13] Pieranski, P. “Two-dimensional interfacial colloidal crystals.” *Physical Review Letters* vol. 45, no. 7 (1980), pp. 569–572.

[14] Fischer, U. C. and Zingsheim, H. P. “Submicroscopic pattern replication with visible light.” *Journal of Vacuum Science & Technology* vol. 19, no. 4 (1981), pp. 881–885.

[15] Hulteen, J. C. and Van Duyne, R. P. “Nanosphere lithography: A materials general fabrication process for periodic particle array surfaces.” *Journal of Vacuum Science & Technology A: Vacuum, Surfaces, and Films* vol. 13, no. 3 (1995), p. 1553.

[16] Haynes, C. and Duyne, R. V. “Nanosphere lithography: a versatile nanofabrication tool for studies of size-dependent nanoparticle optics.” *The Journal of Physical Chemistry B* (2001), pp. 5599–5611.

[17] Bechelany, M. et al. “Extended domains of organized nanorings of silver grains as surface-enhanced Raman scattering sensors for molecular detection.” *Nanotechnology* vol. 20, no. 45 (2009), p. 455302.

[18] Li, Y. F. et al. “A mediator-free phenol biosensor based on immobilizing tyrosinase to ZnO nanoparticles.” *Analytical Biochemistry* vol. 349, no. 1 (2006), pp. 33–40.

[19] Park, S. G. et al. “Perfectly hydrophobic surfaces with patterned nanoneedles of controllable features.” *Langmuir* vol. 26, no. 8 (2010), pp. 5295–5299.

[20] Fan, H. J. et al. “Well-ordered ZnO nanowire arrays on GaN substrate fabricated via nanosphere lithography.” *Journal of Crystal Growth* vol. 287, no. 1 (2006), pp. 34–38.

[21] Bardosova, M. et al. “Correction: The Langmuir-Blodgett Approach to Making Colloidal Photonic Crystals from Silica Spheres.” *Advanced Materials* vol. 22, no. 45 (2010), pp. 5081–5081.

[22] Vogel, N. et al. “A convenient method to produce close- and non-close-packed monolayers using direct assembly at the air-water interface and subsequent plasma-induced size reduction.” *Macromolecular Chemistry and Physics* vol. 212, no. 16 (2011), pp. 1719–1734.

[23] Zhang, J. et al. “Colloidal Self-Assembly Meets Nanofabrication: From Two-Dimensional Colloidal Crystals to Nanostructure Arrays.” *Advanced Materials* vol. 22, no. 38 (2010), pp. 4249–4269.

[24] Haginoya, C., Ishibashi, M., and Koike, K. “Nanostructure array fabrication with a size-controllable natural lithography.” *Applied Physics Letters* vol. 71, no. 20 (1997), pp. 2934–2936.

[25] Phan, L., Yoon, S., and Moon, M.-W. "Plasma-Based Nanostructuring of Polymers: A Review." *Polymers* vol. 9, no. 12 (2017), p. 417.

[26] Akinoglu, E. M., Morfa, A. J., and Giersig, M. "Nanosphere lithography - Exploiting self-assembly on the nanoscale for sophisticated nanostructure fabrication." *Turkish Journal of Physics* vol. 38, no. 3 (2014), pp. 563–572.

[27] Coburn, J. W. and Winters, H. F. "Plasma etching—A discussion of mechanisms." *Journal of Vacuum Science & Technology* vol. 16, no. 2 (1979), pp. 391–403.

[28] Huang, Z. et al. "Metal-assisted chemical etching of silicon: A review." *Advanced Materials* vol. 23, no. 2 (2011), pp. 285–308.

[29] Li, X. and Bohn, P. W. "Metal-assisted chemical etching in HF/h_2o_2 produces porous silicon." *Applied Physics Letters* vol. 77, no. 16 (2000), pp. 2572–2574.

[30] Kim, Y. et al. "Solvent-induced formation of unidirectionally curved and tilted Si nanowires during metal-assisted chemical etching." *Journal of Materials Chemistry C* vol. 1, no. 2 (2013), pp. 220–224.

[31] Huang, Z., Fang, H., and Zhu, J. "Fabrication of Silicon Nanowire Arrays with Controlled Diameter, Length, and Density." *Advanced Materials* vol. 19, no. 5 (2007), pp. 744–748.

[32] Pal, A., Ghosh, R., and Giri, P. K. "Early stages of growth of Si nanowires by metal assisted chemical etching: A scaling study." *Applied Physics Letters* vol. 107, no. 7 (2015), p. 072104.

[33] Harrison, J. A. and Thompson, J. "The electrodeposition of precious metals; a review of the fundamental electrochemistry." *Electrochimica Acta* vol. 18, no. 11 (1973), pp. 829–834.

[34] Winand, R. "Electrodeposition of metals and alloys-new results and perspectives." *Electrochimica Acta* vol. 39, no. 8-9 (1994), pp. 1091–1105.

[35] Zhang, J. X. and Hoshino, K. "Fundamentals of Nano/Microfabrication and Effect of Scaling." *Molecular Sensors and Nanodevices*. William Andrew Publishing, 2013, pp. 43–101.

[36] Lincot, D. "Electrodeposition of semiconductors." *Thin Solid Films* vol. 487, no. 1-2 (2005), pp. 40–48.

[37] Dharmadasa, I. M. and Haigh, J. "Strengths and Advantages of Electrodeposition as a Semiconductor Growth Technique for Applications in Macroelectronic Devices." *Journal of The Electrochemical Society* vol. 153, no. 1 (2005), G47.

[38] Xu, L. et al. "Morphological Control of ZnO Nanostructures by Electrodeposition." *The Journal of Physical Chemistry B* vol. 109, no. 28 (2005), pp. 13519–13522.

[39] Yoshida, T. et al. "Self-assembly of zinc oxide thin films modified with tetrasulfonated metallophthalocyanines by one-step electrodeposition." *Chemistry of Materials* vol. 11, no. 10 (1999), pp. 2657–2667.

[40] Elias, J. et al. “Hollow urchin-like ZnO thin films by electrochemical deposition.” *Advanced Materials* vol. 22, no. 14 (2010), pp. 1607–1612.

[41] Peulon, S. and Lincot, D. “Cathodic electrodeposition from aqueous solution of dense or open-structured zinc oxide films.” *Advanced Materials* vol. 8, no. 2 (1996), pp. 166–170.

[42] Izaki, M. and Omi, T. “Transparent zinc oxide films prepared by electrochemical reaction.” *Applied Physics Letters* vol. 68, no. 17 (1996), pp. 2439–2440.

[43] Elias, J. et al. “Urchin-inspired zinc oxide as building blocks for nanostructured solar cells.” *Nano Energy* vol. 1, no. 5 (2012), pp. 696–705.

[44] Venna, S. R. et al. “Fabrication of MMMs with improved gas separation properties using externally-functionalized MOF particles.” *Journal of Materials Chemistry A* vol. 3, no. 9 (2015), pp. 5014–5022.

[45] Wu, H. B. and Lou, X. W. “Metal-organic frameworks and their derived materials for electrochemical energy storage and conversion: Promises and challenges.” *Science Advances* vol. 3, no. 12 (2017), eaap9252.

[46] Zhou, T. et al. “Pore size dependent gas-sensing selectivity based on ZnO@ZIF nanorod arrays.” *Sensors and Actuators B: Chemical* vol. 258 (2018), pp. 1099–1106.

[47] Eslava, S. et al. “Metal-organic framework ZIF-8 films as low-κ dielectrics in microelectronics.” *Chemistry of Materials* vol. 25, no. 1 (2013), pp. 27–33.

[48] Ameloot, R. et al. “Patterned Growth of Metal-Organic Framework Coatings by Electrochemical Synthesis.” *Chemistry of Materials* vol. 21, no. 13 (2009), pp. 2580–2582.

[49] Van Assche, T. R. et al. “On controlling the anodic electrochemical film deposition of HKUST-1 metal-organic frameworks.” *Microporous and Mesoporous Materials* vol. 224 (2016), pp. 302–310.

[50] Campagnol, N. et al. “On the electrochemical deposition of metal-organic frameworks.” *Journal of Materials Chemistry A* vol. 4, no. 10 (2016), pp. 3914–3925.

[51] Zhang, Q. et al. “Oxygen-Assisted Cathodic Deposition of Zeolitic Imidazolate Frameworks with Controlled Thickness.” *Angewandte Chemie International Edition* vol. 58, no. 4 (2018), pp. 1123–1128.

[52] Cravillon, J. et al. “Controlling zeolitic imidazolate framework nano and microcrystal formation: Insight into crystal growth by time-resolved in situ static light scattering.” *Chemistry of Materials* vol. 23, no. 8 (2011), pp. 2130–2141.

[53] Toshima, N. and Yonezawa, T. “Bimetallic nanoparticles - Novel materials for chemical and physical applications.” *New Journal of Chemistry* vol. 22, no. 11 (1998), pp. 1179–1201.

[54] Sandoval, A., Louis, C., and Zanella, R. “Improved activity and stability in CO oxidation of bimetallic Au-Cu/TiO_2 catalysts prepared by deposition-precipitation with urea.” *Applied Catalysis B: Environmental* vol. 140-141 (2013), pp. 363–377.

[55] Devarajan, S., Bera, P., and Sampath, S. “Bimetallic nanoparticles: A single step synthesis, stabilization, and characterization of Au-Ag, Au-Pd, and Au-Pt in sol-gel derived silicates.” *Journal of Colloid and Interface Science* vol. 290, no. 1 (2005), pp. 117–129.

[56] Belousov, O. V. et al. “Formation of bimetallic Au-Pd and Au-Pt nanoparticles under hydrothermal conditions and microwave irradiation.” *Langmuir* vol. 27, no. 18 (2011), pp. 11697–11703.

[57] Cobley, C. M. and Xia, Y. “Engineering the properties of metal nanostructures via galvanic replacement reactions.” *Materials Science and Engineering R: Reports* vol. 70, no. 3-6 (2010), pp. 44–62.

[58] Weber, M. J. et al. “Supported Core/Shell Bimetallic Nanoparticles Synthesis by Atomic Layer Deposition.” *Chemistry of Materials* vol. 24, no. 15 (2012), pp. 2973–2977.

[59] Silva, A. G. M. da et al. “Galvanic replacement reaction: recent developments for engineering metal nanostructures towards catalytic applications.” *Chem. Commun.* Vol. 53, no. 53 (2017), pp. 7135–7148.

[60] Nutt, M. O., Hughes, J. B., and Wong, M. S. “Designing Pd-on-Au bimetallic nanoparticle catalysts for trichloroethene hydrodechlorination.” *Environmental Science and Technology* vol. 39, no. 5 (2005), pp. 1346–1353.

[61] Deroco, P. B. et al. “Carbon black supported Au–Pd core-shell nanoparticles within a dihexadecylphosphate film for the development of hydrazine electrochemical sensor.” *Sensors and Actuators B: Chemical* vol. 256 (2018), pp. 535–542.

[62] Sugawa, K. et al. “Refractive index susceptibility of the plasmonic palladium nanoparticle: Potential as the third plasmonic sensing material.” *ACS Nano* vol. 9, no. 2 (2015), pp. 1895–1904.

[63] Lay, B. et al. “Galvanically replaced Au–Pd nanostructures: study of their enhanced elemental mercury sorption capacity over gold.” *Physical Chemistry Chemical Physics* vol. 16, no. 36 (2014), p. 19522.

[64] Mahan, J. E. *Physical Vapor Deposition of Thin Films.* Wiley, 2000, p. 336.

[65] Mattox, D. M. *Handbook of Physical Vapor Deposition (PVD) Processing.* William Andrew, 1998, p. 944.

[66] Harsha, K. *Principles of Physical Vapor Deposition of Thin Films.* Vol. 6. s1. Elsevier, 2005, p. 1155.

[67] Martín-Palma, R. J. and Lakhtakia, A. “Vapor Deposition Techniques.” *Engineered Biomimicry.* Elsevier, 2013, pp. 383–398.

[68] Adachi, H. et al. *Handbook of Sputter Deposition Technology: Fundamentals and Applications for Functional Thin Films, Nanomaterials and MEMS*. Ed. by Wasa, K., Kanno, I., and Kotera, H. Second. Elsevier, 2012, p. 660.

[69] Powell, R. A. and Rossnagel, S. M. "Physics of sputtering." *Thin Films*. Ed. by Powell, R. A. and Rossnagel, S. M. Vol. 26. C. Elsevier, 1999, pp. 23–49.

[70] Behrisch, R. and Wittmaack, K. "Sputtering by Particle Bombardment III." *Topics in Applied Physics*. Ed. by Behrisch, R. and Wittmaack, K. Vol. 64. Topics in Applied Physics. Springer Berlin Heidelberg, 1991, p. 410.

[71] Hornyak, G. L. et al. *Introduction to Nanoscience*. First. CRC Press, 2008, p. 856.

[72] Bastidas, D., Criado, M., and Bastidas, J.-M. "Methods for analysing nanocoatings and ultra-thin films." *Nanocoatings and Ultra-Thin Films*. Woodhead Publishing, 2011, pp. 131–156.

[73] Eaton, P. and West, P. *Atomic Force Microscopy*. Oxford University Press, 2010, pp. 1–58.

[74] Suryanarayana, C. and Norton, M. G. "Practical Aspects of X-Ray Diffraction." *X-Ray Diffraction: a practical approach*. Boston, MA: Springer US, 1998, pp. 63–94.

[75] Moulder, J. F. et al. *Handbook of X-ray photoelectron spectroscopy*. Ed. by Chastain, J. Second. Perkin-Elmer Corporation (Physical electronics), 1992, p. 261.

[76] Tardio, S. and Cumpson, P. J. "Practical estimation of XPS binding energies using widely available quantum chemistry software." *Surface and Interface Analysis* vol. 50 (2018), pp. 5–12.

[77] Perkowitz, S. *Optical Characterization of Semiconductors: infrared, Raman, and photoluminescence spectroscopy*. Ed. by March, N. H. Academic Press, 1993, p. 220.

[78] Rao, M. S. R. and Okada, T. *ZnO Nanocrystals and Allied Materials*. Ed. by Rao, M. S. R. and Okada, T. Vol. 180. Springer Series in Materials Science. New Delhi: Springer India, 2014, p. 374.

[79] Jimenez, J. and Tomm, J. W. "Photoluminescence techniques." *Springer Series in Optical Sciences*. Vol. 202. Springer, Cham, 2016, pp. 143–211.

[80] Smekal, A. "Zur Quantentheorie der Dispersion." *Naturwissenschaften* vol. 43 (1923), p. 873.

[81] Raman, C. V. and Krishnan, K. S. "A New Type of Secondary Radiation." *Nature* vol. 121, no. 3048 (1928), pp. 501–502.

[82] Smith, E. and Dent, G. *Modern Raman Spectroscopy - A Practical Approach*. 2005, pp. 1–210.

[83] Fasolato, C. *Surface Enhanced Raman Spectroscopy for Biophysical Applications*. 2018, p. 155.

[84] Fleischmann, M., Hendra, P. J., and McQuillan, A. J. "Raman spectra of pyridine adsorbed at a silver electrode." *Chemical Physics Letters* vol. 26, no. 2 (1974), pp. 163–166.

[85] Jeanmaire, D. L. and Van Duyne, R. P. "Surface raman spectroelectrochemistry. Part I. Heterocyclic, aromatic, and aliphatic amines adsorbed on the anodized silver electrode." *Journal of Electroanalytical Chemistry* vol. 84, no. 1 (1977), pp. 1–20.

[86] Albrecht, M. G. and Creighton, J. A. "Anomalously intense Raman spectra of pyridine at a silver electrode." *Journal of the American Chemical Society* vol. 99, no. 15 (1977), pp. 5215–5217.

[87] Ru, E. L. and Etchegoin, P. *Principles of Surface-Enhanced Raman Spectroscopy: and related plasmonic effects*. Vol. 17. Elsevier, 2008, p. 688.

[88] Schlückler, S. *Surface Enhanced Raman Spectroscopy: : Analytical, Biophysical and Life Science Applications*. Ed. by Schlücker, S. Vol. 401. Weinheim, Germany: Wiley-VCH Verlag GmbH & Co. KGaA, 2011, p. 354.

[89] Daccache, L., Zeller, S., and Jacob, T. "Capturing irradiation with nanoantennae: Plasmon-induced enhancement of photoelectrolysis." *ChemPhysChem* vol. 18, no. 12 (2017), pp. 1578–1585.

Chapter 4

Si nanowires covered with ZnO by atomic layer deposition for photoluminescence sensing*

Silicon (Si) continues to be the most widely used semiconductor due to its high stability and non-toxicity, quantum confinement effects, high carrier mobility, and well-established nanofabrication techniques [1, 2]. Recently, one dimensional (1D) silicon nanostructures (e.g., SiNWs and Si nanopillars) have received considerable attention thanks to their abilities to scatter and trap incident light, large surface to volume ratio, and other unique electronic and optical properties that make them attractive for a wide range of applications such as electronic devices [3–5], energy storage devices [6, 7], thermoelectrics [8–10], and biosensors [11–14].

The first preparation of Si whiskers with <111> orientation was reported in 1957 by Treuting and Arnold [15]. In 1964, Wagner and Ellis performed an illuminating work and established the vapor-liquid-solid (VLS) mechanism for the growth of Si whiskers [16]. These pioneering studies opened up exciting possibilities for the fabrication and investigation of SiNWs. In 2002, Peng *et al.* introduced an HF-etching-assisted nanoelectrochemical strategy to synthesize wafer-scale aligned SiNWs [17]. To date, SiNWs can be fabricated by different methods such as CVD [18], laser ablation [19], molecular beam epitaxy [20], chemical etching [21], and solution growth [22]. Among these preparation methods, the metal-assisted chemical etching (MACE) of silicon substrates in combination with NSL has emerged as a promising method to fabricate large areas of ordered SiNWs [7, 23]. MACE and NSL techniques have experience an increasing attention, mainly because MACE is an inexpensive and straightforward process that allows controlling various parameters of the etched nanostructures such as shape, height, diameter, and crystallographic orientation [24–26]. The main advantages of NSL are its short preparation time, high level of hexagonal structure orientation, and the possibility of applying it directly onto different types of surfaces [27].

ZnO has attracted intensive research effort for its unique properties such as thermal and chemical stability, optical transparency, and piezoelectricity [28]. The addition of ZnO as shells around SiNWs (as cores) can have substantial and beneficial impact on the stability, as well as on the mechanical, photoelectrochemical, and sensing properties when compared to bare ZnO nanowires fabricated

---

*Parts of this chapter have been published as: O. Graniel, V. Fedorenko, R. Viter, I. Iatsunskyi, G. Nowaczyk, M. Weber, K. Załęski, S. Jurga, V. Smyntyna, P. Miele, A. Ramanavicius, S. Balme, M. Bechelany, Optical properties of ZnO deposited by atomic layer deposition (ALD) on Si nanowires, *Materials Science and Engineering: B*, 236–237 (2018) 139–146. doi:10.1016/j.mseb.2018.11.007.

with other techniques [29–31]. Similarly, Si is an attractive substrate thanks to its excellent thermal conductivity, superior crystalline quality, low cost, and size availability with different types of doping.

ZnO thin films can be prepared using various techniques, but the conformality of the deposit required for its preparation as a shell around NWs requires the use of ALD [32–35]. To date, ALD is one of the most promising deposition methods for growing uniform thin films, especially in the cases where precise film thickness control, high reproducibility, thickness uniformity, and excellent conformity are required [36, 37].

In the present work, SiNWs produced by MACE in combination with NSL followed by an ALD deposition of ZnO are investigated. The structural and optical properties of the obtained nanostructures are evaluated. Finally, the SiNWs/ZnO hybrid structures are tested as possible transducers for H_2O_2 sensing by photoluminescence spectroscopy.

4.1 Results and discussion

The final diameter of the SiNWs depends on the O_2 plasma etching time as seen in Fig. 4.1. The etching of polystyrene spheres from 1 to 10 minutes allows decreasing the polystyrene spheres diameter from (960 ± 10) nm to (610 ± 10) nm. Fig. 4.1a shows a SEM image of PS spheres deposited on a Si wafer, which confirms the possibility to obtain a relatively large area, close-packed, hexagonal polystyrene monolayer, produced by the floating-transferring technique. Fig. 4.1f shows a photograph of a monolayer pattern of polystyrene spheres prepared by the mentioned technique on a $2\,\mathrm{cm} \times 2\,\mathrm{cm}$ silicon wafer. The substrate presents a characteristic color that is caused by the diffraction of light from the polystyrene sphere array. Fig. 4.2 shows the final structure of SiNWs (etching time is 5 min) after depositing 50 nm ZnO film by ALD. The SEM images display the conformal ZnO coating on the SiNWs by ALD.

Fig. 4.3 (a) 2D and (b) three dimensional (3D) images of the SiNWs covered with a 50 nm ZnO layer by ALD. The array of SiNWs exhibit hexagonal packing over a large area of $15\,\mu\mathrm{m} \times 15\,\mu\mathrm{m}$ as previously shown by SEM. Due to the high aspect ratio of the SiNWs, the AFM probe cannot reach the bottom part of the sample and degrades quickly. For this reason, the total length of the SiNWs cannot be seen by AFM and would require the use of exotic FIB milled tips and carbon nanotube/fiber tips [38].

XRD patterns of SiNWs (etched for 7 min) covered with 20 and 50 nm of ZnO by ALD are shown in Fig. 4.4. Three prominent peaks appear at $2\theta =$ 31.78°, 34.35°, 36.25° and 56.69°, which correspond to the (100), (002), (101), and (110) reflections of the hexagonal wurtzite phase of ZnO, respectively. This indicates that both films are polycrystalline, as commonly reported for ZnO films deposited by ALD [34, 39, 40]. A peak with low intensity at $2\theta = 47.46°$ appears for the 50 nm thick sample, which corresponds to the (102) reflection of ZnO.

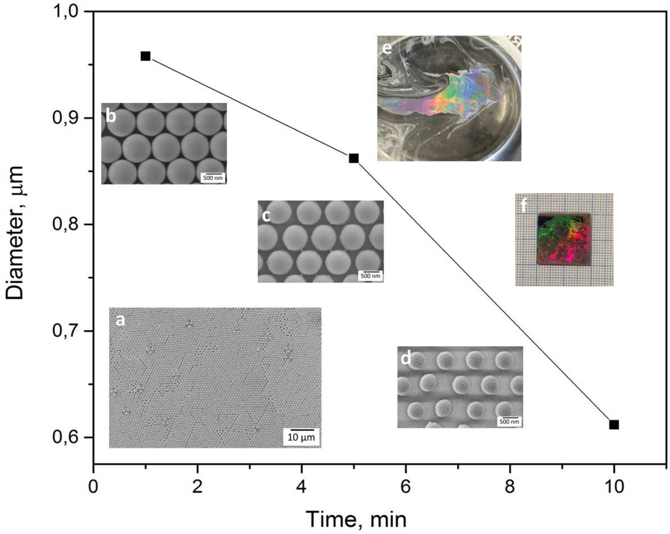

Figure 4.1: Schematic illustration of the RIE process to create a non-close packed monolayer.

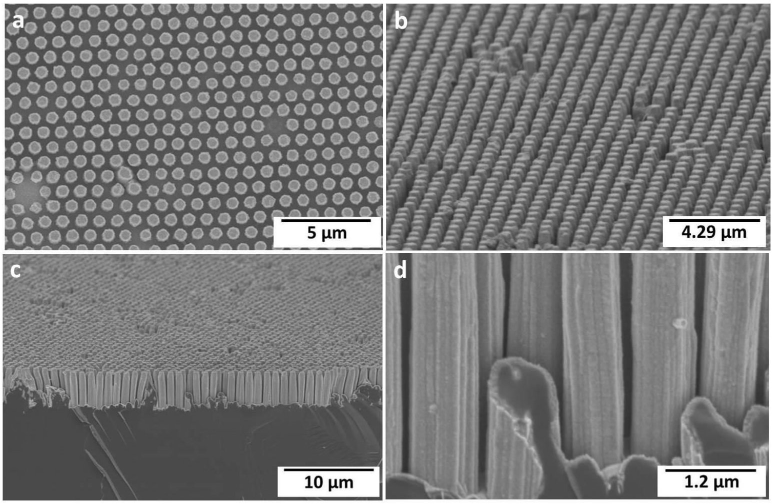

Figure 4.2: SEM images of SiNWs etched for 5 min and covered with a 50 nm ZnO layer deposited by ALD.

The grain sizes D of the deposited films are estimated using the following

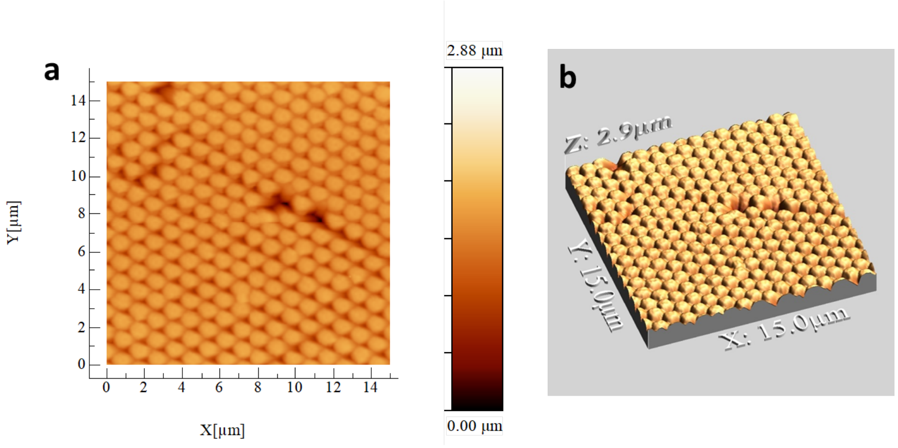

Figure 4.3: a) 2D and b) 3D AFM images SiNWs covered with a 50 nm ZnO layer by ALD.

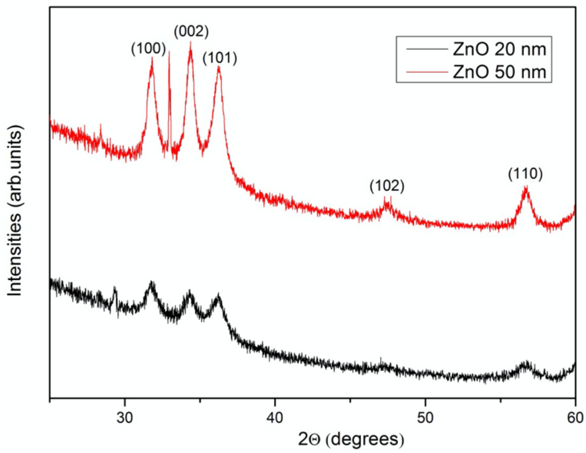

Figure 4.4: XRD patterns of SiNWs (etched for 7 min) covered with 20 and 50 nm of ZnO by ALD.

formula [41]:

$$D = \frac{0.9\lambda}{\beta \cos\theta} \tag{4.1}$$

where λ is the wavelength of X-ray used ($\lambda = 0.154$ nm), β is the full width at half maximum intensity in radians, and θ is the Bragg angle. The average value of grain size is found to be (7.50 ± 0.45) nm, and (14.0 ± 6.5) nm for samples etched for 7 minutes and covered with 20 and 50 nm of ZnO, respectively.

Fig. 4.5 shows the high-resolution TEM images of ZnO/SiNWs with different ZnO layer thicknesses. SiNWs coated with 20 nm of ZnO by ALD are presented in Fig. 4.5a. The TEM images show that the 20 nm ZnO layer covers conformally and homogeneously the SiNWs ZnO. The distance between the nearest wires is reduced from 150 to 300 nm. Also, we noticed that the diameter of the wires is about 450 nm on the top and 850 nm at the bottom. Thus, the wires have the shape of a truncated trapezoid. This shape could be due to the longer exposure time of the top part with the etching solution according to Dawood *et al.* [42]. Macroporous structure of the wires could also be observed (Fig. 4.5a). This can be explained by the lateral transport of the charge carriers [23].

Fig. 4.5b shows a TEM image of silicon nanowires covered by a 50 nm ZnO layer. This layer has a maximum thickness of 55 nm at the top of the SiNWs. For both samples, the ZnO layers have a polycrystalline phase. The size of nanocrystallites was estimated by doing an elliptical shape fit, and the longer axis was used as the nanocrystallite size. The average grain size for the 50 and 20 nm ZnO layers was almost the same (11.8 ± 2.5) nm and (10.0 ± 2.5) nm, respectively), which confirmed the results obtained by XRD. The TEM images demonstrate the ability to produce highly uniform layers of ZnO on SiNWs by using ALD.

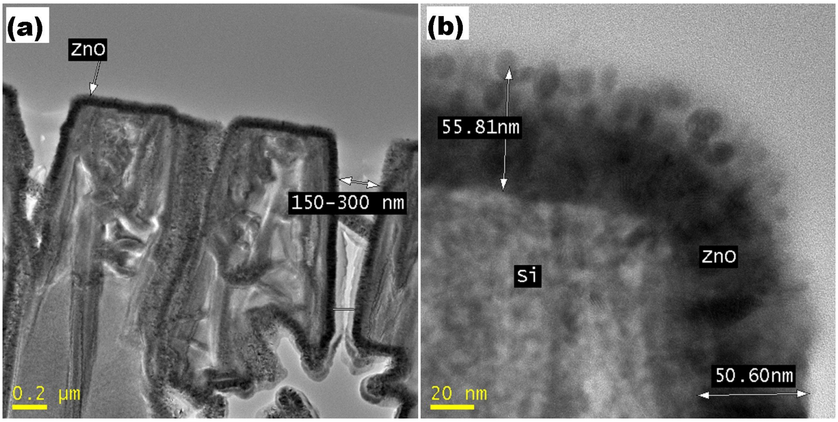

Figure 4.5: Cross-sectional TEM images of SiNWs with (a) 20 and (b) 50 nm of ZnO by ALD.

Raman spectroscopy was used to confirm the composition of SiNWs covered by ALD of ZnO. Fig. 4.6 shows the Raman spectra of Si nanowires (7 min. etching) with 20 and 50 nm of ZnO by ALD. An intense peak (E_2 [high]) of Si is observed at $520\,\mathrm{cm}^{-1}$ due to light penetrating through the thin ZnO films [43]. However, by increasing the number of accumulations, a Raman peak at $(432 \pm 2)\,\mathrm{cm}^{-1}$ (E_2 [high]) that corresponds to the wurtzite phase of ZnO, was observed (inset of Fig. 4.6). This mode is associated with the motion of oxygen atoms [43–46]. The E_2 (high) mode peak (full width at half maximum [FWHM] of ∼20 cm^{-1}) is broader than the one for bulk ZnO (FWHM is less than 10 cm^{-1}) and is shifted to higher frequencies or blue shifts. The broadening of the peak and the blue shift are attributed to phonon confinement effects [47].

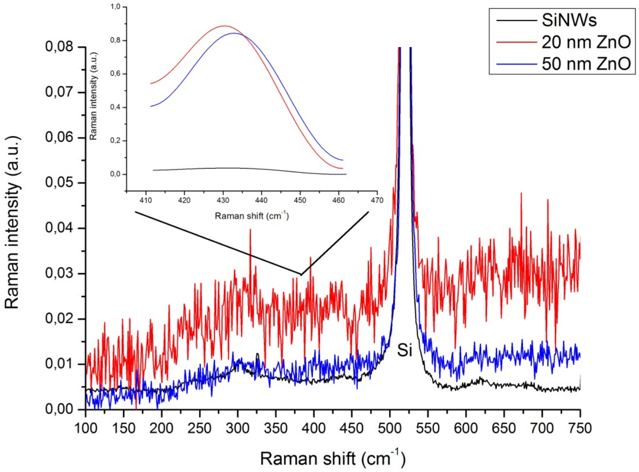

Figure 4.6: Raman spectra of bare SiNWs (etched for 7 min) and after the deposition of ZnO (20 and 50 nm) by ALD.

The PL of SiNWs/ZnO nanostructures with different thicknesses are displayed in Fig. 4.7. The PL spectra showed strong peaks in the range of 410 nm to 450 nm with a long PL tail going to higher wavelengths. Deconvolution of the PL spectra was performed using Gauss fitting in Origin software (see Appendix Fig. A.1). The spectra deconvolution showed peaks centered at 376-379, 411-415, 434-437, 447-480, 490-540, 570-640 nm, and 660-740 nm related to free exciton, Zn interstitials, Zn vacancies, neutral oxygen vacancies, single charged oxygen vacancies, double charged oxygen vacancies, and surface defects, respectively [38,56,68,69] [34, 40, 48, 49]. The domination of defect emission bands points to deviations in the stoichiometry of the prepared 3D ZnO nanostructures. The decrease of PL intensity for ZnO samples deposited on 7 min etched SiNWs could be related to higher light scattering caused by their length. It is suggested that both the high surface area and the anti-reflective properties of the nanostructures might have an impact on the overall PL emission [50].

As a first approach for biosensing, the SiNWs/ZnO structures etched for 5 min and covered with a 50 nm layer of ZnO were tested for the detection of hydrogen peroxide H_2O_2, which is catalytically produced by many oxido-reductase enzymes when acting on a substrate. The samples etched for 5 min and covered with 50 nm of ZnO were selected because they displayed the strongest PL emission that allows improving the overall signal-to-noise ratio. This concept has been reported for the indirect detection of glucose by Sodzel *et al.* by using ZnO

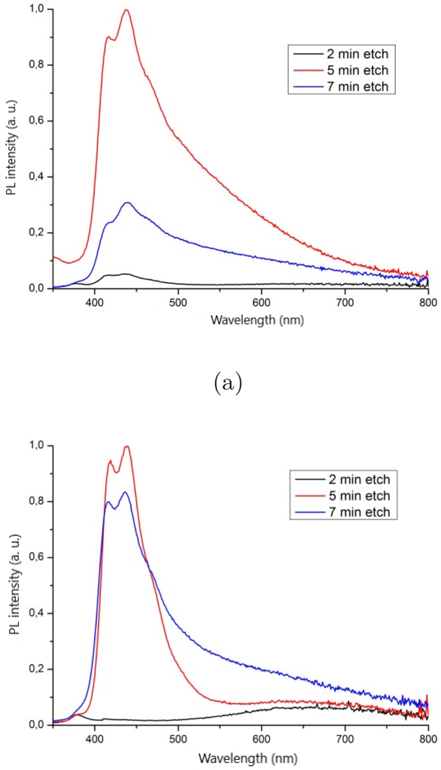

(a)

(b)

Figure 4.7: PL spectra of SiNWs (etched for 2, 5, and 7 min) covered with (a) 20 and (b) 50 nm of ZnO by ALD.

nanoparticles in a 10 mM to 130 mM range [51]. Fig. 4.8 shows the PL spectra of SiNWs/ZnO structures after adding different concentrations of H_2O_2.

The PL intensity decreases in the presence of H_2O_2 and continues to do so as bigger amounts are added into the solution. The nature of this PL quenching can be explained by a collisional mechanism presented schematically in Fig. 4.9. After exciting ZnO, its charge carriers are separated into electrons and holes that go to the conduction and valence bands, respectively.

The radiative recombination of these carriers is followed by the emission of a photon with energy close to the ZnO bandgap (near band edge emission or NBE) or by relaxation through deep level effects (deep level defect emission or DLE) [51]. At the same time, H_2O_2 decomposes catalytically into H_2O and O_2 on the surface of ZnO by acting as an electron acceptor. This acceptance of electrons from the conduction band of ZnO prevents its radiative recombination and quenching of the PL occurs. In addition, several reports show that H_2O_2

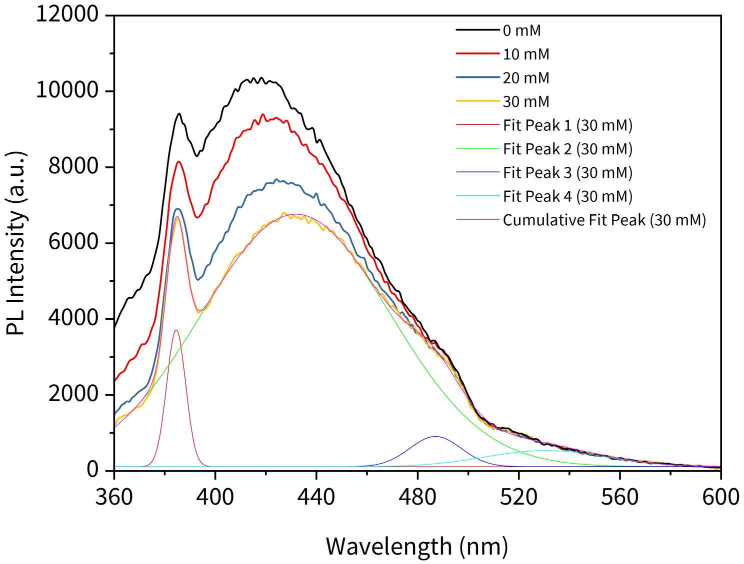

Figure 4.8: Dependence of the PL signal on the H_2O_2 concentration.

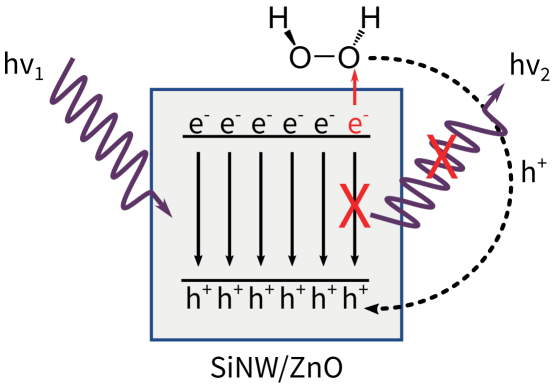

Figure 4.9: Schematic representation of the PL quenching mechanism of ZnO upon exposure to H_2O_2.

can reduce deep level defects by filling O or Zn vacancies to form ZnO, which could account for the quenching of the DLE (but not for the NBE) [52–54].

Besides quenching of the PL emission, we observed a shift of the main DLE peak (∼418 nm as we increased the concentration of H_2O_2. Table 2.1 shows the position of the four main peaks after Gaussian fitting with Origin software (see Appendix Fig. A.2). The violet emission centered at ∼418 nm has been attributed to zinc vacancies [55], interstitial zinc [56], and interface traps [57], which reflects the poor consensus among the different sources in the literature. As we increase the H_2O_2 concentration, a red shift is observed, reaching $\sim$431 nm for the highest H_2O_2 concentration. This blue emission has been attributed to oxygen vacancies at the surface of ZnO [58]. However, as previously mentioned, H_2O_2 can fill O or Zn vacancies or form ZnO, which could decrease the number of oxygen vacancies and would contradict the reports on the origin of the blue emission.

Table 4.1: Position of the four main PL peaks before and after interaction with H_2O_2.

H_2O_2 (mM)	Peak 1	Peak 2	Peak 3	Peak 4
0	384	418	486	529
10	384	420	481	513
20	384	427	485	530
30	384	431	487	530

4.2 Conclusions

In summary, we have demonstrated a simple method for the fabrication of ordered aligned SiNWs/ZnO core shell nanostructures. The method combines colloidal lithography with MACE. The conformal deposition of ZnO on the SiNWs was achieved by using ALD. The ordered SiNWs produced by this method may find many applications in array devices such as field-effect transistors, sensors, electrodes, and two-dimensional photonic crystals. The detailed study of structural and optical properties of the core-shell SiNWs/ZnO heterostructures was presented. The X-ray diffraction analysis revealed that all samples have a hexagonal wurtzite structure. The grain sizes, as measured using XRD data, were found to be in the range of 7 - 14 nm and were confirmed by TEM. The TEM and SEM images demonstrated the ability to produce highly uniform layers of ZnO covered silicon nanowires by the ALD technique. The study of PL spectra of SiNWs/ZnO showed the domination of defect emission bands, which points to deviations in the stoichiometry of the prepared 3D ZnO nanostructures. We also observed the reduction of the PL intensity of SiNWs/ZnO etched for 7 min that could be due to the higher light scattering caused by increasing the length of the nanowires. Finally, we tested the SiNWs/ZnO structures as transducers for the detection of H_2O_2. Quenching of the PL signal was observed, and a mechanism for this effect was proposed. These results open new perspectives for the preparation of optical and sensing devices.

References

[1] Kim, K. “1.1 Silicon technologies and solutions for the data-driven world.” *2015 IEEE International Solid-State Circuits Conference - (ISSCC) Digest of Technical Papers*. Vol. 58. IEEE, 2015, pp. 1–7.

[2] Peng, K.-Q. et al. “Silicon nanowires for advanced energy conversion and storage.” *Nano Today* vol. 8, no. 1 (2013), pp. 75–97.

[3] Cui, Y. et al. “High Performance Silicon Nanowire Field Effect Transistors.” *Nano Letters* vol. 3, no. 2 (2003), pp. 149–152.

[4] Goldberger, J. et al. “Silicon Vertically Integrated Nanowire Field Effect Transistors.” *Nano Letters* vol. 6, no. 5 (2006), pp. 973–977.

[5] Chen, L. J. “Silicon nanowires: the key building block for future electronic devices.” *Journal of Materials Chemistry* vol. 17, no. 44 (2007), p. 4639.

[6] Cui, L.-F. et al. “Crystalline-Amorphous Core-Shell Silicon Nanowires for High Capacity and High Current Battery Electrodes.” *Nano Letters* vol. 9, no. 1 (2009), pp. 491–495.

[7] Pavlenko, M. et al. “Enhancement of optical and mechanical properties of Si nanopillars by ALD TiO_2 coating.” *RSC Advances* vol. 6, no. 99 (2016), pp. 97070–97076.

[8] Hochbaum, A. I. et al. “Enhanced thermoelectric performance of rough silicon nanowires.” *Nature* vol. 451, no. 7175 (2008), pp. 163–167.

[9] Abramson, A. et al. “Fabrication and characterization of a nanowire/polymer-based nanocomposite for a prototype thermoelectric device.” *Journal of Microelectromechanical Systems* vol. 13, no. 3 (2004), pp. 505–513.

[10] Boukai, A. I. et al. “Silicon nanowires as efficient thermoelectric materials.” *Nature* vol. 451, no. 7175 (2008), pp. 168–171.

[11] Cui, Y. et al. “Nanowire nanosensors for highly sensitive and selective detection of biological and chemical species.” *Science* vol. 293, no. 5533 (2001), pp. 1289–1292.

[12] Kim, D. R. and Zheng, X. “Numerical characterization and optimization of the microfluidics for nanowire biosensors.” *Nano Letters* vol. 8, no. 10 (2008), pp. 3233–3237.

[13] Patolsky, F., Zheng, G., and Lieber, C. M. “Nanowire-Based Biosensors.” *Analytical Chemistry* vol. 78, no. 13 (2006), pp. 4260–4269.

[14] Bae, T.-E. et al. “High performance of silicon nanowire-based biosensors using a high- k stacked sensing thin film.” *ACS Applied Materials & Interfaces* vol. 5, no. 11 (2013), pp. 5214–5218.

[15] Treuting, R. and Arnold, S. “Orientation habits of metal whiskers.” *Acta Metallurgica* vol. 5, no. 10 (1957), p. 598.

[16] Wagner, R. S. and Ellis, W. C. “Vapor-liquid-solid mechanism of single crystal growth.” *Applied Physics Letters* vol. 4, no. 5 (1964), pp. 89–90.

[17] Peng, K.-Q. et al. “Synthesis of large-area silicon nanowire arrays via self-assembling nanoelectrochemistry.” *Advanced Materials* vol. 14, no. 16 (2002), p. 1164.

[18] Lerose, D. et al. “Ordered arrays of epitaxial silicon nanowires produced by nanosphere lithography and chemical vapor deposition.” *Journal of Crystal Growth* vol. 312, no. 20 (2010), pp. 2887–2891.

[19] Fukata, N. et al. “Synthesis of silicon nanowires using laser ablation method and their manipulation by electron beam.” *Science and Technology of Advanced Materials* vol. 6, no. 6 (2005), pp. 628–632.

[20] Fuhrmann, B. et al. “Ordered arrays of silicon nanowires produced by nanosphere lithography and molecular beam epitaxy.” *Nano Letters* vol. 5, no. 12 (2005), pp. 2524–2527.

[21] Zhang, Y., Li, W., and Chen, K. “Application of two-dimensional polystyrene arrays in the fabrication of ordered silicon pillars.” *Journal of Alloys and Compounds* vol. 450, no. 1-2 (2008), pp. 512–516.

[22] Park, N.-M. and Choi, C.-J. “Growth of silicon nanowires in aqueous solution under atmospheric pressure.” *Nano Research* vol. 7, no. 6 (2014), pp. 898–902.

[23] Bechelany, M. et al. “New silicon architectures by gold-assisted chemical etching.” *ACS Applied Materials & Interfaces* vol. 3, no. 10 (2011), pp. 3866–3873.

[24] Huang, Z. et al. “Metal-assisted chemical etching of silicon: A review.” *Advanced Materials* vol. 23, no. 2 (2011), pp. 285–308.

[25] Han, H., Huang, Z., and Lee, W. “Metal-assisted chemical etching of silicon and nanotechnology applications.” *Nano Today* vol. 9, no. 3 (2014), pp. 271–304.

[26] Geyer, N. et al. “Influence of the doping level on the porosity of silicon nanowires prepared by metal-assisted chemical etching.” *Nanotechnology* vol. 26, no. 24 (2015), p. 245301.

[27] Rybczynski, J., Ebels, U., and Giersig, M. “Large-scale, 2D arrays of magnetic nanoparticles.” *Colloids and Surfaces A: Physicochemical and Engineering Aspects* vol. 219, no. 1-3 (2003), pp. 1–6.

[28] Özgür, Ü. et al. “A comprehensive review of ZnO materials and devices.” *Journal of Applied Physics* vol. 98, no. 4 (2005), p. 041301.

[29] Li, H.-H. et al. “Coaxial-structured ZnO/silicon nanowires extended-gate field-effect transistor as pH sensor.” *Thin Solid Films* vol. 529 (2013), pp. 173–176.

[30] Memarzadeh Lotfabad, E. et al. “ALD TiO_2 coated silicon nanowires for lithium ion battery anodes with enhanced cycling stability and coulombic efficiency.” *Physical Chemistry Chemical Physics* vol. 15, no. 32 (2013), p. 13646.

[31] Chen, C.-Y. et al. “Enhancing formation rate of highly-oriented silicon nanowire arrays with the assistance of back substrates.” *Scientific Reports* vol. 7, no. 1 (2017), p. 3164.

[32] George, S. M. “Atomic layer deposition: An overview.” *Chemical Reviews* vol. 110, no. 1 (2010), pp. 111–131.

[33] Leskelä, M. and Ritala, M. “Atomic layer deposition (ALD): From precursors to thin film structures.” *Thin Solid Films* vol. 409, no. 1 (2002), pp. 138–146.

[34] Chaaya, A. A. et al. “Evolution of microstructure and related optical properties of ZnO grown by atomic layer deposition.” *Beilstein Journal of Nanotechnology* vol. 4, no. 1 (2013), pp. 690–698.

[35] Marichy, C., Bechelany, M., and Pinna, N. “Atomic layer deposition of nanostructured materials for energy and environmental applications.” *Advanced Materials* vol. 24, no. 8 (2012), pp. 1017–1032.

[36] Graniel, O. et al. “Atomic layer deposition for biosensing applications.” *Biosensors and Bioelectronics* vol. 122 (2018), pp. 147–159.

[37] Iatsunskyi, I. et al. “Study on structural, mechanical, and optical properties of Al_2O_3 –TiO_2 nanolaminates prepared by atomic layer deposition.” *The Journal of Physical Chemistry C* vol. 119, no. 35 (2015), pp. 20591–20599.

[38] Bryce, B. A. et al. “Silicon nanowire atomic force microscopy probes for high aspect ratio geometries.” *Applied Physics Letters* vol. 100, no. 21 (2012), p. 213106.

[39] Viter, R. et al. “Tuning of ZnO 1D nanostructures by atomic layer deposition and electrospinning for optical gas sensor applications.” *Nanotechnology* vol. 26, no. 10 (2015), p. 105501.

[40] Chaaya, A. A. et al. “Tuning optical properties of Al_2O_3/ZnO nanolaminates synthesized by atomic layer deposition.” *The Journal of Physical Chemistry C* vol. 118, no. 7 (2014), pp. 3811–3819.

[41] Robak, E. et al. “The effect of Cu doping on the mechanical and optical properties of zinc oxide nanowires synthesized by hydrothermal route.” *Nanotechnology* vol. 27, no. 17 (2016), p. 175706.

[42] Dawood, M. K. et al. “Interference lithographically defined and catalytically etched, large-area silicon nanocones from nanowires.” *Nanotechnology* vol. 21, no. 20 (2010), p. 205305.

[43] Ye, J. et al. “Raman and photoluminescence of ZnO films deposited on Si (111) using low-pressure metalorganic chemical vapor deposition.” *Journal of Vacuum Science & Technology A: Vacuum, Surfaces, and Films* vol. 21, no. 4 (2003), pp. 979–982.

[44] Pal, B. and Giri, P. K. “Defect mediated magnetic interaction and high T ferromagnetism in Co doped ZnO nanoparticles.” *Journal of Nanoscience and Nanotechnology* vol. 11, no. 10 (2011), pp. 9167–9174.

[45] Mohan Kumar, G. et al. "Magnetic and optical property studies on controlled low-temperature fabricated one-dimensional Cr doped ZnO nanorods." *CrystEngComm* vol. 12, no. 6 (2010), p. 1887.

[46] Kuriakose, S., Satpati, B., and Mohapatra, S. "Enhanced photocatalytic activity of Co doped ZnO nanodisks and nanorods prepared by a facile wet chemical method." *Physical Chemistry Chemical Physics* vol. 16, no. 25 (2014), p. 12741.

[47] Iatsunskyi, I. et al. "Tailoring the structural, optical, and photoluminescence properties of porous silicon/TiO_2 nanostructures." *The Journal of Physical Chemistry C* vol. 119, no. 13 (2015), pp. 7164–7171.

[48] Kurylo, I. et al. "Comparison of Ti-Based Coatings on Silicon Nanowires for Phosphopeptide Enrichment and Their Laser Assisted Desorption/Ionization Mass Spectrometry Detection." *Nanomaterials* vol. 7, no. 9 (2017), p. 272.

[49] Viter, R. et al. "The influence of localized plasmons on the optical properties of Au/ZnO nanostructures." *Journal of Materials Chemistry C* vol. 3, no. 26 (2015), pp. 6815–6821.

[50] Cao, Y. et al. "Fabrication of silicon wafer with ultra low reflectance by chemical etching method." *Applied Surface Science* vol. 257, no. 17 (2011), pp. 7411–7414.

[51] Sodzel, D. et al. "Continuous sensing of hydrogen peroxide and glucose via quenching of the UV and visible luminescence of ZnO nanoparticles." *Microchimica Acta* vol. 182, no. 9-10 (2015), pp. 1819–1826.

[52] Kim, S. H., Kim, H. K., and Seong, T. Y. "Effect of hydrogen peroxide treatment on the characteristics of Pt Schottky contact on n-type ZnO." *Applied Physics Letters* vol. 86, no. 11 (2005), pp. 1–3.

[53] Su, W. Y., Huang, J. S., and Lin, C. F. "Improving the property of ZnO nanorods using hydrogen peroxide solution." *Journal of Crystal Growth* vol. 310, no. 11 (2008), pp. 2806–2809.

[54] Peyghan, A. A. et al. "Hydrogen peroxide reduction in the oxygen vacancies of ZnO nanotubes." *Thin Solid Films* vol. 556 (2014), pp. 566–570.

[55] Wu, X. L. et al. "Photouminescence and cathodoluminescence studies of stoichiometric and oxygen-deficient ZnO films." *Applied Physics Letters* vol. 78, no. 16 (2001), pp. 2285–2287.

[56] Djurišić, A. B. and Leung, Y. H. "Optical properties of ZnO nanostructures." *Small* vol. 2, no. 8-9 (2006), pp. 944–961.

[57] Jin, B. J., Im, S., and Lee, S. Y. "Violet and UV luminescence emitted from ZnO thin films grown on sapphire by pulsed laser deposition." *Thin Solid Films* vol. 366, no. 1-2 (2000), pp. 107–110.

[58] Chen, Z. et al. "Effect of N_2 flow rate on morphology and structure of ZnO nanocrystals synthesized via vapor deposition." *Scripta Materialia* vol. 52, no. 1 (2005), pp. 63–67.

Chapter 5

Au-covered hollow urchin-like ZnO nanostructures for surface-enhanced Raman scattering sensing[*]

Surface-enhanced Raman spectroscopy (SERS) has emerged as one of the most powerful analytical techniques that offer single-molecule detection [1]. Its outstanding sensitivity and non-destructive character have found many applications in many fields such as chemistry [2], medicine [3], biology [4], and environmental sciences [5]. SERS substrates are mainly fabricated with noble metals (Ag, Au, Cu) due to their strong interaction with electromagnetic waves and the excitation of the localized surface plasmon resonance (LSPR) that can be tuned in the ultraviolet-visible-near infrared (UV-Vis-NIR) region [5, 6]. These noble metals are usually combined with nanostructures such as nanospheres [7], nanowires [8], nanogaps [9], nanotrees [10], and nanorods [11] that provide roughened metal surfaces and plasmonically active "hot spots" that enhance the Raman signal by several orders of magnitude [12]. Additionally, thanks to their inherent SERS activity [13], semiconductors have been used to fabricate metal/semiconductor hybrid nanostructures that exhibit both electromagnetic enhancement and charge-transfer effects [14]. Furthermore, these highly-efficient SERS hybrids present additional properties that make them attractive for applications such as photocatalysis [15], water splitting [16], and solar energy conversion [17]. As a semiconductor material with a wide direct bandgap (3.37 eV), biocompatibility [18], and promising optical properties [19], ZnO has been employed for the construction of high-surface-area SERS substrates with a wide range of tunable morphologies [20].

However, the fabrication of reproducible and stable SERS substrates remains a significant challenge [21]. Therefore, much attention has been paid to find facile, repeatable, and high-throughput fabrication methods for large-area nanostructured substrates. Among these methods, NSL has proven to be a reproducible and inexpensive technique that offers well-ordered arrays of nanostructures with wafer-scale throughput [22, 23]. Thus, NSL has been used in combination with other techniques to fabricate different types of SERS substrates such as silver film over nanosphere (AgFON) [24], gold semishells [25], nanoring cavities [26], nanopyramids [27], and optrodes [28]. Recently, high-surface-area urchin-like structures decorated with Ag have been successfully used as SERS substrates [29–31]. Nevertheless, even though Ag is preferred over Au due to its higher

---

[*] Parts of this chapter will be submitted to the *Journal of Materials Chemistry C*

SERS activity, Ag is prone to oxidation in air or water environments [32]. Consequently, decreasing its SERS enhancement factor (EF) as a result of changes in its chemical and plasmonic properties [33]. Herein, we report a high-surface-area reproducible SERS substrate consisting of Au-covered ZnO urchin-like hollow structures for the detection of thiophenol. This substrate was fabricated by using scalable techniques that include NSL, ALD [34], electrodeposition, and electron beam (E-beam) evaporation. NSL was used to obtain a template of well-organized spheres that were later covered with a seed layer of ZnO deposited by ALD. Afterward, ZnO nanowires (NWs) were grown via a hydrothermal method to obtain the urchin-like structures which were finally subjected to E-beam evaporation of Au.

5.1 Results and discussion

Among the different approaches to fabricate ordered arrays of PS spheres, the direct assembly at the air-water interface has been demonstrated to be a simple and low-cost method that offers high-quality monolayers over large areas. Fig. 3.18a shows a SEM micrograph of a large area monolayer of PS spheres with a high degree of order. In order to produce a non-closed-packed monolayer, the PS spheres are exposed to oxygen plasma (Fig. 3.18b). This treatment allows controlling the size of the urchins and space between them. After reducing the size of the PS spheres, a thin 20 nm ZnO layer was deposited by ALD as a seed layer to promote the growth of ZnO NWs (Fig. 3.18b). Owing to its high conformality and homogeneity, the ALD method promotes the uniform generation of ZnO NWs on the surface of the PS spheres, unlike pure hydrothermal methods or sputtering were the thickness control of the seed layer becomes a challenge [35]. In addition, the ALD layer anchors the PS spheres to the ITO substrate and renders their surface electrically conductive for the electrodeposition process. Fig. 3.18c shows the morphology of the urchin-like ZnO structures. Thanks to the homogeneous ALD seed layer, the electrodeposited ZnO NWs are evenly distributed on the surface of the PS spheres. The size and length of the ZnO NWs of the urchin-like structures deposited by electrodeposition can be tuned by changing the electrochemical conditions (i.e., zinc precursor concentration and charge density) [36]. Finally, the urchins are homogeneously covered by a Au film via E-beam evaporation with thicknesses of 10 nm, 30 nm and 50 nm. Fig. 3.18d shows the as-synthesized Au-covered urchin-like structures with a Au layer thickness of 30 nm (10 nm and 50 nm are shown on Fig. B.2).

The morphology and crystallinity of the urchin-like structures were studied by TEM. Fig. 3.19a clearly shows the Au film that covers the top of the urchin-like structures and the 20 nm ZnO seed film deposited by ALD. Notably, the TEM images display a cavity with a reduced contrast and a shell with a uniform dark gray color (Fig. B.3), clearly showing the hollow character of the structures. The high-resolution (HR) TEM image from Fig. 3b shows the lattice fringes that correspond to ZnO and Au. Likewise, the fast Fourier transform (FFT) of the HRTEM image shows the (002) plane of ZnO. Additionally, to further confirm that the PS core of the urchin structures is removed after annealing, an EDX mapping was performed. The EDX elemental mapping (Fig. 3.19d) shows that Zn and O are located in the core of the urchin, while Au is covering the outer shell of the structure.

XRD measurements were carried out to study the cristallinity of the samples. The XRD patterns of ITO, urchin-like ZnO, and Au-covered urchin-like ZnO structures are displayed in Fig. 3.20. The diffraction peaks at 31.8°, 34.4° and 36.4° can be assigned to the hexagonal wurtzite planes of (100), (002), and (101) of ZnO [37, 38], while the peaks at 38.2°, 44.5° and 64.6° can be assigned to the face-centered-cubic (fcc) planes of (111), (200), and (220) of Au [39, 40]. These results show the crystalline nature of the samples and the successful fabrication of a ZnO/Au composite. The remaining peaks correspond to the ITO film deposited on quartz that is used as a substrate [41].

The SERS activity of the substrates was optimized by depositing different thicknesses of Au. Fig. 5.1 shows the Raman spectra of thiophenol molecules grafted on the ZnO urchin-like structures covered with 10 nm, 30 nm and 50 nm of Au deposited by e-gun evaporation. Thiophenol was selected due to its ability to form SAMs via S−Au bonds [42] and its non-resonance behavior near the selected excitation wavelengths (633 nm and 785 nm) [43].

The characteristic vibrational modes of thiophenol molecules (10^{-3} M) are well-observed (see refs [44–46]) like those at 999 cm^{-1} corresponding to the ring out-of-plane deformation and the C−H out-of-plane bending (noted, respectively: r-o-d and γ(CH)), 1022 cm^{-1} corresponding to the C−C symmetric stretching and the ring in-plane deformation (noted, respectively: ν(CC) and r-i-d), 1072 cm^{-1} corresponding to the C−C symmetric stretching and C−S stretching (noted, respectively: ν(CC) and ν(CS)), and at 1572 cm^{-1} the C−C symmetric stretching (noted: ν(CC)). For comparison, we studied the intensity of the peak at 999 cm^{-1}. It is noticeable that the Raman peaks intensities become larger as we increase the Au layer thickness for the two excitation wavelengths. This is in accordance with literature reports where it is shown that the thickness of the metallic layer plays an important role on the overall SERS enhancement [47–49]. For our complete study, we chose the 30 nm-thickness with the excitation wavelength of 785 nm to obtain a good compromise between the SERS signal enhancement and a low overall cost of production of these SERS substrates.

Fig. 5.2a shows the thiophenol spectra obtained from different structures for the purpose of comparison. When ZnO nanowires covered with Au (30 nm) of a size comparable from those on the ZnO urchin-like structures were used, the characteristic Raman peaks of thiophenol could be barely distinguished. Similarly, for the bare Au film (30 nm), the thiophenol peaks could be hardly identified. This result shows that the urchin-like structures present the highest SERS activity from these three types of substrate configurations.

Given the complex 3D morphology of the urchins, it is difficult to know the exact number of molecules that are excited in the SERS measurements [50, 51]. For this reason, the SERS gain (G_{SERS}) for the 30 nm Au-covered ZnO urchins

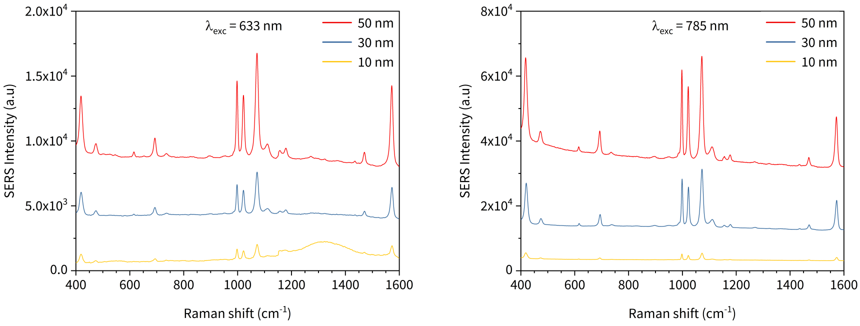

(a) (b)

Figure 5.1: SERS spectra of thiophenol (10^{-3} M) from different Au film thicknesses (10, 30, and 50 nm) for the two excitation wavelengths used in our experiments: (a) 633 nm and (b) 785 nm.

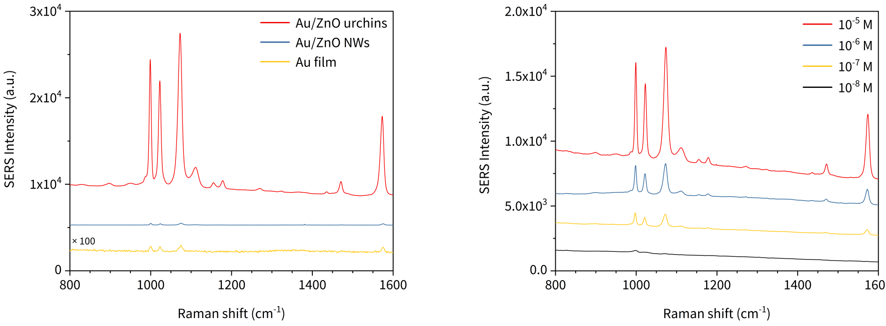

(a) (b)

Figure 5.2: (a) SERS spectra of thiophenol (10^{-3} M) from a 30 nm Au film, a 30 nm Au ZnO NWs, and a 30 nm Au covered urchin-like ZnO, which present an offset to improve the data visualization. (b) SERS spectra of the 30 nm Au-covered ZnO urchins with different thiophenol concentrations. The spectra are not background-corrected and were recorded at the excitation wavelength of 785 nm.

SERS substrates was calculated by using the formula:

$$G_{SERS} \approx \frac{I_{SERS}}{I_{Raman}} \tag{5.1}$$

[9] were I_{Raman} represents the Raman intensity of a planar 30 nm Au thin film functionalized with thiophenol and I_{SERS} represents the Raman intensity of of a thiophenol solution in ethanol (1 M; see Fig. B.4).

Thus, the highest G_{SERS} value for the Raman peak at 1572 cm^{-1} was 5.3×10^3)(Table 5.1).

Table 5.1: Calculated SERS gains G_{SERS} for four Raman peaks (1 mM of thiophenol) at the excitation wavelength of 785 nm for ZnO urchin-like structures covered with a 30 nm Au film.

Raman shift (cm^{-1})	**999**	**1022**	**1072**	**1572**
I_{SERS}	15066	12199	16926	9539
I_{Raman}	79	32	55	18
G_{SERS}	1.9×10^2	3.8×10^2	3.1×10^2	5.3×10^3

This outstanding G_{SERS} can be attributed to the combination of different effects such as efficient light trapping [30] and the generation of hot spots from almost-touching NWs from adjacent urchins [52]. Additionally, the size of the gaps between the Au-covered urchin-like structures is in the same range as the excitation wavelength, which could contribute to the enhancement of localized electromagnetic fields and effective absorption of light by the LSPR [9, 31]. SERS measurements with a range of concentrations from 10^{-5} M to 10^{-8} M were performed in order to assess the limit of detection (LOD) of the substrates . Fig. 5.2b shows the Raman spectra of the substrates grafted with different thiophenol concentrations. The intensities of the Raman peaks remain strong up to a concentration of 1×10^{-7} M and then decrease considerably for the concentration of 10^{-8} M where only the peak at 999 cm^{-1} remains visible. This LOD is comparable with values reported in the literature for thiophenol and similar Au-based structures [45, 48].

To demonstrate the large-area uniformity of the Au-covered hollow urchin-like structures, we constructed a Raman intensity map of the 999 cm^{-1} peak over a 20 µm × 20 µm area with a step size of 1 µm (Fig. 5.3a). The 400 point map shows an almost continuous bright-colored area with a few darker spots where the intensity is lower, which demonstrates the reasonable uniformity of the substrate.

Additionally, the substrate-to-substrate repeatability was investigated by measuring the intensity of the 999 cm^{-1} peak from three different batches. Fig. 5.3b shows the intensity distribution for three different samples. The average RSD value was found to be <10 % which indicates decent repeatability of the SERS substrates and shows their excellent performance.

Finally, to demonstrate the biomolecule sensing capability of these substrates, we chose the biomolecule adenine which can be used in the detection of DNA or RNA analytes [9, 26]. Fig. 5.4 shows Raman spectra of adenine at three different concentrations. The characteristic purine stretch at 736 cm^{-1} is noticeable up to a concentration of 1 µM and the spectra show a low signal-to-noise ratio, which is beneficial for future biosensing applications and is comparable to results published in the literature [9, 26].

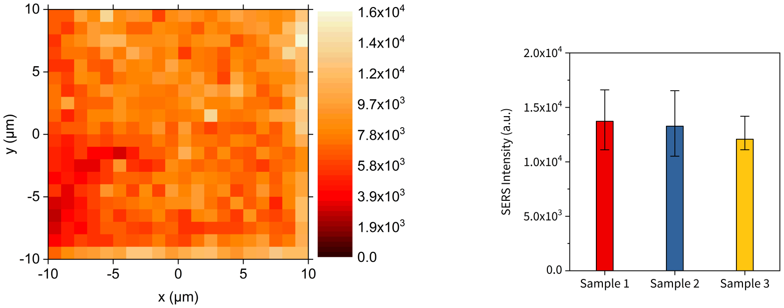

(a) (b)

Figure 5.3: (a) Raman map image of the 999 $\mathrm{cm^{-1}}$ peak from a randomly selected area (20 µm × 20 µm) on the Au-covered hollow urchin-like structures at the 785 nm excitation wavelength. (b) Intensity distribution of the 999 $\mathrm{cm^{-1}}$ peak of three different samples with an average RSD value <10 %.

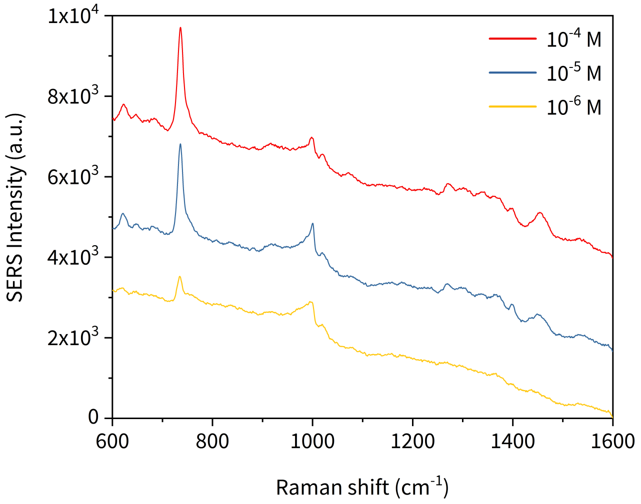

Figure 5.4: SERS detection of adenine with a LOD of 1 µM. An offset was applied to improve the data visualization.

5.2 Conclusions

In summary, high-surface-area Au-covered hollow ZnO urchin-like structures were prepared by combining NSL, ALD, electrodeposition, and E-beam evaporation. These high-throughput methods are readily scalable and allow the precise control of the size of the urchins and the interparticle distance. The amplification of the SERS signal of thiophenol was investigated by depositing different thicknesses of Au and the optimal thickness was selected. The LOD of the optimized substrates was tested by detecting thiophenol down to 10^{-8} M. Additionally, the batch-to-batch repeatability was demonstrated and an average RSD $<10\,\%$ was obtained. Finally, adenine was detected up to a concentration of 10^{-6} M to demonstrate the biosensing capability of our substrate. These results suggest that the Au-covered hollow urchin-like ZnO structures are viable candidates for ultrasensitive and repeatable SERS sensing and biosensing.

References

[1] Kneipp, K. et al. "Single molecule detection using surface-enhanced Raman scattering (SERS)." *Physical Review Letters* vol. 78, no. 9 (1997), pp. 1667–1670.

[2] Xue, J. Q. et al. "Surface-imprinted core-shell Au nanoparticles for selective detection of bisphenol A based on surface-enhanced Raman scattering." *Analytica Chimica Acta* vol. 777 (2013), pp. 57–62.

[3] Lane, L. A., Qian, X., and Nie, S. "SERS nanoparticles in medicine: From label-free detection to spectroscopic tagging." *Chemical Reviews* vol. 115, no. 19 (2015), pp. 10489–10529.

[4] Jarvis, R. M. and Goodacre, R. "Characterisation and identification of bacteria using SERS." *Chemical Society Reviews* vol. 37, no. 5 (2008), p. 931.

[5] Halvorson, R. A. and Vikesland, P. J. *Surface-enhanced Raman spectroscopy (SERS) for environmental analyses*. 2010.

[6] Willets, K. A. and Van Duyne, R. P. "Localized surface plasmon resonance spectroscopy and sensing." *Annual review of physical chemistry* vol. 58, no. October 2006 (2007), pp. 267–97.

[7] Stropp, J. et al. "A new version of AgFON substrates for high-throughput analytical SERS applications." *Journal of Raman Spectroscopy* vol. 34, no. 1 (2003), pp. 26–32.

[8] Li, Y. et al. "A new heterostructured SERS substrate: free-standing silicon nanowires decorated with graphene-encapsulated gold nanoparticles." *Nanoscale* vol. 9, no. 16 (2017), pp. 5263–5272.

[9] Jin, H. M. et al. "Ultralarge area sub-10 nm plasmonic nanogap array by block copolymer self-assembly for reliable high-sensitivity SERS." *ACS Applied Materials & Interfaces* vol. 10, no. 51 (2018), acsami.8b17325.

[10] Cheng, C. et al. "Fabrication and SERS Performance of Silver-Nanoparticle-Decorated Si/ZnO Nanotrees in Ordered Arrays." *ACS Applied Materials & Interfaces* vol. 2, no. 7 (2010), pp. 1824–1828.

[11] Kim, W. et al. “Highly Reproducible Au-Decorated ZnO Nanorod Array on a Graphite Sensor for Classification of Human Aqueous Humors.” *ACS Applied Materials & Interfaces* vol. 9, no. 7 (2017), pp. 5891–5899.

[12] Asiala, S. M. and Schultz, Z. D. “Characterization of hotspots in a highly enhancing SERS substrate.” *The Analyst* vol. 136, no. 21 (2011), p. 4472.

[13] Alessandri, I. and Lombardi, J. R. “Enhanced Raman scattering with dielectrics.” *Chemical Reviews* vol. 116, no. 24 (2016), pp. 14921–14981.

[14] Ren, X. et al. “Au–ZnO hybrid nanoparticles exhibiting strong charge-transfer-induced SERS for recyclable SERS-active substrates.” *Nanoscale* vol. 7, no. 12 (2015), pp. 5147–5151.

[15] Nasr, M. et al. “Recent progress on titanium dioxide nanomaterials for photocatalytic applications.” *ChemSusChem* vol. 11, no. 18 (2018), pp. 3023–3047.

[16] Zhang, X., Liu, Y., and Kang, Z. “3D branched ZnO nanowire arrays decorated with plasmonic Au nanoparticles for high-performance photoelectrochemical water splitting.” *ACS Applied Materials & Interfaces* vol. 6, no. 6 (2014), pp. 4480–4489.

[17] Karam, C. et al. “Urchin-inspired ZnO-TiO_2core-shell as building blocks for dye sensitized solar cells.” *Materials and Design* vol. 126 (2017), pp. 314–321.

[18] Graniel, O. et al. “Atomic layer deposition for biosensing applications.” *Biosensors and Bioelectronics* vol. 122 (2018), pp. 147–159.

[19] Graniel, O. et al. “Optical properties of ZnO deposited by atomic layer deposition (ALD) on Si nanowires.” *Materials Science and Engineering: B* vol. 236-237 (2018), pp. 139–146.

[20] Yang, L. et al. “Fabrication of Semiconductor ZnO Nanostructures for Versatile SERS Application.” *Nanomaterials* vol. 7, no. 12 (2017), p. 398.

[21] Bantz, K. C. et al. “Recent progress in SERS biosensing.” *Physical Chemistry Chemical Physics* vol. 13, no. 24 (2011), p. 11551.

[22] Hulteen, J. C. and Van Duyne, R. P. “Nanosphere lithography: A materials general fabrication process for periodic particle array surfaces.” *Journal of Vacuum Science & Technology A: Vacuum, Surfaces, and Films* vol. 13, no. 3 (1995), p. 1553.

[23] Sakamoto, S. et al. “Ordered hexagonal array of Au nanodots on Si substrate based on colloidal crystal templating.” *Nanotechnology* vol. 19, no. 40 (2008), p. 405304.

[24] Lee, J. et al. “Particle–film plasmons on periodic silver film over nanosphere (AgFON): A hybrid plasmonic nanoarchitecture for surface-enhanced Raman spectroscopy.” *ACS Applied Materials & Interfaces* vol. 8, no. 1 (2016), pp. 634–642.

[25] Li, X. et al. “Ordered Array of Gold Semishells on TiO_2 Spheres: An Ultrasensitive and Recyclable SERS Substrate.” *ACS Applied Materials & Interfaces* vol. 4, no. 4 (2012), pp. 2180–2185.

[26] Im, H. et al. “Self-assembled plasmonic nanoring cavity arrays for SERS and LSPR biosensing.” *Advanced Materials* vol. 25, no. 19 (2013), pp. 2678–2685.

[27] Tabatabaei, M. et al. “Optical properties of silver and gold tetrahedral nanopyramid arrays prepared by nanosphere lithography.” *Journal of Physical Chemistry C* vol. 117, no. 28 (2013), pp. 14778–14786.

[28] Quero, G. et al. “Nanosphere lithography on fiber: towards engineered lab-on-fiber SERS optrodes.” *Sensors* vol. 18, no. 3 (2018), p. 680.

[29] He, X. et al. “Multi-hot spot configuration on urchin-like Ag nanoparticle/ZnO hollow nanosphere arrays for highly sensitive SERS.” *Journal of Materials Chemistry A* vol. 1, no. 47 (2013), pp. 15010–15015.

[30] Tao, Q. et al. “A highly sensitive and recyclable SERS substrate based on Ag-nanoparticle-decorated ZnO nanoflowers in ordered arrays.” *Dalton Transactions* vol. 44, no. 7 (2015), pp. 3447–3453.

[31] Li, R., Han, C., and Chen, Q. W. “A facile synthesis of multifunctional ZnO/Ag sea urchin-like hybrids as highly sensitive substrates for surface-enhanced Raman detection.” *RSC Advances* vol. 3, no. 29 (2013), pp. 11715–11722.

[32] Erol, M. et al. “SERS not to be taken for granted in the presence of oxygen.” *Journal of the American Chemical Society* vol. 131, no. 22 (2009), pp. 7480–7481.

[33] Han, Y. et al. “Effect of oxidation on surface-enhanced Raman scattering activity of silver nanoparticles: A quantitative correlation.” *Analytical Chemistry* vol. 83, no. 15 (2011), pp. 5873–5880.

[34] Weber, M. et al. “Atomic Layer Deposition for Membranes: Basics, Challenges, and Opportunities.” *Chemistry of Materials* vol. 30, no. 21 (2018), pp. 7368–7390.

[35] Sinha, G., Depero, L. E., and Alessandri, I. “Recyclable SERS Substrates Based on Au-Coated ZnO Nanorods.” *ACS Applied Materials & Interfaces* vol. 3, no. 7 (2011), pp. 2557–2563.

[36] Elias, J. et al. “Urchin-inspired zinc oxide as building blocks for nanostructured solar cells.” *Nano Energy* vol. 1, no. 5 (2012), pp. 696–705.

[37] Chaaya, A. A. et al. “Tuning optical properties of Al_2O_3/ZnO nanolaminates synthesized by atomic layer deposition.” *The Journal of Physical Chemistry C* vol. 118, no. 7 (2014), pp. 3811–3819.

[38] Di Mauro, A. et al. “Low temperature atomic layer deposition of ZnO: Applications in photocatalysis.” *Applied Catalysis B: Environmental* vol. 196 (2016), pp. 68–76.

[39] Viter, R. et al. “The influence of localized plasmons on the optical properties of Au/ZnO nanostructures.” *Journal of Materials Chemistry C* vol. 3, no. 26 (2015), pp. 6815–6821.

[40] Arunkumar, S. et al. “Au Decorated ZnO hierarchical architectures: Facile synthesis, tunable morphology and enhanced CO detection at room temperature.” *Sensors and Actuators B: Chemical* vol. 243 (2017), pp. 990–1001.

[41] Ghorannevis, Z., Akbarnejad, E., and Ghoranneviss, M. “Structural and morphological properties of ITO thin films grown by magnetron sputtering.” *Journal of Theoretical and Applied Physics* vol. 9, no. 4 (2015), pp. 285–290.

[42] Lee, B.-S., Lin, D.-Z., and Yen, T.-J. “A low-cost, highly-stable surface enhanced Raman scattering substrate by Si nanowire arrays decorated with Au nanoparticles and Au backplate.” *Scientific Reports* vol. 7, no. 1 (2017), p. 4604.

[43] Li, M. et al. “Microfluidic surface-enhanced Raman scattering sensor with monolithically integrated nanoporous gold disk arrays for rapid and label-free biomolecular detection.” *Journal of Biomedical Optics* vol. 19, no. 11 (2014), p. 111611.

[44] Li, S. et al. “Theoretical and experimental studies on the adsorption behavior of thiophenol on gold nanoparticles.” *Journal of Raman Spectroscopy* vol. 38, no. 11 (2007), pp. 1436–1443.

[45] Scarabelli, L. et al. “Monodisperse gold nanotriangles: size control, large-scale self-assembly, and performance in surface-enhanced Raman scattering.” *ACS Nano* vol. 8, no. 6 (2014), pp. 5833–5842.

[46] Bryche, J. F. et al. “Surface enhanced Raman scattering improvement of gold triangular nanoprisms by a gold reflective underlayer for chemical sensing.” *Sensors and Actuators B: Chemical* vol. 228 (2016), pp. 31–35.

[47] Lee, C. et al. “Thickness of a metallic film, in addition to its roughness, plays a significant role in SERS activity.” *Scientific Reports* vol. 5, no. 1 (2015), p. 11644.

[48] Magno, G., Bélier, B., and Barbillon, G. “Gold thickness impact on the enhancement of SERS detection in low-cost Au/Si nanosensors.” *Journal of Materials Science* vol. 52, no. 23 (2017), pp. 13650–13656.

[49] Schneidewind, H. et al. “The effect of silver thickness on the enhancement of polymer based SERS substrates.” *Nanotechnology* vol. 25, no. 44 (2014), p. 445203.

[50] Le Ru, E. C. et al. “Surface Enhanced Raman Scattering Enhancement Factors: A Comprehensive Study.” *The Journal of Physical Chemistry C* vol. 111, no. 37 (2007), pp. 13794–13803.

[51] Barbillon, G. et al. “Study of Au coated ZnO nanoarrays for surface enhanced Raman scattering chemical sensing.” *Journal of Materials Chemistry C* vol. 5, no. 14 (2017), pp. 3528–3535.

[52] Li, Z. et al. “Galvanic-cell-reaction-driven deposition of large-area Au nanourchin arrays for surface-enhanced Raman scattering.” *Nanomaterials* vol. 8, no. 4 (2018), p. 265.

Chapter 6

Synthesis of hybrid Pd/Au and ZnO/Au/ZIF-8 materials

Nanostructured materials have significantly changed materials science as we know it. Their fabrication methods have provided a new generation of hybrid structures with tunable physical, mechanical, chemical, and optical properties. Nanomaterials have gained attention due to their enhanced performance when compared to their bulk counterparts, making them attractive for many industrial applications. The design of innovative nanostructured materials requires a strict control of their size, shape, and composition. Furthermore, these nanoengineered materials must be cost-effective and compatible with large scale production lines. As one of the few techniques that allows to deposit thin films with control down to the angstrom level, ALD has become an essential tool for the assembly of nanostructured materials. In addition, its compatibility with current manufacturing methods makes it a promising candidate for the high-throughput processing of nanostructured components.

In this chapter, we propose two novel materials based on the SiNWs and urchin-like ZnO structures displayed in Chapter 4 and Chapter 5, respectively. First, to overcome the difficulties of depositing bimetallic Pd and Au nanoparticles directly on the SiNWs, a combination of ALD and galvanic replacement reaction are proposed. Second, a novel electrochemically-based approach to deposit a thin film of ZIF-8 MOF is introduced. Third, the fabrication processes, physical properties, and chemical composition will be discussed. Finally, as these are only preliminary results, general perspectives and examples of how they could be applied for SERS sensing will be suggested.

6.1 Pd/Au nanoparticles

Bimetallic nanostructures have attracted a great deal of attention in the last decade not only for their distinct electronic, optical, and catalytic properties but also for their potential applications in photocatalysis [1], drug delivery [2], water remediation [3], biosensing [4], and energy conversion in low-temperature fuel cells [5]. Unfortunately, for surface-enhanced Raman spectroscopy (SERS) applications, only substrates made from silver (Ag), gold (Au), and copper (Cu) have been used, which limits their range of applications. For this reason, considerable effort has been put for developing SERS-active substrates based on other transition metals. In particular, Palladium (Pd) has been proposed as an alternative SERS-active material due to its stability and catalytical applications in electrochemistry and surface science. Although present, the enhancement factors that can be obtained with Pd (10^1 to 10^3) are much lower than the ones coming from Ag, Au, and Cu (10^6).

Thus, one of the strategies that have been proposed to improve the SERS activity of Pd has been to combine it with SERS-active materials like Ag and Au. This approach takes advantage of the strong electromagnetic field created by the Ag or Au SERS-active substrate when excited with the right excitation line. For instance, Hu *et al.* prepared core-shell Au@Pd structures by chemical deposition of Pd on Au seeds with different sizes [6]. The Au@Pd nanoparticles were deposited on a glassy carbon electrode for in-situ electrochemical SERS measurements of carbon monoxide (CO) to confirm that the Pd shell on the Au core was uniform. Furthermore, the Au@Pd nanoparticles displayed a higher SERS enhancement of more than two orders of magnitude when compared with bare roughened Pd electrodes. Similarly, Zhang *et al.* developed a seed-mediated growth method to produce highly branched concave Au/Pd nanocrystals with five-fold symmetric features [7]. Owing to their sharp multitips and edges, the Au/Pd nanostructures exhibited efficient SERS-activity and superior electrocatalytic activity. Crystal violet dye was detected at concentrations as low as 10^{-12} M.

6.1.1 Results and discussion for silicon nanowires decorated with Pd/Au nanoparticles

Fig. 6.1 shows the SEM images of SiNWs decorated with Pd and Pd/Au nanostructures by combining ALD and galvanic replacement. After optimization of the deposition process, it was found that 100 ALD cycles produced an homogeneous coating of highly dispersed Pd nanoparticles on the surface of SiNWs (Fig. 6.1a,b). Next, Au was introduced in the Pd nanoparticles by performing a galvanic replacement reaction. Fig. 6.1d shows a top view image of the SiNWs decorated with Pd/Au nanostructures and confirms the preservation of the SiNWs architecture.

Additionally, EDX was performed to confirm the presence of Pd and Au on the SiNWs as shown in Fig. 6.2. Considering that the depth of penetration of the EDX measurement is ∼500 nm, the majority of the signal comes from the SiNWs (Si, O) and only a small portion is due to the Pd/Au nanoparticles. [8].

The Pd/Au decorated SiNWs were further analyzed by XPS to determine the oxidation states of Pd and Au. The two peaks with binding energies of 84.5 eV and 88.2 eV correspond to the Au $4f_{7/2}$ and Au $4f_{5/2}$, respectively, which indicate that Au is in its metallic form (Au^0) [9]. Furthermore, the 3.7 eV binding energy difference of the Au $4f_{7/2}$ and the Au $4f_{5/2}$ components is attributed to the Au 4f ionization process, which is in agreement with the values found in the literature [10, 11]. Likewise, the presence of metallic Pd can be confirmed by looking at the Pd $3d_{5/2}$ and Pd $3d_{3/2}$ at binding energies of 335.4 eV and 340.5 eV, respectively [12]. Also, no Au^{3+} or chlorine signals were detected in their corresponding photoelectron region, which tells us that the washing procedure was effective for the removal of Au^{3+} salt residues.

To have an insight into the distribution of Au and Pd species on the SiNWs TEM and EDX-element mapping should be performed. Moreover, different $Au_3{}^+$ concentrations and galvanic replacement reaction times should be tested in order

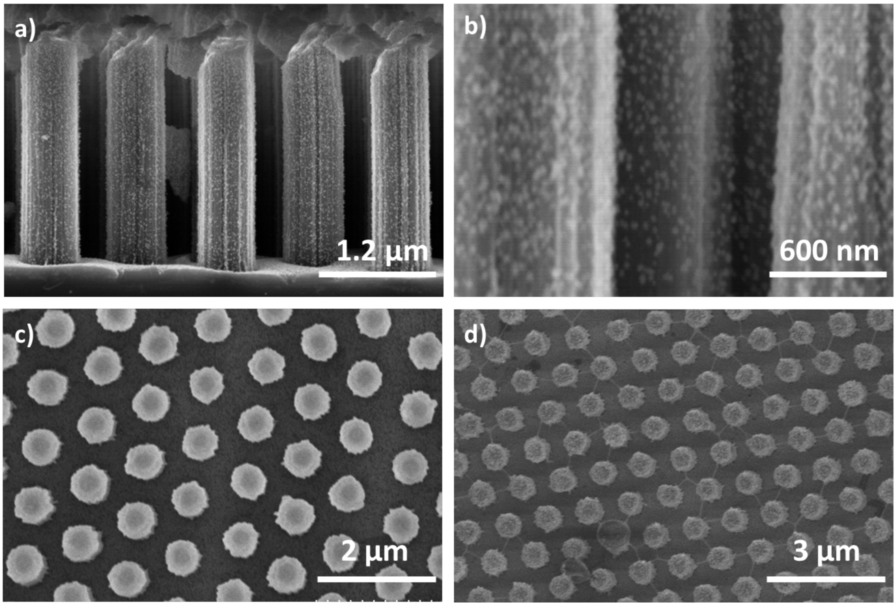

Figure 6.1: SEM images of (a), (b), (c) SiNWs decorated with Pd by ALD. Top view of (d) SiNWs decorated with Pd and Au structures after galvanic replacement.

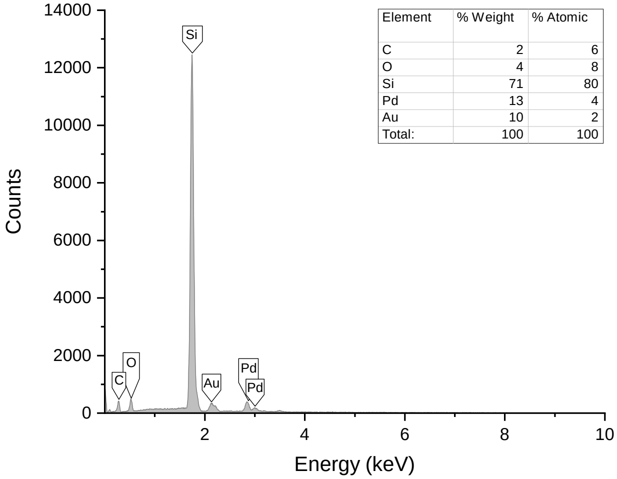

Element	% Weight	% Atomic
C	2	6
O	4	8
Si	71	80
Pd	13	4
Au	10	2
Total:	100	100

Figure 6.2: EDX spectrum of the as-synthesized SiNWs/Pd/Au structures.

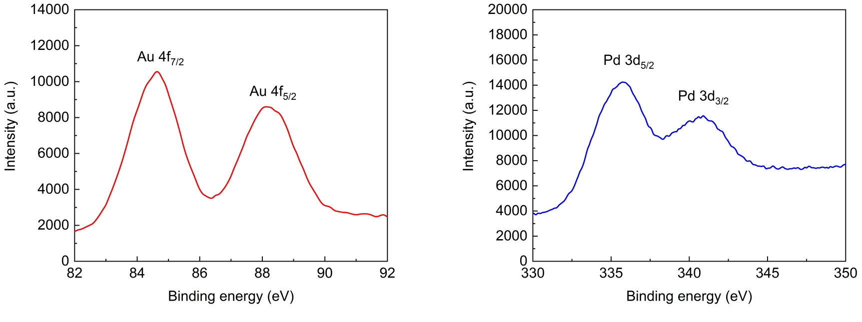

(a) (b)

Figure 6.3: XPS spectra of the Pd/Au system showing (a) Au 4f and (b) Pd 3d core level spectra.

to control the Au:Pd ratio. Finally, Raman measurements should be conducted to test the SERS activity of the substrates. In the next section, a hybrid 3D nanostructure based on ZIF-8 and ZnO will be discussed.

6.2 ZIF-8

Metal organic frameworks (MOFs) constitute a novel class of crystalline materials that are formed through the self-assembly of metal cations (nodes) and organic ligands (linkers). Their diverse structural topologies, unprecedented porosity, and versatile chemical functionalities (host-guest interactions) have made them attractive for applications such as gas storage and separation [13], fabrication of luminescent materials [14], drug delivery [15], and catalysis [16]. The size and aperture of the pores can be fine-tuned by carefully selecting the appropriate metal ion clusters and organic linker sizes and shapes, controlling the catenation (i.e., interpenetration or interweaving of identical frameworks), and taking into account the directional mobility of the linkers.

Recently, the potential of MOFs to improve the detection capabilities of SERS substrates has been explored. For instance, He *et al.* developed a facile one-pot method to prepare AU@MOF-5 nanoparticles wherein a single Au nanoparticle is coated with a uniform MOF-5 shell [17]. The core-shell Au@MOF-5 nanoparticles with a shell thickness of ∼3 nm were highly selective towards CO_2 in a gas mixture of N_2, O_2, and CO. For comparison purposes, bare Au nanoparticles and MOF-5 spheres where exposed to CO_2 and no Raman signals were observed, which demonstrated the critical role of the combination of Au and MOF-5 in the specific core-shell nanostructure. Impressively enough, the influence of aggregation of the nanoparticles towards the repeatability of the measurements can be seen as a drawback. Recently, Kreno *et al.* deposited a thin film of ZIF-8 to detect a series of volatile organic compounds (VOCs) that do not absorb on the surface of Ag "films-over-nanospheres" (FON) substrates [18]. However, the adsorbed molecules were much larger than the 3.4 Å pore apertures, suggesting that the adsorption was preferably at grain boundaries in the film and thus no molecular sieving effect could be envisioned.

6.2.1 Results and discussion for ZIF-8 deposited on urchin-like ZnO structures

SEM images of the bare ZnO/Au and ZnO/Au/ZIF-8 urchin-like structures are shown in Fig. 6.4. As shown in Fig. 6.4, the ZIF-8 film covers the entire urchin structure with small crystallites. This polycrystalline morphology is similar as to the structure seen on a flat ITO substrate [19]. As shown on the XRD pattern from Fig. 6.5, the ZIF-8 film on top of the ZnO/Au structures shows peaks that coincide with the reflections of the simulated pattern, confirming that the single phase is ZIF-8 [20]. Additionally, EDX was performed to further confirm the presence of ZIF-8 on the ZnO/Au urchin-like structures by detecting C and N (Fig. 6.6).

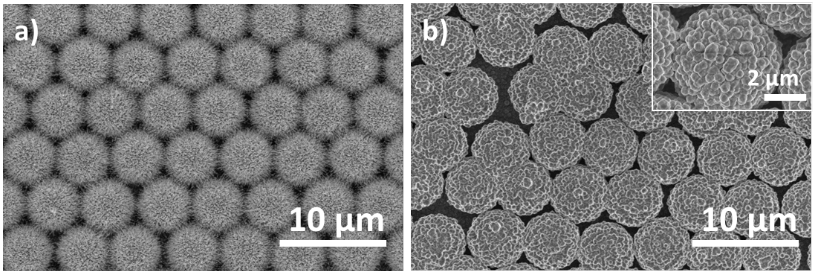

Figure 6.4: SEM images of urchin-like ZnO/Au structures (a) before and (b) after ZIF-8 electrodeposition. The inset in (b) shows a magnification of the ZIF-8 crystals.

So far, the presence of ZIF-8 was confirmed by XRD and EDX measurements. A further analysis with TEM should be conducted to have an insight into the distribution of ZIF-8 on the Au/ZnO urchin-like structures. Also, considering that the electromagnetic enhancement suffers an exponential attenuation with distance [21] (within just a few nanometers), different thicknesses of ZIF-8 should be produced to test the influence on the overall SERS enhancement factor.

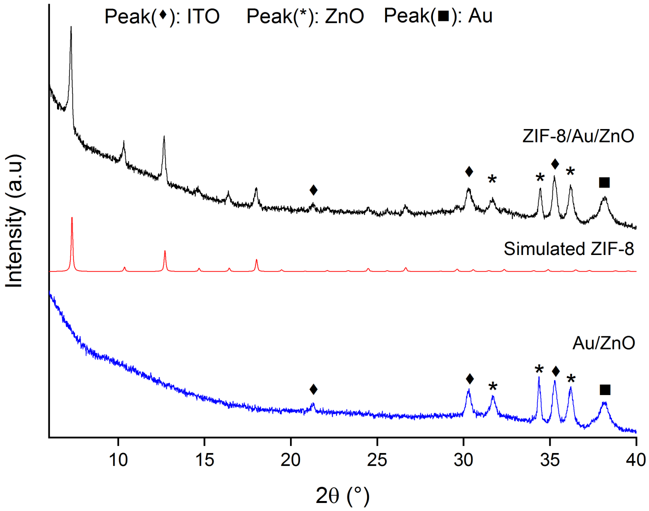

Figure 6.5: XRD patterns of the urchin-like ZnO/Au structures and the urchin-like ZnO/Au/ZIF-8 structures. The simulated XRD pattern of ZIF-8 is given under the corresponding measured pattern. The peaks of ITO come from the underlying substrate.

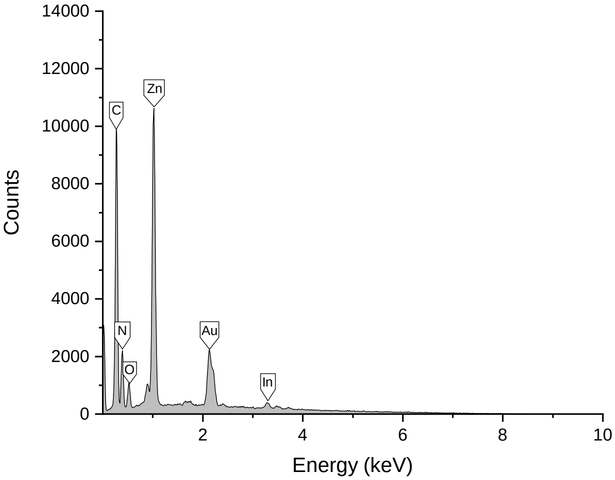

Figure 6.6: EDX spectrum of the as-synthesized ZIF-8/Au/ZnO urchin-like hybrid structures.

6.3 Conclusions

Pd/Au nanoparticles supported on SiNWs were synthesized by a combination of ALD and the galvanic replacement reaction. Their general morphology before and after the galvanic replacement reaction was studied. The composition and chemical state of the Pd/Au nanoparticles was confirmed with EDX and XPS. Further characterization techniques like HRTEM would be of great interest to elucidate the exact morphology and crystallinity of the nanoparticles, which could give us an insight into the replacement mechanism and segregation of Au into the Pd nanoparticles. We believe that these bimetallic nanoparticles could be used as SERS substrates for sensing of relevant biomolecules [6, 7, 22].

ZnO/Au/ZIF-8 hollow urchin-like structures were synthesized by an oxygen-assisted cathodic electrodeposition strategy. The overall morphology was studied by SEM and the chemical composition was confirmed by XRD. The microstructures should be further analyzed with TEM and EDX to study the ZIF-8 film thickness and to confirm the ZnO/Au/ZIF-8 core-shell structure. These hybrid structures could be used as potential SERS substrates for the sensing of volatile organic compounds [17, 18, 23].

References

[1] Wali, L. A. et al. “Excellent fabrication of Pd-Ag NPs/PSi photocatalyst based on bimetallic nanoparticles for improving methylene blue photocatalytic degradation.” *Optik* vol. 179 (2019), pp. 708–717.

[2] McNamara, K. and Tofail, S. A. M. “Nanosystems: the use of nanoalloys, metallic, bimetallic, and magnetic nanoparticles in biomedical applications.” *Physical Chemistry Chemical Physics* vol. 17, no. 42 (2015), pp. 27981–27995.

[3] Thatai, S. et al. “Nanoparticles and core–shell nanocomposite based new generation water remediation materials and analytical techniques: A review.” *Microchemical Journal* vol. 116 (2014), pp. 62–76.

[4] Rick, J., Tsai, M.-C., and Hwang, B. “Biosensors Incorporating Bimetallic Nanoparticles.” *Nanomaterials* vol. 6, no. 1 (2015), p. 5.

[5] Long, N. V. et al. “The development of mixture, alloy, and core-shell nanocatalysts with nanomaterial supports for energy conversion in low-temperature fuel cells.” *Nano Energy* vol. 2, no. 5 (2013), pp. 636–676.

[6] Hu, J. W. et al. “Palladium-coated gold nanoparticles with a controlled shell thickness used as surface-enhanced raman scattering substrate.” *Journal of Physical Chemistry C* vol. 111, no. 3 (2007), pp. 1105–1112.

[7] Zhang, L. F., Zhong, S. L., and Xu, A. W. “Highly branched concave Au/Pd bimetallic nanocrystals with superior electrocatalytic activity and highly efficient SERS enhancement.” *Angewandte Chemie - International Edition* vol. 52, no. 2 (2013), pp. 645–649.

[8] Boyadjiev, S. I. et al. “Preparation and characterization of ALD deposited ZnO thin films studied for gas sensors.” *Applied Surface Science* vol. 387 (2016), pp. 1230–1235.

[9] Lay, B. et al. “Galvanically replaced Au–Pd nanostructures: study of their enhanced elemental mercury sorption capacity over gold.” *Physical Chemistry Chemical Physics* vol. 16, no. 36 (2014), p. 19522.

[10] Venezia, A. M. et al. “Relationship between structure and CO oxidation activity of ceria-supported gold catalysts.” *Journal of Physical Chemistry B* vol. 109 (2005).

[11] Lallo, J. et al. “Oxidation of palladium on Au(111) and ZnO(001) supports.” *The Journal of Chemical Physics* vol. 141 (2014), p. 154702.

[12] Weber, M. et al. “High-performance nanowire hydrogen sensors by exploiting the synergistic effect of Pd nanoparticles and metal-organic framework membranes.” *ACS Applied Materials & Interfaces* vol. 10, no. 40 (2018), pp. 34765–34773.

[13] Wales, D. J. et al. “Gas sensing using porous materials for automotive applications.” *Chemical Society Reviews* vol. 44, no. 13 (2015), pp. 4290–4321.

[14] Zhang, Y. et al. “Luminescent sensors based on metal-organic frameworks.” *Coordination Chemistry Reviews* vol. 354 (2018), pp. 28–45.

[15] Shekhah, O. et al. *MOF thin films: Existing and future applications.* 2011.

[16] Li, B. et al. “Emerging Multifunctional Metal-Organic Framework Materials.” *Advanced Materials* vol. 28, no. 40 (2016), pp. 8819–8860.

[17] Liu, Y. et al. “Core-shell noble-metal@metal-organic-framework nanoparticles with highly selective sensing property.” *Angewandte Chemie - International Edition* vol. 52, no. 13 (2013), pp. 3741–3745.

[18] Kreno, L. E. et al. “SERS of molecules that do not adsorb on Ag surfaces: A metal-organic framework-based functionalization strategy.” *Analyst* vol. 139, no. 16 (2014), pp. 4073–4080.

[19] Zhang, Q. et al. “Oxygen-Assisted Cathodic Deposition of Zeolitic Imidazolate Frameworks with Controlled Thickness.” *Angewandte Chemie International Edition* vol. 58, no. 4 (2018), pp. 1123–1128.

[20] Zhou, T. et al. “Pore size dependent gas-sensing selectivity based on ZnO@ZIF nanorod arrays.” *Sensors and Actuators B: Chemical* vol. 258 (2018), pp. 1099–1106.

[21] Yu, X. et al. “Enhanced thermal stability of boron nitride-coated Au nanoparticles for surface enhanced Raman spectroscopy.” *Journal of Alloys and Compounds* vol. 730 (2018), pp. 487–492.

[22] Fang, P. P. et al. “Optimization of SERS activities of gold nanoparticles and gold-core-palladium-shell nanoparticles by controlling size and shell thickness.” *Journal of Raman Spectroscopy* vol. 39, no. 11 (2008), pp. 1679–1687.

[23] Zhou, X. et al. “Porous zeolite imidazole framework-wrapped urchin-like Au-Ag nanocrystals for SERS detection of trace hexachlorocyclohexane pesticides via efficient enrichment.” *Journal of Hazardous Materials* vol. 368 (2019), pp. 429–435.

Chapter 7

Summary and outlook

The primary motivation of the different projects presented in this thesis was to develop different nanostructured transducers by using ALD in combination with other fabrication techniques. This motivation was addressed by developing two distinct approaches. The first one was based on the combination of ALD and lithographic etching processes to produce high aspect ratio structures that could be used as optical transducers. The second approach involved the elaboration of complex architectures based on ZnO by combining ALD and electrodeposition to introduce structural features that can benefit future biosensing applications. In the following, a summary of the specific achievements is given:

- SiNWs/ZnO were produced with a simple method that combines MACE, NSL, and ALD. The versatility of the method to change the spacing between the SiNWs and their height is demonstrated by modifying the RIE treatment and etching times. The ability of ALD to conformally coat these 3D SiNWs nanostructures with ZnO was confirmed by TEM. Also, XRD and Raman spectroscopy were employed to determine the crystallite size of ZnO and the implications on its optical properties. Photoluminescence measurements of the structures with different etching times and ZnO thicknesses were performed and it was found that the nanostructures obtained with a 5 min etch showed the strongest PL emission. Finally, the 5 min etched SiNWs/ZnO were exposed to varying concentrations of H_2O_2 while recording their PL emission spectra as a first approach for sensing. Quenching of the PL emission was observed with the first addition of H_2O_2, and a mechanism for this observation was proposed.

- Though there exist numerous approaches to produce nanostructures based on ZnO, their reliable and controlled generation is still not trivial. One of the most powerful techniques to create ZnO-based structures is ALD. In this thesis, a combination of NSL, ALD, electrodeposition, and e-beam evaporation was used to produce highly-ordered ZnO/Au urchin-like structures. The SERS capabilities of these substrates was investigated by grafting them with thiophenol. After testing three different Au layer thicknesses, it was found that the both 30 nm and 50 nm thicknesses presented the highest enhancements. The LOD of the optimized substrates was determined to be 10^{-8} M. Furthermore, the batch-to-batch repeatability was tested and a RSD of $<10\,\%$ was obtained. Adenine was detected with concentrations as low as 10^{-6} M, which demonstrates the capability of the substrates to biomolecules sensing. These results suggest that the urchin-like ZnO/Au structures can be successfully applied as SERS substrates.

- The SiNWs and urchin-like structures described above were used as a basis to prepare Pd/Au nanoparticles and ZnO/Au/ZIF-8 films, respectively. The formation of Pd nanoparticles was achieved by using ALD. After, Au was introduced to the SiNWs/Pd structures by the galvanic replacement reaction. EDX and XPS techniques were used to confirm the chemical composition of these sructures and it was found that Au had been replace successfully by looking at its oxidation state. The deposition of ZIF-8 on ZnO/Au urchin-like structures was performed by using a novel oxygen-assisted cathodic synthesis strategy. The morphology of these structures was studied with SEM, which showed an homogeneous film of ZIF-8 covering the 3D structures. Additionally, the composition of the films was studied with XRD, which confirmed the presence of ZIF-8 on the surface of the urchins.

A short outlook for the possible research directions of the projects introduced in this thesis is described as follows:

- The selection of an adequate functionalization method of the SiNWs/ZnO structures for the immobilization of bio-recognition elements should be studied. Furthermore, the selection of a relevant enzyme/substrate system for the biosensing proof-of-concept should be addressed. Also, the stability of the ZnO layer towards aqueous environments should be tested as many biosensing applications involve the introduction of the substrates into complex media (e.g., blood). Because POC applications demand the use of portable devices, the photoluminescence properties of the nanostructures should be tested with adequate compact UV lightsources.
- To have a deeper understanding of the exact Raman enhancement mechanism of the Au/ZnO urchin-like structures, finite-difference time-domain (FDTD) simulations could be performed. In addition, the influence of the size and geometry of the urchins on the localization of the LSPR could be investigated. Similarly, the influence on the optical properties and SERS enhancement of the substrates after annealing (transformation of the Au film into nanoparticles) could be studied. To validate the biosensing capability of the substrates, DNA detection could be envisioned by immobilizing a capture probe DNA on the surface of the Au/ZnO urchin-like structures, which could detect a target DNA carrying a reporter probe labeled with a dye, leading to a detectable SERS signal.
- The morphology of the SiNWs/Pd/Au could be investigated by TEM. Also, the influence on the Pd loading and the ratio of Au replacement could be performed, which could give a broader tunability of the composition and morphology of these bimetallic nanostructures. Moreover, these hybrid structures could be tested for SERS activity by choosing an adequate probe. Regarding the ZnO/Au/ZIF-8 urchin-like structures, TEM measurements could be performed to have a better idea of the morphology of the ZIF-8

film. The thickness of the ZIF-8 film could be changed in order to study the influence on the morphology and optical properties of the hybrid structures. Extinction and SERS measurements could be conducted with a suitable probe that cannot be adsorbed on a bare Au surface (e.g., benzene) to study the capability of the ZIF-8 film for trapping these type of molecules.

In the last decade, the vast amount of theoretical and experimental work on transducer elements for biosensing has expanded the collection of available materials and nanostructures. The influencing demand of fabricating reliable and robust biosensors has stimulated the development of novel approaches that can deliver reproducible nanostructured substrates with a tough control of their size, composition, and morphology. As one of the few established methods that allows depositing thin films with high conformality over complex 3D structures, ALD has revolutionized the semiconductors industry by becoming a key technology for microelectronic devices fabrication. Moreover, the ALD technology has had a direct impact in the development of novel types of biosensors platforms by being combined with other fabrication techniques such as NSL, electrodeposition, and electrospinning. However, a cost-effectiveness analysis should be performed before these approaches can be implemented into large scale production lines. For instance, ALD is a slower (up to two orders of magnitude) technique than CVD and usually requires vacuum conditions, thus making it hard and expensive to scale up. Additionally, when lithographic techniques based on nanospheres are used to produce wafer-scale nanostructures, the resulting substrate is usually accompanied by point defects that can have a negative effect on their overall performance. Thus, to overcome these limitations, novel approaches such as spatial ALD and nanoimprint lithography (NIL) have been developed and represent cost-effective tools that can be implemented to produce nanostructured transducer materials for biosensors.

Going forward, we believe that the SiNWs and urchin like structures presented in this work will serve as the basis for future transducer elements by targeting portable systems that are non-invasive and that can be used at home. Moreover, their tailorability and potential surface functionalization with bio-recognition elements derived from semi-synthetic ligands (e.g., aptamers, affibodies, peptide arrays, and molecularly imprinted polymers) will further expand their use as transducers for sensitive, selective, and stable biosensors. Finally, we envision that the nanostructures and techniques presented in this work will continue to expand their presence in real-world applications.

List of publications and conferences

Publications

- **O. Graniel** *et al.*, *Atomic layer deposition for biosensing applications.* Biosens. Bioelectron. 122 (2018) 147–159. doi:10.1016/j.bios.2018.09.038.
- **O. Graniel**, *et al.*, *Optical properties of ZnO deposited by atomic layer deposition (ALD) on Si nanowires.* Mater. Sci. Eng. B. 236–237 (2018) 139–146. doi:10.1016/j.mseb.2018.11.007.
- **O. Graniel** *et al.*, *Au-covered hollow urchin-like ZnO nanostructures for surface-enhanced Raman scattering (SERS) sensing.* Under revision in Journal of Materials Chemistry C.
- I. Iatsunskyi, **O. Graniel**, E. Coy, M. Weber, P. Miele, M. Bechelany, *Si/TiO_2/Pd nanowires prepared by ALD for photoelectrocatalysis.* Under revision in Chemical Engineering Journal.
- M. Baitimirova, J. Andzane, R. Viter, B. Fraisse, **O. Graniel**, M. Bechelany, D. Peckus, S. Tamulevicius, D. Erts, *Structure and Enhanced Photoluminescence of ZnO in Bi_2Se_3/ZnO Heterostructures.* Under revision in The Journal of Physical Chemistry C.
- M. Weber, **O. Graniel**, S. Balme, P. Miele, M. Bechelany. On the use of MOFs and ALD layers as nanomembranes for the enhancement of gas sensors selectivity. Accepted to Nanomaterials.

Conferences

- Poster presentation: *Atomic layer depositon for biosensing applications.* Réseau des Acteurs Français de l'ALD 2017. November 7-9, 2017, Montpellier, France.
- Oral presentation: *Atomic layer deposition for biosensing applications.* CanBioSe workshop. September 14-15, 2018, Rome, Italy.
- Oral presentation: *Atomic layer deposition for biosensing applications.* 4th International Conference on Bioinspired and Biobased Chemistry & Materials (N.I.C.E. 2018). October 14-17, 2018, Nice, France

- Oral presentation: *Atomic layer deposition for biosensing applications.* Réseau des Acteurs Français de l'ALD 2018, November 06-08, 2018, Lyon, France

- Oral presentation: *Au-covered ZnO urchin-like structures for surface-enhanced Raman scattering (SERS) sensing.* CanBioSe workshop. April 17-18, Vilnius, Lithuania.

- Oral presentation: *Atomic layer deposition for biosensing applications.* 6th International Conference on Bio-Sensing Technology. June 16-19, 2019. Kuala Lumpur, Malaysia.

- Oral presentation: *Au-covered ZnO urchin-like structures for surface-enhanced Raman scattering (SERS) sensing.* Nanomaterials for biosensors and biomedical applications. 2-4 July, 2019. Jūrmala, Latvia.

Appendices

Appendix A

Appendix for Chapter 4

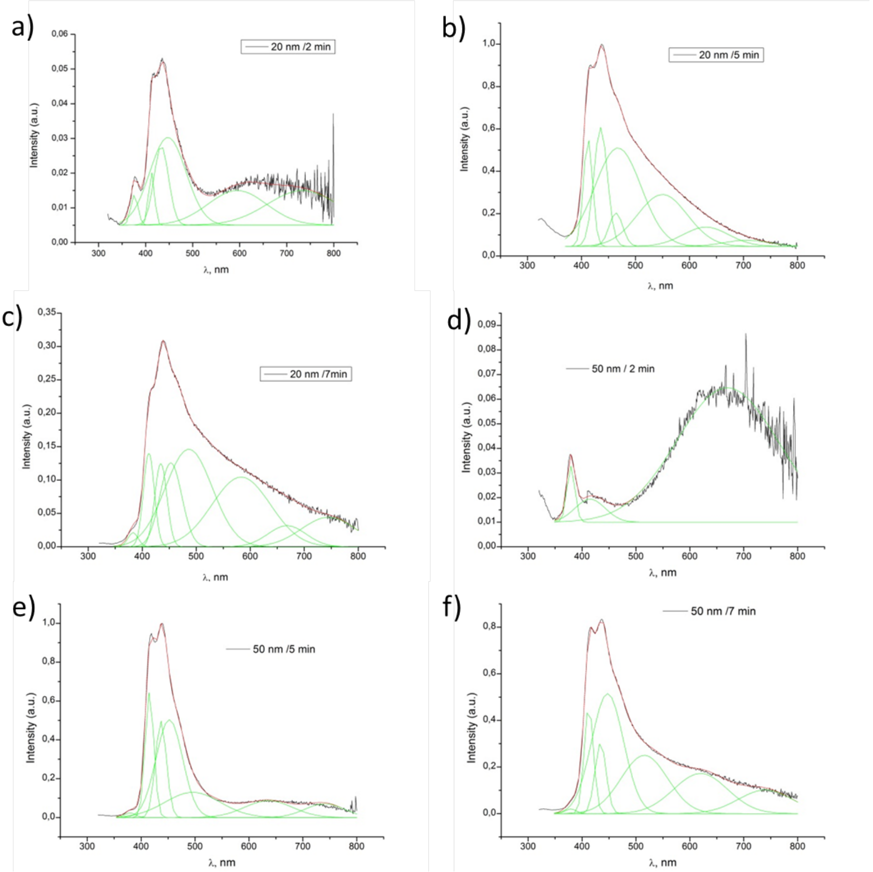

Figure A.1: Deconvolution of peaks for the PL spectra of SiNWs prepared at different etching times: 2, 5 and 7 minutes, and after ALD of 20 and 50 nm of ZnO.

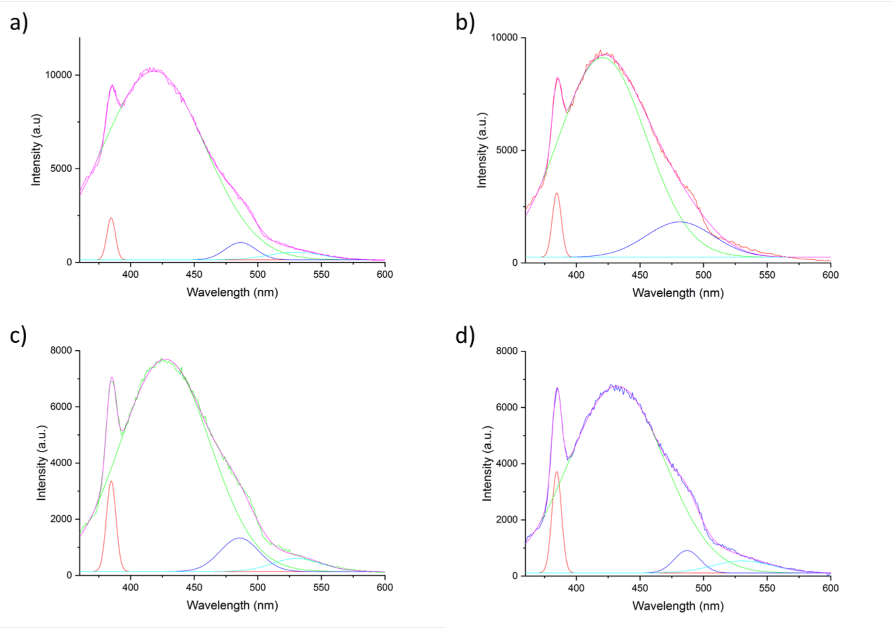

Figure A.2: Deconvolution of peaks for the PL spectra of SiNWs etched for 5 min and covered with a 50 nm ZnO film by ALD, and after being exposed to (b), (c), and (d), 10 mM, 20 mM, and 30 mM of H_2O_2.

Appendix B

Appendix for Chapter 5

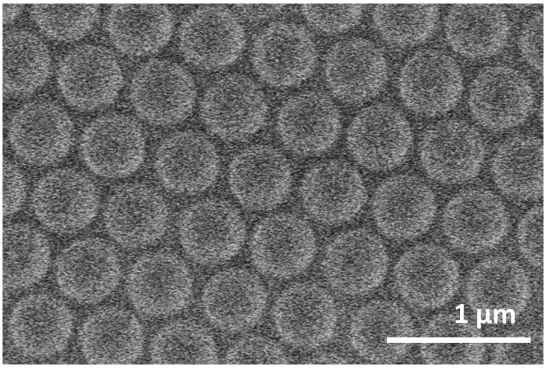

Figure B.1: SEM micrograph of PS spheres exposed to an O_2 plasma for 5 min.

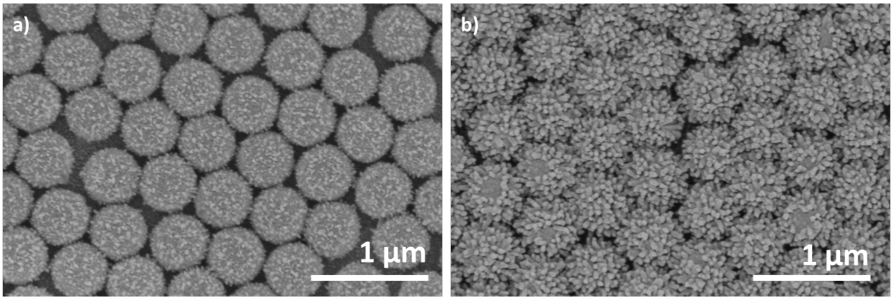

Figure B.2: SEM micrographs of urchin-like ZnO structures covered by a a) 10 nm and a b) 50 nm Au layer deposited by e-gun evaporation (scale bar: 1 µm).

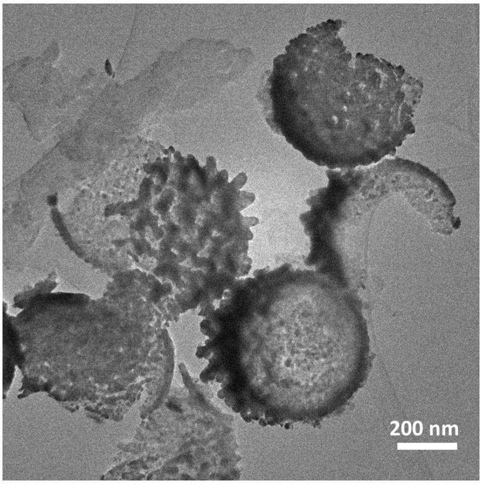

Figure B.3: TEM image of a Au-covered ZnO urchin-like structures. The cavity has a reduced contrast and a shell with a uniform dark gray color.

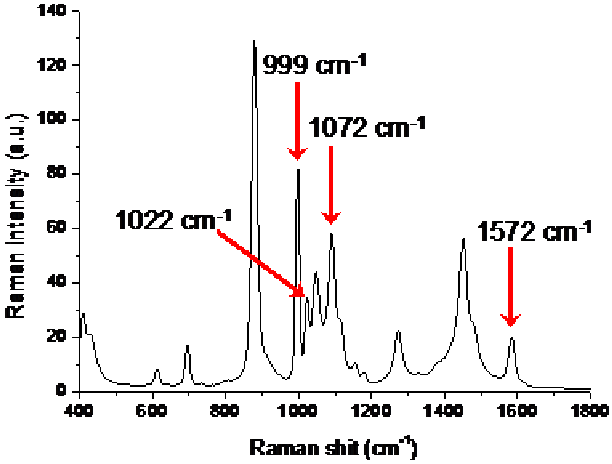

Figure B.4: Raman spectrum of thiophenol in ethanol recorded at the excitation wavelength of 785 nm where the four Raman peaks studied here are displayed. The rest of the peaks correspond either to thiophenol or ethanol. Reprinted with permission from [1]. Copyright 2017 Elsevier.

[1] Bryche, J. F. et al. “Low-cost SERS substrates composed of hybrid nanoskittles for a highly sensitive sensing of chemical molecules.” *Sensors and Actuators B: Chemical* vol. 239 (2017), pp. 795–799.